

The Pennsylvania State University
The Graduate School
College of Engineering

TITLE OF YOUR THESIS

A Dissertation
in Civil Engineering
by
Charilaos Lyritsakis

© Charilaos Lyritsakis 2022

Submitted in Partial Fulfillment
of the Requirements
for the Degree of

Doctor of Philosophy

December 2022

The dissertation of Charilaos Lyritsakis was reviewed and approved* by the following:

Kostas Papakonstantinou
Associate Professor of Civil & Environmental Engineering
Dissertation Advisor
Chair of Committee

Gordon Warn
Associate Professor of Civil & Environmental Engineering

Pinlei Chen
Assistant Professor of Civil & Environmental Engineering

Tong Qiu
Professor of Civil & Environmental Engineering

Reuben Kraft
Associate Professor of Mechanical Engineering

Patrick Fox
Professor of Civil & Environmental Engineering
Head of Department of Civil & Environmental Engineering

* Signatures are on file in the Graduate School.

Abstract

Lorem ipsum dolor sit amet, consectetur adipiscing elit, sed do eiusmod tempor incididunt ut labore et dolore magna aliqua. Ut enim ad minim veniam, quis nostrud exercitation ullamco laboris nisi ut aliquip ex ea commodo consequat. Duis aute irure dolor in reprehenderit in voluptate velit esse cillum dolore eu fugiat nulla pariatur. Excepteur sint occaecat cupidatat non proident, sunt in culpa qui officia deserunt mollit anim id est laborum.

To my parents

Table of Contents

List of Figures	ix
List of Tables	xi
Nomenclature	xii
Acronyms	xvi
Acknowledgements	xvii
Chapter 1: Introduction and Background	1
1.0.1 Notation	1
Chapter 2: Hybrid Beam Element Formulation	2
2.1 Introduction	2
2.2 Geometrically-Exact Model	3
2.2.1 Beam Kinematics	3
2.2.2 Strain Measures, Strain-Displacement Relations	5
2.3 Nonlinear Programming Formulation	7
2.3.1 NLP framework	7
2.3.2 Total potential energy	8

2.3.3	Strain-Displacement Constraints	9
2.3.4	Lagrangian function	11
2.4	Implementation	12
2.4.1	Equilibrium	14
2.4.2	Hessian matrix	15
2.4.3	Solution scheme	15
2.4.4	Cross-section state determination	20
2.5	Numerical Examples	24
2.5.1	Cantilever with tip load	25
2.5.2	Lee's frame	29
2.5.3	Two-Storey frame	33
Chapter 3: Material Constitutive Model	37
3.1	Introduction	37
3.2	Three-dimensional Constitutive Model	38
3.3	The J_2 formulation for fiber stress state	40
3.3.1	Mapping on the constrained stress space	40
3.3.2	Continuous tangent modulus	43
3.4	Implicit integration of rate equations	44
3.4.1	Elastic predictor - Plastic Corrector algorithm	45
3.4.2	Consistent Tangent Modulus	46
3.4.3	Consistent Section Stiffness	47
3.5	Numerical Examples	49

3.5.1	Accuracy of the proposed algorithm	49
3.5.2	Performance against non-monotonic strain histories	51
3.5.3	Plastic collapse of a doubly clamped beam	52
3.5.4	Cyclic loading of shear link	57
3.5.5	Elastoplastic post-buckling behavior of two-beam structure	58
3.5.6	Three story frame with shear links	61
Chapter 4: Naturally Parameterized NLP framework	65
4.1	Introduction	65
4.2	Homotopy Continuation	67
4.2.1	Main idea	67
4.2.2	Regularity and existence of homotopy paths	70
4.2.3	Parametric nonlinear programming	72
4.2.4	Global optimization	76
Chapter 5: Conclusion	79
Appendix A:	81
A.0.1	Gradient of strain energy	81
A.0.2	Gradient of constraints	82
A.0.3	Gradient of the potential energy	85
A.0.4	Gradient of the Lagrangian	85
Appendix B:	87

Appendix C:	90
Appendix D:	92
References	93

List of Figures

2.1	Undeformed and deformed configurations of the beam.	4
2.2	Integration of curvature shape functions.	11
2.3	Typical element representing one member.	13
2.4	Solution process stages. Quantities \mathbf{K}^e and $\vec{\mathbf{F}}_{int}$ stand for stiffness matrix and internal nodal force vector for element e respectively.	23
2.5	Geometrically nonlinear analyses of cantilever.	27
2.6	Moment and curvature distributions for the nonlinear analyses of the cantilever - one element with $n = 6$ quadrature points.	27
2.7	Influence of L/h on the tip deflection and comparison with analytical solution. .	28
2.8	Geometrically nonlinear analyses of Lee's frame with pinned supports.	30
2.9	Deformation profiles for Lee's frame with pinned supports.	30
2.10	Effect of shear flexibility on Lee's frame response.	31
2.11	Deformation profiles for Lee's frame with fixed supports.	32
2.12	Geometrically nonlinear analyses of Lee's frame with fixed supports.	33
2.13	Two-storey portal frame discretization.	34
2.14	Geometrically nonlinear analyses of the two-storey frame.	34
2.15	Deformation profiles for two-storey frame.	35
3.1	Feasible space and yield locus for the J_2 model. At the boundary of the ellipse, $\sqrt{3J_2} = q$	41

3.2	Points of interest on yield surface and direction of load increments.	50
3.3	Iso-error maps for a perfectly plastic material.	50
3.4	Iso-error maps for combined linear isotropic and kinematic hardening.	51
3.5	The four different strain histories imposed, with the unstresses configuration as initial point.	52
3.6	Geometry, initial and final configuration of clamped beam, along with cross-section dimensions.	55
3.7	Load-deflection plots for different slenderness ratios. Influence of quadrature type and number of points.	56
3.8	Case $L/h = 4$. Spread of Plastic Zone (P.Z.) and stress distribution for von Mises, axial and shear stress at three different load levels.	56
3.9	Geometry of the specimen and displacement-controlled loading history.	58
3.10	Experimental and numerical results for the specimen.	59
3.11	Geometry and loading of two-beam structure. Comparison of load vs deflection curves for different cases.	60
3.12	Influence of slenderness and constitutive model on the response for elastic and elastoplastic behavior.	60
3.13	Geometry of the steel frame and 3.13b response curves for three different models.	62
4.1	A homotopy path connecting the trivial solution of $G = 0$ to a root of $F = 0$ for a single scalar equation dependent on x	68
4.2	Homotopy paths for (a) $f(x) = x^3 - 6x^2 + 21x - 26 = 0$, with starting point $x_0 = 0$ and convergence at root $x_1 = 2$ when $t = 1$ and (b) truss, with initial state the undeformed configuration($x_0 = 0$) and target load level $P = 0.03$	69
4.3	Components of $H^{-1}(0)$ in \mathbb{R}^{n+1}	71
4.4	Piecewise continuously differentiable paths and loops of $\mathbf{H}_{KKT}^{-1}(\mathbf{0})$ in $\mathbb{R}^{n+l+p+1}$	77

List of Tables

2.1	Comparison of tip normalized displacements for different load levels for elastic response.	26
3.1	Results for Scenario 1, perfect plasticity.	53
3.2	Results for Scenario 2, perfect plasticity.	53
3.3	Results for Scenario 3, perfect plasticity.	53
3.4	Results for Scenario 4, five cycles, perfect plasticity. One cycle: A-B-C-A.	53
3.5	Collapse moments and loads for clamped beam.	55
3.6	Material properties for Example 3.5.4.	57
3.7	Member geometric and material data.	59
3.8	Convergence in residual norm during steps 5, 15, 25 35. $\epsilon_{tol} = 10^{-10}$	61
3.9	Convergence in energy norm during steps 5, 15, 25, 35. $\epsilon_{tol} = 10^{-10}$	61
3.10	Vertical gravity loads at nodes.	62

Nomenclature

\vec{E}_i	Spatial basis unit vectors, $i = 1, 2, 3$
\vec{e}_i	Material basis unit vectors, $i = 1, 2, 3$
X_i	Initial configuration coordinates, $i = 1, 2, 3$
\vec{X}	Position vector of a material point in the initial configuration
x_i	Current configuration coordinates, $i = 1, 2, 3$
\vec{x}	Position vector of a material point in the current configuration
\vec{r}_o	Position vector of a material point on the centerline in the initial configuration
\vec{r}	Position vector of a material point on the centerline in the current configuration
\vec{u}	Displacement vector of points on the centerline with respect to the initial configuration.
\vec{t}	Position vector of a material point on the local system of a cross-section.
ϕ	Angle between \vec{E}_i and \vec{e}_i
$\mathbf{R}(\phi)$	Rotation matrix
κ	Curvature of the beam centerline.
ϵ	Axial strain of the beam centerline
γ	Shear strain of the beam centerline
\vec{s}	Vector containing ϵ and γ but not κ
u	Displacement component along X_1
v	Displacement component along X_2
\vec{d}	Displacement vector containing u, v and ϕ
\vec{q}	Strain vector containing ϵ, γ and κ
f	Generic objective function

\vec{h}	Vector of discretized constraints
\mathcal{S}	Constrained space for \vec{x}
\mathcal{L}	Lagrangian function associated with the NLP
$\vec{\lambda}$	Vector of Lagrange multipliers associated with equality constraints
Π	Total potential energy function
U	Strain energy function
W	Potential energy of external loads
\mathcal{W}_s	Cross-section strain energy density
\vec{P}	Vector of external loads
\vec{F}_{sec}	Cross-section stress resultants
N	Section axial force
V	Section shear force
M	Section internal moment
E	Young's modulus
G	Shear modulus
I	Cross-section moment of inertia
A	Cross-section area
A_s	Effective area of the cross-section
ℓ	Element length
n_{nod}	Number of non-restrained nodes
n	Number of quadrature points in the element
w_i	Quadrature weight for the i -th quadrature point
ξ	Normalized coordinate associated with X_1
L_i	Lagrange cardinal function
\mathbf{T}	Curvature mapping matrix
Θ	Vandermonde matrix
\vec{y}	Internal field variable vector, associated with unknowns at quadrature points

Λ	Element orientation matrix
θ	Angle of element centerline in the initial configuration with \vec{E}_1
\mathcal{E}^e	Energy contribution of element e in the Lagrangian function
H	Hessian matrix
\vec{z}	Vector of all unknown state variables of the system
\mathbf{k}_s	Section stiffness matrix
K	Stiffness matrix
\vec{F}_{int}	Internal nodal force vector
ΔS	Incremental arc-length parameter
$\vec{\sigma}_f$	Vector of active stress components on a fiber
$\vec{\epsilon}_f$	Strain components corresponding to $\vec{\sigma}_f$
N_s	Cross-section shape function matrix
φ	Shear strain distribution function along the cross-section height
C	Material tangent modulus
$\vec{d}_{l,r}$	Element nodal displacement vector for left (l) or right (r) elememtn edge
$\vec{P}_{l,r}$	Element externally applied nodal force vector for left (l) or right (r) elememtn edge
σ	Cauchy stress tensor
ϵ	Strain tensor
a	Back stress tensor
q	Current uniaxial yield stress
e^{pl}	Equivalent plastic strain
λ	Plastic parameter
Φ	Yield function
σ_{eq}	Equivalent stress associated with the appropriate yield criterion
H_{kin}	Kinematic hardening modulus
H_{iso}	Isotropic hardening modulus
C, C	Fourth order constitutive tensor and its matrix representation

J_2	Second invariant of the deviatoric stress tensor
σ_y	Yield stress of the virgin material
ζ	Effective stress tensor
\mathbf{w}^d	Deviatoric part of a tensor \mathbf{w}
\mathbf{C}_c^{pl}	Consistent elastoplastic tangent modulus
$\vec{\mathbf{H}}$	Homotopy (vector) function
t	Pseudo-time or homotopy parameter
C^k	Space of functions with their first k derivatives continuous
Γ	A (connected) component, path or loop, in $\vec{\mathbf{H}}^{-1}(\vec{0})$
Ω	Feasible space for an NLP or PNLP program
I_h	Index set of equality constraints
I_g	Index set of inequality constraints
$\vec{\boldsymbol{\mu}}$	Vector of Lagrange multipliers associated with inequality constraints
\bar{I}_g	Index set of active inequality constraints
\mathcal{D}	Subdivision of an interval
$\tau(\bar{I}_g)$	Cell associated with subdivision of Ω
W^q	Subinterval associated with subdivision \mathcal{D}

Acronyms

DOF Degree of Freedom.

FEM Finite Element Method.

KKT Karush-Kuhn-Tucker.

LICQ Linear Independence Constraint Qualification.

NLP Non-Linear Programming.

NPNLP Naturally Parameterized Non-Linear Programming.

PNLP Parametric Non-Linear Programming.

SCC Strict Complementarity Condition.

TPE Total Potential Energy.

Acknowledgements

Consectetur adipiscing elit

Ut enim ad minim veniam, quis nostrud exercitation ullamco laboris nisi ut aliquip ex ea commodo consequat.

Duis aute irure dolor in reprehenderit in voluptate velit esse cillum dolore eu fugiat nulla pariatur.

Excepteur sint occaecat cupidatat non proident, sunt in culpa qui officia deserunt mollit anim id est laborum.

CHAPTER 1

INTRODUCTION AND BACKGROUND

1.0.1 Notation

Unless state otherwise, boldface lowercase letters indicate second order tensor. Wherever the same letters appear with an overhead arrow, this indicates the vector notation for the tensor represented with that letter. The convention adopted herein for storing second order tensors in a vector object is the following:

$$\boldsymbol{\sigma} = \begin{bmatrix} \sigma_{11} & \sigma_{12} & \sigma_{13} \\ \sigma_{12} & \sigma_{22} & \sigma_{23} \\ \sigma_{13} & \sigma_{23} & \sigma_{33} \end{bmatrix} \rightarrow \vec{\boldsymbol{\sigma}} = \begin{bmatrix} \sigma_{11} & \sigma_{22} & \sigma_{33} & \sigma_{12} & \sigma_{23} & \sigma_{13} \end{bmatrix}^T$$

For strain tensors, components for which $i \neq j$ are multiplied by 2.

In addition, any boldface letter, lowercase or uppercase, with an overhead arrow indicates a vector object. In contrast, matrices are represented exclusively by uppercase, non-italic, boldface letters. Finally, normal font letters indicate scalar quantities.

CHAPTER 2

HYBRID BEAM ELEMENT FORMULATION

2.1 Introduction

In this chapter we present the formulation of a novel hybrid beam element which is based on NLP principles. The kinematic assumptions adopted fall under the category of geometrically exact or Simo-Reissner beam theory[1, 2, 3, 4], whereby no simplifying approximation is made with respect to the strain-displacement equations. This allows for capturing arbitrarily large displacements and rotations, as well as accounting for the effect of shear deformation at the section level.

As opposed to deriving the system equations from the Galerkin form,, we recast the problem in an NLP framework by utilizing the underlying variational structure. The total potential energy (TPE) functional is augmented with all relevant conditions that enforce the exact kinematics, by introducing a set of Lagrange multipliers that act as conjugate force quantities. The resulting modified functional is then approximated by employing a Gauss-Legendre quadrature rule, which yields the objective function to be minimized. With this particular approach, the primary variables in the element interior contributing to the elastic strain energy are the generalized strain measures of the centroid, which are the unknown quantities at the quadrature points. Displacement measures at the edge nodes of the element, namely, the translations along coordinate axes and the rotation of cross sections, are only associated with the external work. Kinematic consistency between the rotational measures of displacement and strains is enforced by using a Lagrange interpolation scheme for the curvature field, similar to the one used by Neuenhofer and Filippou [5] and Schulz & Filippou [6] for force-based elements. In this work, the points used for the interpolation coincide with the integration points of the quadrature rule used for approximating the energy functional. To avoid ill-conditioning issues of the linearized operator,

we also outline a block-elimination procedure for the linear system involving the Hessian matrix so that the reduced system includes only displacement components. The corresponding stiffness operator is well-conditioned, sparse, banded and symmetric. This renders standard FEM routines from existing codes reusable and, in conjunction with the capability for accuracy even with crude discretization, provides an attractive formulation for fast and accurate computation. Additionally, accuracy and locking free performance are guaranteed with just one element per structural member, even in the presence of arbitrarily large displacements and rotations. Accordingly, the element can also capture high curvature gradients due to plastic hinge formation, in the case of inelastic analysis.

This chapter starts with a brief outline of the beam geometric description while adhering to the derivations by Cardona & Geradin[7], followed by the hybrid NLP formulation for the element. The third section is devoted to implementation details, where special attention is given to the block elimination technique used for the reduction of the linear system involving the Hessian matrix. Finally, the chapter concludes with a set of numerical examples where the focus is the Hybrid NLP element performance with respect to coarse mesh discretizations in nonlinear analysis.

2.2 Geometrically-Exact Model

2.2.1 Beam Kinematics

Let $\{\mathbf{E}\}$ be a fixed orthonormal coordinate frame with unit vectors $\{\vec{\mathbf{E}}_1, \vec{\mathbf{E}}_2, \vec{\mathbf{E}}_3\}$ along the axes X_1, X_2, X_3 . For an initially straight beam of length ℓ with its centerline coinciding with X_1 , the undeformed configuration is completely described by:

$$\vec{\mathbf{X}}(X_1, X_2) = X_1 \vec{\mathbf{E}}_1 + X_2 \vec{\mathbf{E}}_2 = \vec{\mathbf{r}}_o(X_1) + \vec{\mathbf{t}}(X_2) \quad (2.1)$$

where $\vec{\mathbf{r}}_o$ traces the centerline in the reference configuration and $\vec{\mathbf{t}}$ locates a material point on the cross section. Assuming a rectangular cross-section of height h , without loss of generality,

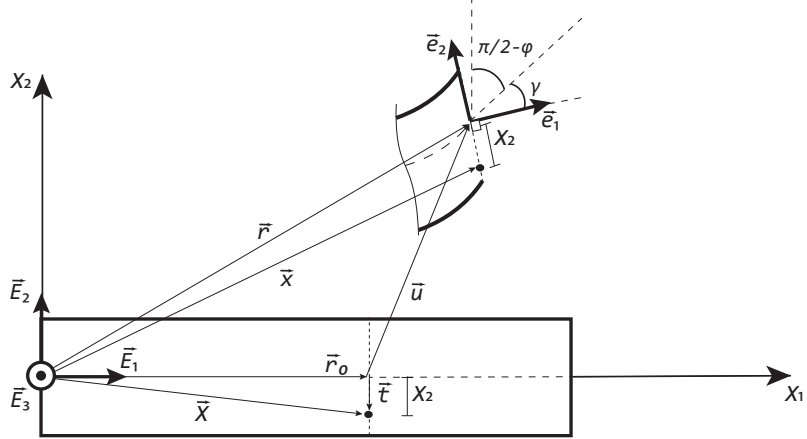


Fig. 2.1. Undeformed and deformed configurations of the beam.

we have that $X_1 \in [0, \ell]$ and $X_2 \in [-\frac{h}{2}, \frac{h}{2}]$. We should note here that X_3 is omitted as it does not explicitly come into the expressions. We nevertheless hold on to the \mathbb{R}^3 vector formalism to maintain consistency with the representation of rotation as a linear operator. After the application of a displacement field $\vec{u}(X_1)$, the deformed configuration is given by vector \vec{x} such that:

$$\vec{r} = \vec{r}_o + \vec{u} \quad (2.2)$$

$$\vec{x} = \vec{r} + X_2 \vec{e}_2 \quad (2.3)$$

where $\{\mathbf{e}\}$ is a local coordinate system attached at cross-sections that completely describes their orientation. For the unit vectors of the local base \vec{e}_1 , \vec{e}_2 , \vec{e}_3 , we let \vec{e}_1 be normal to the cross-section, but not necessarily tangent to the deformed centerline, and \vec{e}_2 (and \vec{e}_3) coincide with the cross-section principal axes of inertia, as shown in Fig. (2.1).

If \mathbf{R} is the rotation operator that rotates $\{\mathbf{E}\}$ to $\{\mathbf{e}\}$, then:

$$\vec{e}_i = \mathbf{R} \vec{E}_i, \quad i = 1, 2, 3 \quad (2.4)$$

For the plane case, the component form of \mathbf{R} reduces to:

$$\mathbf{R} = \begin{bmatrix} \cos \phi & -\sin \phi & 0 \\ \sin \phi & \cos \phi & 0 \\ 0 & 0 & 1 \end{bmatrix} \quad (2.5)$$

Then, using Eq. (2.4), Eq. (2.3) becomes:

$$\vec{x} = \vec{r} + \mathbf{R}\vec{t} \quad (2.6)$$

For Eqs. (2.3),(2.6) to hold in this manner, we tacitly assume that cross-sections remain rigid during deformation, that is, the position of a material point on a cross-section with respect to the centroid does not change.

2.2.2 Strain Measures, Strain-Displacement Relations

Within the context of geometrically-exact formulations, it is common to adopt as a strain measure \vec{s} the difference of the position vector gradients, \vec{r} and \vec{r}_o , with respect to the local frame (e.g. see [2, 7, 8]). Denoting derivatives with respect to X_1 by $(\cdot)'$, we get:

$$\vec{s} = \mathbf{R}^T \vec{r}' - \vec{r}'_o \quad (2.7)$$

whereas the cross-section curvature is given as:

$$\kappa = \phi' \quad (2.8)$$

The axial and shear strain of the centroid, ϵ and γ respectively, can then be retained as follows:

$$\epsilon = \vec{e}_1^T \vec{s} \quad (2.9)$$

$$\gamma = \vec{e}_2^T \vec{s} \quad (2.10)$$

where $\vec{s} = \begin{bmatrix} \epsilon & \gamma & 0 \end{bmatrix}^T$, with the third component, representing the shear strain along the out-of-plane axis, being by assumption zero.

Using Eq. (2.2) and performing the differentiations in Eq. (2.7) with respect to X_1 , we get:

$$\vec{s} = \mathbf{R}^T [\vec{u}' + \vec{E}_1] - \vec{E}_1 \quad (2.11)$$

Deriving the exact differential strain-displacement relations as presented in Reissner¹ is straightforward if we solve Eq. (2.11) for \vec{u}' :

$$\vec{u}' = \mathbf{R}\vec{s} + \vec{e}_1 - \vec{E}_1 \quad (2.12)$$

If we write $\vec{u} = \begin{bmatrix} u & v & 0 \end{bmatrix}^T$, then the explicit expressions for u', v' along with Eq. (2.8) are:

$$u' = \vec{E}_1^T \vec{u}' = (1 + \epsilon) \cos \phi - \gamma \sin \phi - 1 \quad (2.13a)$$

$$v' = \vec{E}_2^T \vec{u}' = (1 + \epsilon) \sin \phi + \gamma \cos \phi \quad (2.13b)$$

$$\phi' = \kappa \quad (2.13c)$$

By introducing vectors \vec{d} and \vec{q} , such that $\vec{d} = \begin{bmatrix} u & v & \phi \end{bmatrix}^T$ and $\vec{q} = \begin{bmatrix} \epsilon & \gamma & \kappa \end{bmatrix}^T$, we can maintain the structure of Eq. (2.12) and express all fields involved in matrix notation, as follows:

$$\vec{d}' = \mathbf{R}\vec{q} + \vec{e}_1 - \vec{E}_1 \quad (2.14)$$

Strain-displacement equations as represented in Eq. (2.14) will be subsequently utilized in the formulation of the beam model.

¹See equations (15) in [1]

2.3 Nonlinear Programming Formulation

The hybrid beam element discretization is presented by utilizing the underlying variational structure of the static problem. The minimizing principle for the TPE is recast here in an NLP formulation and the strain-displacement equations in (2.14) are incorporated, representing the equality constraints of the problem.

2.3.1 NLP framework

The NLP problem adopted herein is of the following form:

$$\begin{aligned} & \text{minimize} && f(\vec{x}) \\ & \text{subject to} && \vec{h}(\vec{x}) = \vec{0} \\ & && \vec{x} \in \mathcal{S} \end{aligned} \tag{2.15}$$

The objective function $f(\vec{x})$ represents the total potential energy of the structure, whereas vector $\vec{h}(\vec{x})$ includes the active constraints of the program. The corresponding Lagrangian is:

$$\mathcal{L}(\vec{x}, \vec{\lambda}) = f(\vec{x}) + \vec{\lambda}^T \vec{h}(\vec{x}) \tag{2.16}$$

where $\vec{\lambda}$ are the Lagrange multipliers. The first-order optimality conditions are given from the following expression:

$$\nabla \mathcal{L} = \vec{0} \tag{2.17}$$

This is the standard form of a nonlinear constrained minimization program with equality constraints, as encountered in the literature (e.g. [9]).

2.3.2 Total potential energy

We consider the following decomposition of the total potential energy of a beam:

$$\Pi = U - W \quad (2.18)$$

where U and W are the stored strain energy and potential energy associated with external loading respectively. For the case of concentrated external loads, Eq. (2.18) can be expressed as:

$$\Pi = \int_0^\ell \mathcal{W}_S(X_1, \vec{q}) dX_1 - \sum_{i=1}^2 \vec{P}_i^T \vec{u}_i \quad (2.19)$$

where \mathcal{W}_S is the strain energy density of a cross section at X_1 and \vec{q} denotes the neutral axis strain vector, \vec{P}_i, \vec{u}_i the element nodal force and displacement vectors, respectively. It can be proven[10] that for strain hardening materials within the premises of small strain elastoplasticity, the exact solution to the problem renders Π an absolute minimum. Equivalently, the exact solution solves the program in Eq. (2.15) for $f = \Pi$ with \vec{h} acting as constraints. Assuming a stable work-hardening material, the corresponding Euler-Lagrange equations yield the constitutive equations of elastoplasticity (e.g. see discussion in Simo and Hughes [11]). As it will be shown in subsequent sections, since the constitutive update is carried out locally at the section fiber level.

Section stress resultants are then given by the gradient of \mathcal{W}_S :

$$\vec{F}_{sec} = \nabla_{\mathbf{q}} \mathcal{W}_S \quad (2.20)$$

with $\vec{F}_{sec} = \begin{bmatrix} N & V & M \end{bmatrix}^T$. In the case of linear elasticity, the energy density is given by

$\mathcal{W}_S = \frac{1}{2}[EA\epsilon^2 + GA_s\gamma^2 + EI\kappa^2]$ and the section resultants are:

$$\vec{\mathbf{F}}_{sec} = \begin{bmatrix} EA\epsilon \\ GA_s\gamma \\ EI\kappa \end{bmatrix}$$

where A_s is the effective shear area of the cross-section. Numerical approximation of Eq. (2.19) by an appropriate quadrature yields:

$$f(\vec{\mathbf{q}}_1, \dots, \vec{\mathbf{q}}_n, \vec{\mathbf{u}}_1, \dots, \vec{\mathbf{u}}_N) = \sum_{i=1}^n w_i \mathcal{W}_{S,i} - \sum_{i=1}^2 \vec{\mathbf{P}}_i^T \vec{\mathbf{u}}_i \quad (2.21)$$

with w_i and n being the weights and the number of integration points respectively, and $\mathcal{W}_{S,i} = \mathcal{W}_S(\vec{\mathbf{q}}_i)$. Eq. (2.21) serves as the objective function of the NLP of Eq. (2.15).

2.3.3 Strain-Displacement Constraints

The constrained conditions are derived by applying the same quadrature rule on the integral form of the strain-displacement equations (2.14):

$$\vec{\mathbf{d}}(\ell) - \vec{\mathbf{d}}(0) = \int_0^\ell \vec{\mathbf{d}}' dX_1 = \int_0^\ell \mathbf{R} \vec{\mathbf{q}} + \vec{\mathbf{e}}_1 - \vec{\mathbf{E}}_1 dX_1 \quad (2.22)$$

Using Eq. (2.4), numerical approximation of the right-hand side integral leads to the element specific constraints:

$$\vec{\mathbf{h}}^A = \vec{\mathbf{d}}(\ell) - \vec{\mathbf{d}}(0) - \sum_{i=1}^n w_i \mathbf{R}_i (\vec{\mathbf{q}}_i + \vec{\mathbf{E}}_1) + \ell \vec{\mathbf{E}}_1 = \vec{\mathbf{0}} \quad (2.23)$$

The component form of Eq. (2.23) can be given as:

$$\vec{h}^A = \begin{bmatrix} u(\ell) - u(0) - \sum_{i=1}^n w_i \left[(\epsilon_i + 1) \cos \phi_i - \gamma_i \sin \phi_i \right] + \ell \\ v(\ell) - v(0) - \sum_{i=1}^n w_i \left[(\epsilon_i + 1) \sin \phi_i + \gamma_i \cos \phi_i \right] \\ \phi(\ell) - \phi(0) - \sum_{i=1}^n w_i \kappa_i \end{bmatrix} \quad (2.24)$$

Although the strain fields appear explicitly only in the weighted evaluation points of the quadrature, the rotational field ϕ is involved in both the integration points and the element edge nodes. As such, we introduce a Lagrange interpolation scheme for the curvature field in the same fashion as in [12]:

$$\kappa(\xi) = \sum_{i=1}^n L_i(\xi) \kappa_i \quad (2.25)$$

where L_i are the Lagrange cardinal functions:

$$L_i(\xi) = \frac{\prod_{j=1, j \neq i}^n (\xi - \xi_j)}{\prod_{j=1, j \neq i}^n (\xi_i - \xi_j)}, \quad \xi = \frac{X_1}{\ell}$$

Substitution of Eq. (2.25) to Eq. (2.13c) yields the expression for rotations ϕ_i :

$$\phi_i - \phi(0) = \sum_{j=1}^n \left(\int_0^{\xi_i} L_j(x) dx \right) \kappa_j = \sum_{i=1}^n T_{ij} \kappa_j \quad (2.26)$$

with derivation of T_{ij} illustrated in Fig. (2.2). In matrix form, the above equation can be directly restated as a linear equality constraint set as:

$$\vec{h}^B = \vec{\phi} - \phi(0) \vec{1} - \mathbf{T} \vec{\kappa} = \vec{0} \quad (2.27)$$

where

$$\vec{\phi} = \begin{bmatrix} \phi_1 & \phi_2 & \cdots & \phi_n \end{bmatrix}^T, \vec{1} = \begin{bmatrix} 1 & 1 & \cdots & 1 \end{bmatrix}^T \in \mathbb{R}^n$$

$$\mathbf{T} = L \begin{bmatrix} \xi_1 & \frac{\xi_1^2}{2} & \cdots & \frac{\xi_1^n}{n} \\ \vdots & \vdots & \ddots & \vdots \\ \xi_n & \frac{\xi_n^2}{2} & \cdots & \frac{\xi_n^n}{n} \end{bmatrix} \Theta^{-1}, \Theta = \begin{bmatrix} 1 & \xi_1 & \xi_1^2 & \cdots & \xi_1^{n-1} \\ \vdots & \vdots & \vdots & \ddots & \vdots \\ 1 & \xi_n & \xi_n^2 & \cdots & \xi_n^{n-1} \end{bmatrix}$$

We can then collect all active constraints, Eqs. (2.23),(2.27), in one vector \vec{h} :

$$\vec{h} = \begin{bmatrix} \vec{h}^A \\ \vec{h}^B \end{bmatrix} = \begin{bmatrix} \vec{0} \\ \vec{0} \end{bmatrix} \quad (2.28)$$

containing all constraints pertaining to one element. While vector \vec{h}^A of strain-displacement constraints will always contain three components for each element, the number of components in vector \vec{h}^B will depend on the chosen quadrature rule.

2.3.4 Lagrangian function

In order to derive the Lagrangian function in the form of Eq. (2.16), we introduce a vector $\vec{\lambda}$ of additional Lagrange multiplier variables and augment Eq. (2.21) with Eq. (2.28):

$$\mathcal{L} = f + \vec{\lambda}^T \vec{h} \quad (2.29)$$

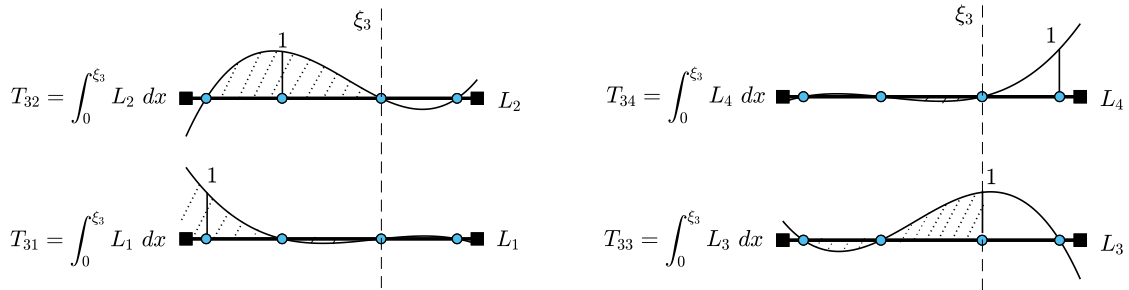


Fig. 2.2. Integration of curvature shape functions.

A more convenient form for the Lagrangian function can also be achieved by expanding f into its constituents, namely, the element stored energy and the potential energy:

$$\mathcal{L} = \sum_{e=1}^{n_{el}} U^e - W + \vec{\lambda}^T \vec{h} \quad (2.30)$$

where:

$$U^e = \sum_{i=1}^n w_i \mathcal{W}_{S,i}^e \quad , \quad W = \sum_{i=1}^N \vec{P}_i^T \vec{u}_i$$

Thereby, additional elements can be simply incorporated by adding their stored energy in the corresponding sum, and considering element constraints by augmenting vectors $\vec{\lambda}$, \vec{h} , after transforming them to the global system. Potential function W is “global” in the sense that external loads and the corresponding work-conjugate displacement degrees of freedom are directly added to the expression and are not influenced by adding nodal contributions from adjacent elements. As a result, no additional connectivity constraints at the element interfaces are needed, and Eq. (2.30) is thus a global function for the whole structure.

2.4 Implementation

The set of vectors associated with internal field variables, $\{\vec{y}_i\}_{i=1}^n$, is defined as $\vec{y}_i = \begin{bmatrix} \vec{q}_i & \phi_i \end{bmatrix}^T = \begin{bmatrix} \epsilon_i & \gamma_i & \kappa_i & \phi_i \end{bmatrix}^T$. Moreover, and according to Fig. (2.3), we designate the local element edge degrees of freedom in vector form as $\hat{\vec{d}}_l = \vec{d}(0)$ and $\hat{\vec{d}}_r = \vec{d}(\ell)$. The element displacement vector is thus $\hat{\vec{d}} = \begin{bmatrix} \hat{\vec{d}}_l^T & \hat{\vec{d}}_r^T \end{bmatrix}^T$. The corresponding global displacement vector \vec{d}_g is related to the local vector $\hat{\vec{d}}$ via the typical linear transformation Λ :

$$\hat{\vec{d}} = \begin{bmatrix} \Lambda & \mathbf{0} \\ \mathbf{0} & \Lambda \end{bmatrix} \vec{d}_g \quad , \quad \Lambda = \begin{bmatrix} \cos \theta & \sin \theta & 0 \\ -\sin \theta & \cos \theta & 0 \\ 0 & 0 & 1 \end{bmatrix} \quad (2.31)$$

The element constraints of Eqs. (2.23),(2.27) transformed in the global system become:

$$\vec{h}_g^A = \mathbf{V}_1 \vec{d}_g - \Lambda^T \left[\sum_{i=1}^n w_i \mathbf{R}_i (\vec{q}_i + \vec{E}_1) - \ell \vec{E}_1 \right] \quad (2.32a)$$

$$\vec{h}_g^B = \vec{\phi} - \mathbf{V}_2 \vec{d}_g - \mathbf{T} \vec{\kappa} \quad (2.32b)$$

where:

$$\mathbf{V}_1 = \begin{bmatrix} -\mathbf{I} & \mathbf{I} \end{bmatrix} \quad , \quad \mathbf{V}_2 = \begin{bmatrix} \vec{0} & \vec{0} & \vec{1} & \vec{0} & \vec{0} & \vec{0} \end{bmatrix}$$

$$\mathbf{I} = \begin{bmatrix} 1 & 0 & 0 \\ 0 & 1 & 0 \\ 0 & 0 & 1 \end{bmatrix} \quad , \quad \vec{0} \in \mathbb{R}^n$$

In the equation above the superscript denoting an element is ommited for clarity. The element

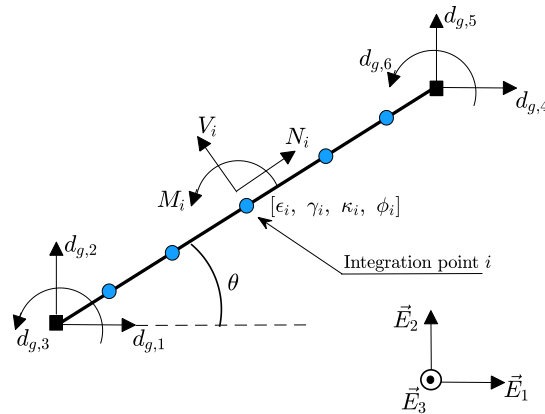


Fig. 2.3. Typical element representing one member.

contribution to the Lagrangian of the assemblage, denoted \mathcal{E}^e , is then:

$$\mathcal{E}^e(\vec{\mathbf{y}}_1, \dots, \vec{\mathbf{y}}_n, \vec{\mathbf{d}}_g, \vec{\lambda}^e) = U^e + (\vec{\lambda}^e)^T \vec{\mathbf{h}}_g^e \quad (2.33)$$

Notice that the external potential function W is not included in Eq. (2.33) as it is added directly via the work done by external forces in the global degrees of freedom and not from element contributions. The element Lagrange multipliers $\vec{\lambda}^e$ are force conjugate measures at the corresponding degrees of freedom and U^e is the sum total of cross-section strain energies. The Lagrangian of the whole system is accordingly given by:

$$\mathcal{L}(\vec{\mathbf{y}}, \vec{\mathbf{d}}_g, \vec{\lambda}) = U - W + \vec{\lambda}^T \vec{\mathbf{h}}_g \quad (2.34)$$

which is a restatement of Eq. (2.30) in the global coordinate system and $\vec{\mathbf{y}} = \begin{bmatrix} \vec{\mathbf{y}}_1^T & \vec{\mathbf{y}}_2^T & \cdots & \vec{\mathbf{y}}_m^T \end{bmatrix}^T$, with m being the total number of quadrature points in the structure.

2.4.1 Equilibrium

In what follows, it is assumed we are dealing with quantities pertaining to the total assemblage, after all element contributions have been resolved. The first-order necessary optimality condition for the Lagrangian function (see Eq. (2.17)), after the imposition of boundary conditions, yields the following relations:

$$\nabla_{\mathbf{y}_i} \mathcal{L} = \nabla_{\mathbf{y}_i} U + [\nabla_{\mathbf{y}_i} \vec{\mathbf{h}}_g] \vec{\lambda} = \vec{0} \quad (2.35a)$$

$$\nabla_{\mathbf{d}_g} \mathcal{L} = -\nabla_{\mathbf{d}_g} W + [\nabla_{\mathbf{d}_g} \vec{\mathbf{h}}_g] \vec{\lambda} = \vec{0} \quad (2.35b)$$

$$\nabla_{\lambda} \mathcal{L} = \vec{\mathbf{h}}_g = \vec{0} \quad (2.35c)$$

Eq. (2.35a) expresses the equilibrium between external and internal forces acting on the i -th cross-section for $i = 1, 2, \dots, m$, while Eq. (2.35b) ensures consistency between externally

applied loads and Lagrange multipliers. Finally, Eq. (2.35c) requires that all constraints are active when the minimum is attained. Explicit expressions for the first and second derivatives of all quantities involved are given in the Appendix. We should note that derivatives of the strain energy U are computed numerically during the cross-section state determination phase in Sec. (2.4.3).

2.4.2 Hessian matrix

The Hessian matrix of the Lagrangian function contains second order information of the system and is utilized during the solution phase. Eqs. (2.35a)-(2.35c) constitute a set of nonlinear algebraic equations and an iterative scheme is needed to solve the system. In block matrix form, the Hessian is provided as:

$$\mathbf{H} = \begin{bmatrix} \nabla_{\mathbf{y}\mathbf{y}}^2 \mathcal{L} & \nabla_{\mathbf{y}\mathbf{d}_g}^2 \mathcal{L} & \nabla_{\mathbf{y}\lambda}^2 \mathcal{L} \\ \nabla_{\mathbf{y}\mathbf{d}_g}^2 \mathcal{L}^T & \nabla_{\mathbf{d}_g\mathbf{d}_g}^2 \mathcal{L} & \nabla_{\mathbf{d}_g\lambda}^2 \mathcal{L} \\ \nabla_{\mathbf{y}\lambda}^2 \mathcal{L}^T & \nabla_{\mathbf{d}_g\lambda}^2 \mathcal{L}^T & \nabla_{\lambda\lambda}^2 \mathcal{L} \end{bmatrix} = \begin{bmatrix} \nabla_{\mathbf{y}\mathbf{y}}^2 \mathcal{L} & \mathbf{0} & \nabla_{\mathbf{y}} \vec{\mathbf{h}}_g^T \\ \mathbf{0} & \mathbf{0} & \nabla_{\mathbf{d}_g} \vec{\mathbf{h}}_g^T \\ \nabla_{\mathbf{y}} \vec{\mathbf{h}}_g & \nabla_{\mathbf{d}_g} \vec{\mathbf{h}}_g & \mathbf{0} \end{bmatrix} \quad (2.36)$$

The resulting Hessian is fairly sparse. Moreover, the block matrix $\nabla_{\mathbf{y}\mathbf{y}} U$ which contains section stiffness information is block-diagonal (see Appendix B) and its symmetry guarantees the full symmetry of \mathbf{H} .

2.4.3 Solution scheme

As mentioned in Appendix B, the nonlinear system of equations in Eq. (2.17) is solved in an incremental-iterative fashion. Linearization around the current iteration k yields:

$$\nabla \mathcal{L}^k + \mathbf{H}^k \delta \vec{\mathbf{z}}^k = \vec{\mathbf{0}} \quad (2.37)$$

where \vec{z} is the vector of all unknowns:

$$\vec{z} = \begin{bmatrix} \vec{y} \\ \vec{d}_g \\ \vec{\lambda} \end{bmatrix}, \quad \text{with} \quad \vec{y} = \begin{bmatrix} \vec{y}_1 \\ \vdots \\ \vec{y}_m \end{bmatrix}$$

Reference to the current iteration step is omitted subsequently for clarity. Solving Eq. (2.37) directly may be cumbersome in some cases, especially for problems that require denser distribution of integration points (e.g. plasticity), since the Hessian is not banded and may also be badly conditioned. In addition, implementation of continuation schemes in order to attain solutions past critical points is more involved since the state variable vector contains displacements, strains and Lagrange multiplier unknowns. A different approach is hence sought, where the initial linear system is reduced to a smaller one involving only the displacement vector \vec{d}_g .

Restating the system in terms of its distinct vector components \vec{y} , \vec{d}_g and $\vec{\lambda}$ gives:

$$\begin{bmatrix} \nabla_y \mathcal{L} \\ \nabla_{d_g} \mathcal{L} \\ \nabla_\lambda \mathcal{L} \end{bmatrix} + \begin{bmatrix} \nabla_{yy}^2 \mathcal{L} & \mathbf{0} & \nabla_y \vec{h}_g^T \\ \mathbf{0} & \mathbf{0} & \nabla_{d_g} \vec{h}_g^T \\ \nabla_y \vec{h}_g & \nabla_{d_g} \vec{h}_g & \mathbf{0} \end{bmatrix} \begin{bmatrix} \delta \vec{y} \\ \delta \vec{d}_g \\ \delta \vec{\lambda} \end{bmatrix} = \begin{bmatrix} \vec{0} \\ \vec{0} \\ \vec{0} \end{bmatrix} \quad (2.38)$$

Utilizing Eqs. (2.35a)-(2.35c) and setting $\delta \vec{\lambda} = \vec{\lambda}^{k+1} - \vec{\lambda}^k$, Eq. (2.38) can be rewritten as:

$$\begin{bmatrix} \nabla_y U \\ -\vec{P} \\ \vec{h}_g \end{bmatrix} + \begin{bmatrix} \nabla_{yy}^2 \mathcal{L} & \mathbf{0} & \nabla_y \vec{h}_g^T \\ \mathbf{0} & \mathbf{0} & \nabla_{d_g} \vec{h}_g^T \\ \nabla_y \vec{h}_g & \nabla_{d_g} \vec{h}_g & \mathbf{0} \end{bmatrix} \begin{bmatrix} \delta \vec{y} \\ \delta \vec{d}_g \\ \vec{\lambda}_{k+1} \end{bmatrix} = \begin{bmatrix} \vec{0} \\ \vec{0} \\ \vec{0} \end{bmatrix} \quad (2.39)$$

As mentioned previously, the gradient of the strain energy with respect to the strain vector represents the cross-sectional stress resultants. Solving the first equation in the system of Eq.

(2.39) for $\delta\vec{y}$ we get:

$$\delta\vec{y} = -\nabla_{yy}^2 \mathcal{L}^{-1} \left[\vec{F}_{sec} + \nabla_y \vec{h}_g^T \vec{\lambda}_{k+1} \right] \quad (2.40)$$

Substituting Eq. (2.40) in the third equation of Eq. (2.39) and solving for $\vec{\lambda}^{k+1}$ yields:

$$\vec{\lambda}^{k+1} = \mathbf{B}^{-1} [\vec{h}_g - \vec{b}] + \mathbf{B}^{-1} [\nabla_{d_g} \vec{h}_g] \delta \vec{d}_g \quad (2.41)$$

By substituting Eq. (2.41) into the second system equation Eq. (2.35b) we arrive at the familiar static equilibrium form of the system of equations:

$$\mathbf{K} \delta \vec{d}_g = \vec{P} - \vec{F}_{int} \quad (2.42)$$

which can now be solved for the iterative displacement vector $\delta \vec{d}_g$. Vectors \vec{b} , \vec{F}_{int} and matrices \mathbf{B} , \mathbf{K} , are given by the following explicit formulas in the global system:

$$\vec{b} = [\nabla_y \vec{h}_g] [\nabla_{yy}^2 \mathcal{L}]^{-1} \vec{F}_{sec} \quad (2.43a)$$

$$\vec{F}_{int} = [\nabla_{d_g} \vec{h}_g]^T [\mathbf{B}]^{-1} [\vec{h}_g - \vec{b}] \quad (2.43b)$$

$$\mathbf{B} = [\nabla_y \vec{h}_g] [\nabla_{yy}^2 \mathcal{L}]^{-1} [\nabla_y \vec{h}_g]^T \quad (2.43c)$$

$$\mathbf{K} = [\nabla_{d_g} \vec{h}_g]^T [\mathbf{B}]^{-1} [\nabla_{d_g} \vec{h}_g] \quad (2.43d)$$

where $\vec{b} \in \mathbb{R}^p$, $\vec{F}_{int} \in \mathbb{R}^{3N}$, N is again the number of structural nodes, $\mathbf{B} \in \mathbb{R}^{p \times p}$ with $p = m + 3n_{nel}$, and $\mathbf{K} \in \mathbb{R}^{3N \times 3N}$.

Equivalently, an assembly process can also be implemented by casting Eqs. (2.43a), (2.43c) in local form, where they can be further simplified by being expanded in terms of element

cross-section contributions:

$$\vec{\mathbf{b}}^e = \sum_{i=1}^n [\nabla_{\mathbf{y}_i} \vec{\mathbf{h}}_g] [\nabla_{\mathbf{y}_i}^2 \mathcal{L}]^{-1} \vec{\mathbf{F}}_{sec}^{(i)} \quad (2.44a)$$

$$\mathbf{B}^e = \sum_{i=1}^n [\nabla_{\mathbf{y}_i} \vec{\mathbf{h}}_g] [\nabla_{\mathbf{y}_i}^2 \mathcal{L}]^{-1} [\nabla_{\mathbf{y}_i} \vec{\mathbf{h}}_g]^T \quad (2.44b)$$

where n is the number of element quadrature points, $\vec{\mathbf{b}}^e \in \mathbb{R}^{n+3}$ and $\mathbf{B}^e \in \mathbb{R}^{(n+3) \times (n+3)}$. The element stiffness matrix $\mathbf{K}^e \in \mathbb{R}^{6 \times 6}$ and internal force vector $\vec{\mathbf{F}}_{int}^e \in \mathbb{R}^6$ are given by the same expressions as in Eqs. (2.43b), (2.43d), but with the gradients now cast in the local element form. For the assembly, the standard FEM routines can be directly employed and the resulting global stiffness operator retains all properties typically associated with it in the context of classical finite element analysis, i.e. it is a symmetric positive definite matrix, it is well-conditioned and, importantly, it is sparse and banded. Hence, in this case, the global internal force vector and the global stiffness matrix are given by the standard assembly process, designated here via operator Λ :

$$\vec{\mathbf{F}}_{int} = \prod_{e=1}^{n_{el}} \vec{\mathbf{F}}_{int}^e \quad (2.45)$$

$$\mathbf{K} = \prod_{e=1}^{n_{el}} \mathbf{K}^e \quad (2.46)$$

with

$$\vec{\mathbf{F}}_{int}^e = [\nabla_{\mathbf{d}_g} \vec{\mathbf{h}}_g^e]^T [\mathbf{B}^e]^{-1} [\vec{\mathbf{h}}_g^e - \vec{\mathbf{b}}^e] \quad (2.47)$$

$$\mathbf{K}^e = [\nabla_{\mathbf{d}_g} \vec{\mathbf{h}}_g^e]^T [\mathbf{B}^e]^{-1} [\nabla_{\mathbf{d}_g} \vec{\mathbf{h}}_g^e] \quad (2.48)$$

where $\vec{\mathbf{h}}_g^e \in \mathbb{R}^{n+3}$ denotes the *element* constraint vector given by Eq. (2.28) and $\nabla_{\mathbf{d}_g} \vec{\mathbf{h}}_g^e \in \mathbb{R}^{(n+3) \times 6}$ its gradient with respect to the global displacement degrees of freedom (DOFs) asso-

ciated with it, is given in Appendix A. It is clear that with this formulation the inversion of large global matrices for the computation of \mathbf{K} and $\vec{\mathbf{F}}_{int}$ is avoided and, instead, only inversion of the local elements flexibility matrices \mathbf{B}^e is required. Given that for highly nonlinear problems we typically have $n \in \mathbb{N}([5, 10])$ for satisfactory accuracy, this results in an element flexibility matrix of dimension $\dim(\mathbf{B}^e) \leq 13$, thus accelerating the analysis considerably.

Having written the system of equations in the form of Eq. (2.42), implementation of arc-length type schemes is now straightforward. In the present work, we adopt the algorithm proposed by Crisfield [13] whereby the additional equation supplemented to the system is:

$$\Delta \vec{\mathbf{d}}_g^T \Delta \vec{\mathbf{d}}_g = \Delta S^2 \quad (2.49)$$

with ΔS being the user-specified arc-length parameter. The incremental displacement vector $\Delta \vec{\mathbf{d}}_g$ is updated in each iteration as follows:

$$\Delta \vec{\mathbf{d}}_g^k = \Delta \vec{\mathbf{d}}_g^{k-1} + \delta \vec{\mathbf{d}}_g^k \quad (2.50)$$

where k denotes the current iteration and $\delta \vec{\mathbf{d}}_g^k$ is the vector of iterative displacements.

Solution updating

After the determination, at an arbitrary iteration k within step j , of the iterative displacement vector $\delta \vec{\mathbf{d}}_g^k$ from Eq. (2.42), the strain and Lagrange multiplier vectors in Eqs. (2.40),(2.41) have then to be updated. The detailed steps of the updating procedure are as follows:

Step j , iteration k : $\left\{ \vec{\mathbf{y}}_j^0, \quad \vec{\mathbf{d}}_{g,j}^0, \quad \vec{\lambda}_j^0, \quad \vec{\mathbf{P}}_j, \quad \Delta \vec{\mathbf{y}}_j^{k-1}, \quad \Delta \vec{\mathbf{d}}_{g,j}^{k-1} \right\}$

(1): Get section stiffnesses $\nabla_{\mathbf{y}\mathbf{y}}^2 \mathcal{L}^k$ from Eq. (B.3) in Appendix B and section forces $\vec{\mathbf{F}}_{sec}^k$ from section integration, Eq. (2.55).

(2): Evaluate $\vec{\mathbf{b}}^k$ and \mathbf{B}^k from Eqs. (2.43a), (2.43c) respectively (or, alternatively, $\vec{\mathbf{b}}^{e,k}$, $\mathbf{B}^{e,k}$ from Eqs. (2.44a), (2.44b)).

(3): Evaluate \mathbf{K}^k from Eq. (2.43d), (or, alternatively, from Eqs. (2.46), (2.48)).

(4): Solve Eq. (2.42) for $\delta\vec{\mathbf{d}}_g^k$.

(5): Update incremental displacement vector: $\Delta\vec{\mathbf{d}}_{g,j}^k \leftarrow \Delta\vec{\mathbf{d}}_{g,j}^{k-1} + \delta\vec{\mathbf{d}}_g^k$

(6): Update displacement vector: $\vec{\mathbf{d}}_{g,j}^k \leftarrow \vec{\mathbf{d}}_{g,j}^0 + \Delta\vec{\mathbf{d}}_g^k$

(7): Update Langrange multiplier $\vec{\lambda}_j^k$ from Eq. (2.41).

(8): Evaluate iterative strain vector $\delta\vec{\mathbf{y}}^k$ from Eq. (2.40).

(9): Update incremental strain vector: $\Delta\vec{\mathbf{y}}_j^k \leftarrow \Delta\vec{\mathbf{y}}_j^{k-1} + \delta\vec{\mathbf{y}}^k$

(10): Update total strain vector: $\vec{\mathbf{y}}_j^k \leftarrow \vec{\mathbf{y}}_j^0 + \Delta\vec{\mathbf{y}}_j^k$

(11): Evaluate $\vec{\mathbf{F}}_{int}^k$ from Eq. (2.43b) (or, alternatively, from Eqs. (2.45), (2.47)).

(12): Check $\|\vec{\mathbf{P}}_j - \vec{\mathbf{F}}_{int}^k\| \leq \text{tol} \cdot \|\vec{\mathbf{P}}_j - \vec{\mathbf{F}}_{int}^0\|$.

(13): If **FALSE**, set $k \leftarrow k + 1$ and go to (1). If **TRUE**, set $j \leftarrow j + 1$, $\vec{\mathbf{y}}_j^0 \leftarrow \vec{\mathbf{y}}_{j-1}^k$, $\vec{\mathbf{d}}_{g,j}^0 \leftarrow \vec{\mathbf{d}}_{g,j-1}^k$, $\vec{\lambda}_j^0 \leftarrow \vec{\lambda}_{j-1}^k$.

2.4.4 Cross-section state determination

During the updating scheme described in the previous section, the section stress resultants $\vec{\mathbf{F}}_{sec}$, along with the matrix $\nabla_{yy}^2 \mathcal{L}$, are required. The latter, as seen subsequently, corresponds to the generalized section stiffnesses. In the general case where inelastic behavior is considered, the stress-strain constitutive law has to be integrated at the cross-section level and the material properties have to be updated accordingly. In this work, each cross-section is discretized in n_l number of layers and the stress update is performed independently for each layer. This is equivalent to the composite midpoint rule applied along the height of the cross-section. The shear coefficient k_s is introduced as a correction factor for the simplifying aforementioned assumption, in accordance with Cowper [14].

Below we present the kinematic and constitutive relations for a cross-section object. The (multiaxial) constitutive law at the fiber level is treated in the next chapter. The update procedure is regarded as strain-driven, in the sense that the known initial state is updated given an increment in the centerline strains at a particular quadrature point. First, we define the stress and strain vectors associated with a particular fiber:

$$\vec{\sigma}_f = \begin{bmatrix} \sigma_{11} & \sigma_{12} \end{bmatrix}^T, \quad \vec{\epsilon}_f = \begin{bmatrix} \epsilon_{11} & \gamma_{12} \end{bmatrix}^T \quad (2.51)$$

In line with the plane section hypothesis, the fiber strain vector can be determined from the centerline strain vector as follows:

$$\begin{aligned} \epsilon_{11} &= \varepsilon - X_2 \kappa \\ \gamma_{12} &= \varphi(X_2) \gamma \end{aligned} \iff \vec{\epsilon}_f = \mathbf{N}_s \vec{q}, \quad \mathbf{N}_s = \begin{bmatrix} 1 & 0 & -X_2 \\ 0 & \varphi(X_2) & 0 \end{bmatrix} \quad (2.52)$$

where $\varphi(X_2)$ is an as of now unspecified function that defines a shear strain distribution along the height of the cross-section.

Thus, given $\{\vec{q}, \vec{q}^{pl}\}$, $\Delta\vec{q}$, along with a set of internal state variables (e.g. accumulated plastic strain), we can evaluate the incremental strains at the midpoint of a layer at distance X_2 from the neutral axis as follows:

$$\vec{\epsilon}_f = \mathbf{N}_s \vec{q} \quad (2.53a)$$

$$\Delta\vec{\epsilon}_f = \mathbf{N}_s \Delta\vec{q} \quad (2.53b)$$

where it is reminded that \vec{q} is the vector containing the neutral axis generalized strains and $\vec{\epsilon}_f$ is the strain vector associated with the fiber midpoint. With Eqs. (2.53a), (2.53b) and the initial state known, we can perform the stress update which will yield the updated stress vector $\vec{\sigma}_f$ and the (consistent) elastoplastic modulus for the fiber. The conjugate stress resultants associated with the assumed kinematic assumptions are derived from the element virtual work equation:

$$\vec{P}_l^T \delta \vec{d}_l + \vec{P}_r^T \delta \vec{d}_r = \int_V \vec{\sigma}_f^T \delta \vec{\epsilon}_f \, dV = \int_0^L \left[\int_A \mathbf{N}_s^T \vec{\sigma}_f dA \right]^T \vec{q} \, dX_1 \quad (2.54)$$

where we define the conjugate section stress resultants associated with \vec{q} as follows:

$$\vec{F}_{sec}^{(i)} = \int_A \mathbf{N}_s^T \vec{\sigma}_f \, dA \quad (2.55)$$

Application of the composite midpoint rule on Eq. (2.55) yields:

$$\vec{F}_{sec}^{(i)} \approx \begin{bmatrix} \sum_{j=1}^{n_l} \sigma_{11,j} \Delta A_j \\ \sum_{j=1}^{n_l} \sigma_{12,j} \Delta A_j \\ \sum_{j=1}^{n_l} X_{2,j} \sigma_{11,j} \Delta A_j \end{bmatrix} \quad (2.56)$$

where ΔA_j the area of layer j .

Let $\mathbf{C} = \partial \vec{\sigma}_f / \partial \vec{\epsilon}_f$ designate the tangent modulus at a fiber. During elastic steps, $\mathbf{C} \equiv \mathbf{C}^{el} = \text{diag}[E, G]$. In the next chapter we will see that during plastic steps the diagonal components of \mathbf{C} are, generally, also non-zero. The tangent section stiffness is derived as follows:

$$\mathbf{k}_{sec}^{(i)} = \frac{\partial \vec{F}_{sec}^{(i)}}{\partial \vec{q}} = \int_A \mathbf{N}_s^T \frac{\partial \vec{\sigma}_f}{\partial \vec{q}} \, dA = \int_A \mathbf{N}_s^T \frac{\partial \vec{\sigma}_f}{\partial \vec{\epsilon}_f} \frac{\partial \vec{\epsilon}_f}{\partial \vec{q}} \, dA = \int_A \mathbf{N}_s^T \mathbf{C} \mathbf{N}_s \, dA \quad (2.57)$$

Application of the midpoint rule on Eq. (2.57) yields the following component form for $\mathbf{k}_s^{(i)}$:

$$\mathbf{k}_{sec}^{(i)} = \begin{bmatrix} C_{11}^i & \varphi^i C_{12}^i & -X_2^i C_{11}^i \\ \varphi^i C_{21}^i & (\varphi^i)^2 C_{22}^i & -x_2^i \varphi^i C_{21}^i \\ -X_2^i C_{11}^i & -x_2^i \varphi^i C_{12}^i & (X_2^i)^2 C_{11}^i \end{bmatrix} \quad (2.58)$$

where C_{ij} are the components of the elastoplastic consistent tangent modulus of the fiber. The

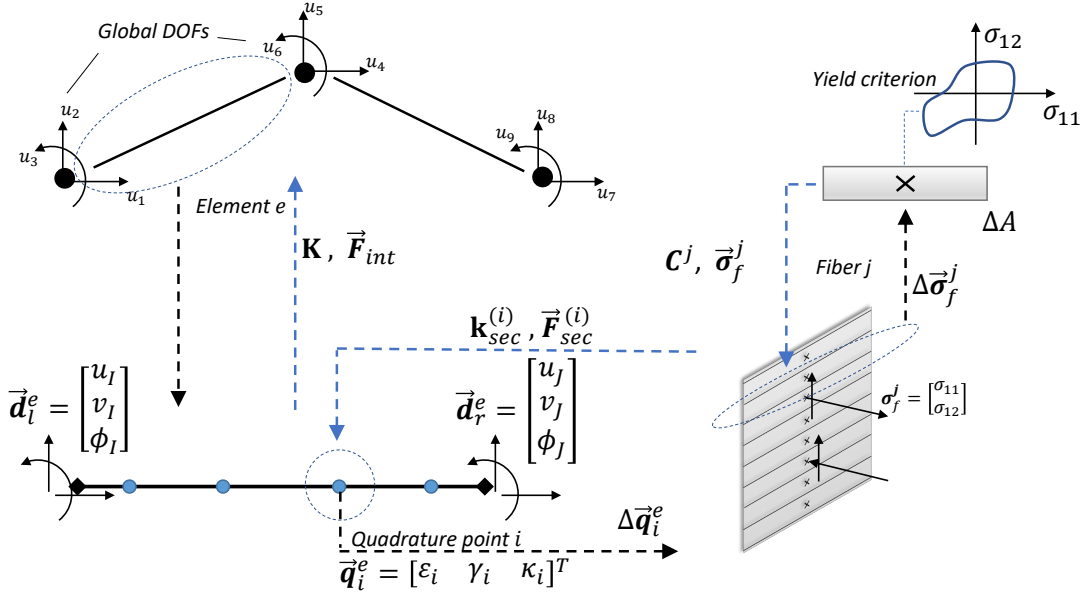


Fig. 2.4. Solution process stages. Quantities \mathbf{K}^e and $\vec{\mathbf{F}}_{int}$ stand for stiffness matrix and internal nodal force vector for element e respectively.

section stiffness is then given by the following sum:

$$\mathbf{k}_{sec} = \sum_{i=1}^{n_f} \mathbf{k}_{sec}^{(i)} \Delta A^i \quad (2.59)$$

Given an increment in nodal displacements at the global/structural level, the assembly process has to loop over all elements in order to determine the element stiffness and internal nodal forces. This procedure, illustrated in Fig. 2.4, involves analysis at three different levels: the global/element, the section state determination, and the fiber stress update. Having briefly outlined the basic theory for the hybrid element as it pertains to the first two levels mentioned above, next we introduce the elastoplastic stress update formulation, which pertains to the third level of the solution process and results in a fast return mapping algorithm.

The generalized section stiffness, $\nabla_{\mathbf{y}_i \mathbf{y}_i}^2 \mathcal{L}$, is given by the second derivatives of the Lagrangian with respect to strain vector $\vec{\mathbf{q}}_i = \begin{bmatrix} \vec{\mathbf{q}}_i^T & \phi_i \end{bmatrix}^T$:

$$\nabla_{\mathbf{y}_i \mathbf{y}_i}^2 \mathcal{L} = \nabla_{\mathbf{y}_i \mathbf{y}_i}^2 U + \nabla_{\mathbf{y}_i} ([\nabla_{\mathbf{y}_i} \vec{\mathbf{h}}_g] \vec{\lambda}) \quad (2.60)$$

where:

$$\nabla_{\mathbf{y}_i \mathbf{y}_i}^2 U = w_i \begin{bmatrix} \mathbf{k}_{sec}^{(i)} & \mathbf{0} \\ \mathbf{0} & 0 \end{bmatrix}$$

For the explicit expression of the second term in the right-hand side of Eq. (2.60), see Appendix B. It generally includes parameters associated with section rotations and Lagrange multipliers, and is greatly simplified if small displacement assumptions are used.

2.5 Numerical Examples

In this section we present the capabilities and efficiency of the proposed element in a number of well-known benchmark examples. In cases where analytical solutions are available, they are included in the comparisons. Our results are compared against the ones achieved i) with the structural FEM software OpenSees[15], using its flexibility-based beam element [5, 16] with five quadrature points and fiber section integration, and ii) with the FEM software Abaqus[17], using plane-stress modeling for the frame members. For the elastic analyses, reduced integration linear quadrilateral elements (CPS4R) were used in Abaqus to avoid shear-locking, while for the elastoplastic simulations, reduced integration quadratic quadrilaterals (CPS8R) elements were used instead. For all cases the Gauss-Legendre quadrature rule is used for approximating the integrals in Eqs. (2.19),(2.22). For the elastoplastic analyses, we assume a linear isotropic hardening law and the elastoplastic modulus is given as a percentage r of the elastic modulus E . Moreover, we assume a rigid rectangular cross-section shape for all cases, with shear coefficient $k_s = 0.870$ [14]. For all examples, the SI units corresponding to material and geometric properties are Pa and m, while for the load units Newton(N) is used. The convergence termination criterion for the iterative procedure was 10^{-7} for all cases. Shear deformation is allowed to occur in all analyses unless stated otherwise.

2.5.1 Cantilever with tip load

In this first example we demonstrate the element performance with fully nonlinear assumptions against available analytical solutions, as well as its locking-free behavior when small displacement assumptions hold.

Nonlinear analyses

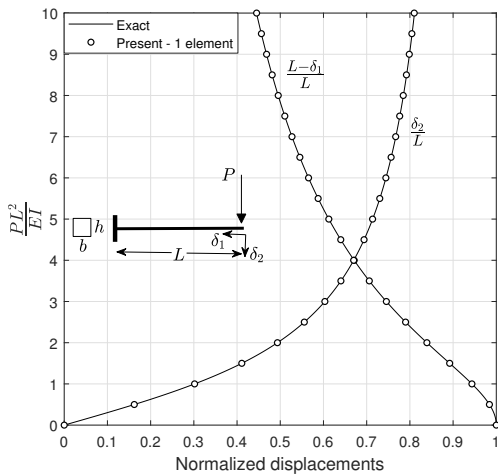
Both elastic and inelastic geometrically nonlinear cases are considered. One element and six integration points are used, with the beam assumed to be inextensible, and the results are presented in Fig. (2.5). The elastic case assumed $EI = 10$, $L = 1$ and shear-rigid response for comparison purposes with available exact equilibrium paths[18], while the inelastic case allows for shear effects to take place with $GA_s = 500$. In order to maintain consistency with the attributes $EI = 10$ and $L = 1$, we used $E = 200 \times 10^9$ for Young's modulus and prescribed the height of the cross-section to be $h = 0.02$, which is now required in order to carry out the cross-sectional stress-update. For the material nonlinearity example, the yield stress is $\sigma_y = 180 \times 10^7$ with a tangent-to-elastic modulus ratio $r = 3\%$ and results are compared against Abaqus and OpenSees. As can be seen in Fig. (2.5), in both cases remarkable accuracy is achieved with just one element. Slight differences between the Abaqus quadrilateral model and the beam models are observed when extensive plastification takes place. In Table 2.1 we also provide distinct comparisons with exact values for the elastic case. It is clear that when the normalized load is equal to 1, displacements remain small, and thus, only $n = 4$ quadrature points suffice to achieve small absolute error. At the maximum load level, however, $n = 6$ quadrature points were required for highly accurate results. For the shear-rigid case exact solutions are computed from numerical evaluation of the elliptic integrals that describe the problem. The reader can also consult Table 1 in [19] for a wide range of values reported. Additional results pertaining to the elastic shear-flexible case are also reported in Table 2.1. For this case, we used again $GA_s = 500$, $EI = 10$, $L = 1$ and compared against available analytical solutions from[20], where the normalized load level therein is held constant and equal to 1. The values correspond-

Table 2.1 Comparison of tip normalized displacements for different load levels for elastic response.

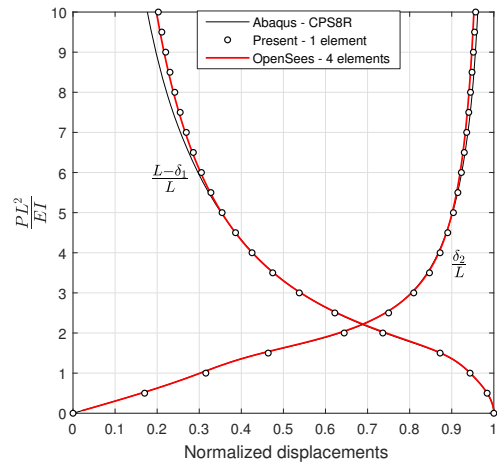
$\frac{PL^2}{EI}$	n	Shear Rigid			Shear Flexible			
		Exact	Present	Error	Exact	Present	Error	
$\frac{\delta_2}{L}$	1	4	0.3017207	0.3017206	1.12E-07	0.3178138	0.3178137	1.64E-07
$\frac{L}{L}$	10	6	0.8106090	0.8106113	2.32E-06	-	0.8536137	-
$\frac{L - \delta_1}{L}$	1	4	0.9435668	0.9435666	1.82E-07	0.9386844	0.9386842	1.75E-07
$\frac{L}{L}$	10	6	0.4450044	0.4450017	2.62E-06	-	0.4208910	-

ing to the maximum normalized load equal to 10 are also reported. Although exact solutions are not available for this load level to compare against, we can see that the relative change in the transverse and axial displacement with respect to the shear-rigid case is consistent and about 5.30% and 5.40%, respectively.

In Fig. (2.6) we see how the moment and curvature distributions change based on the beam deformations for both cases of Fig. (2.5), captured at distinct load levels. The moment values at the left fixed end are also reported on the graphs. The observed nonlinear distributions for the elastic case are due to the deformed shape of the beam being drastically different from its initial configuration. As seen, an important feature of the formulation is its ability to capture curvature localization when plastic hinges are also formed. In displacement-based conventional beam elements, a fine mesh is in constrast required in the areas where plastification is expected.



(a) Elastic analysis



(b) Inelastic analysis

Fig. 2.5. Geometrically nonlinear analyses of cantilever.

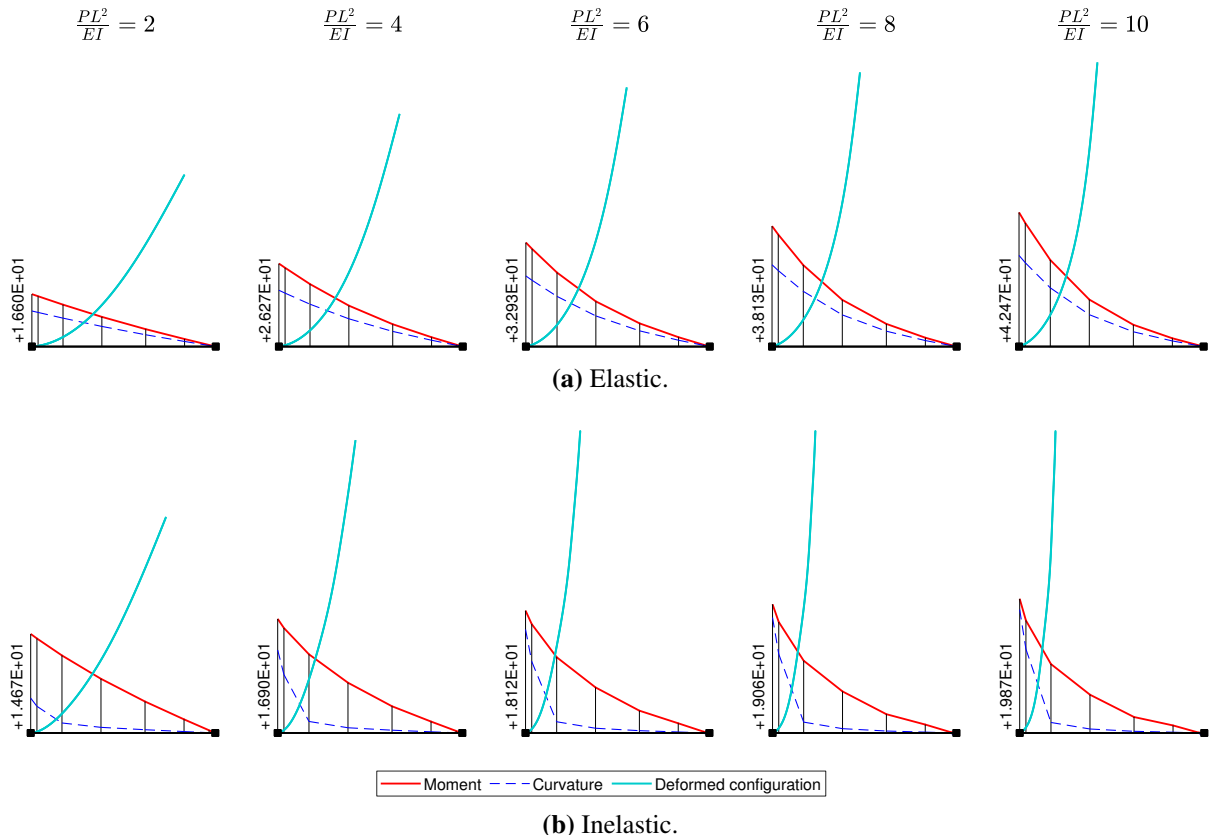


Fig. 2.6. Moment and curvature distributions for the nonlinear analyses of the cantilever - one element with $n = 6$ quadrature points.

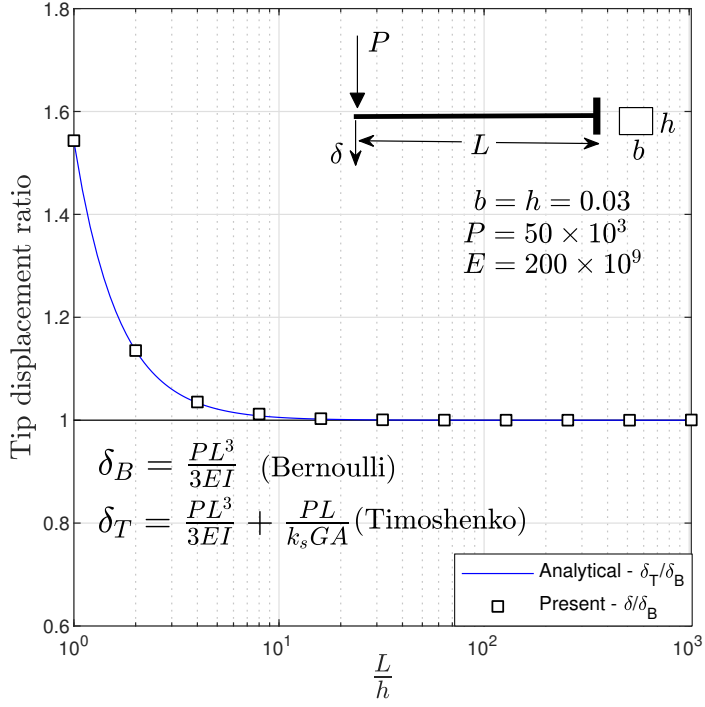


Fig. 2.7. Influence of L/h on the tip deflection and comparison with analytical solution.

Shear-locking

Shear locking may occur in shear deformable elements undergoing bending. Due to inconsistent interpolation of fields that are naturally related, spurious shear stresses develop and the element response appears to be stiffer, particularly as the beam slenderness is increased. Appropriate numerical treatments include using field consistent higher order elements or applying reduced numerical integration [21, 22, 23]. Here, we perform small displacement elastic analyses for various length-to-thickness ratios. The tip displacement ratios of δ_T/δ_B and δ/δ_B are then plotted against the length to thickness ratio L/h , where δ_B and δ_T denote the Bernoulli and Timoshenko displacements respectively. Only one element is used with two integration points. The section dimensions are kept fixed, while the length L of the beam varies. Results, along with used data are shown in Fig. (2.7), where it can be seen that the proposed element exhibits locking-free behavior.

2.5.2 Lee's frame

Lee's frame is a well-known benchmark for geometrically nonlinear capabilities of beam-column element formulations. It was first analyzed by Seng-Lip Lee et.al. in [24] where the exact solution to the problem was also provided. We first consider here the classic case, where the frame is pinned on both supports. An investigation on the effect of shear flexibility to the elastic response is also carried out by varying the length-to-thickness ratio, while maintaining large-displacement assumptions. It is demonstrated that for ratios smaller than five, the equilibrium path ceases to be similar to the shear-rigid case. Lastly, we investigate the response of the same frame when both supports are fixed. This again leads to a drastically different response, with abrupt changes in the equilibrium path. In all cases, the centerline is assumed inextensible.

Frame with pinned supports

An elastic, geometrically nonlinear analysis is first performed. The minimum number of elements that can be used for this specific example is three and a 4-point quadrature is applied for each element, whereas twelve flexibility elements are required in OpenSees to achieve comparable accuracy. For the elastoplastic analysis, again three elements are used in our simulation with eight integration points, whereas fourteen flexibility elements are now required in OpenSees for comparable accuracy. The yield stress is $\sigma_y = 1.3 \times 10^9$ and the tangent-to-elastic modulus is $r = 3.00\%$. In the elastic analysis, the frame members are also considered shear-rigid, in order to remain consistent to the initial assumptions in the original investigation[24]. Results are shown in Fig. (2.8), with the colored markers corresponding to the deformed profiles of the same color shown in Fig. (2.9).

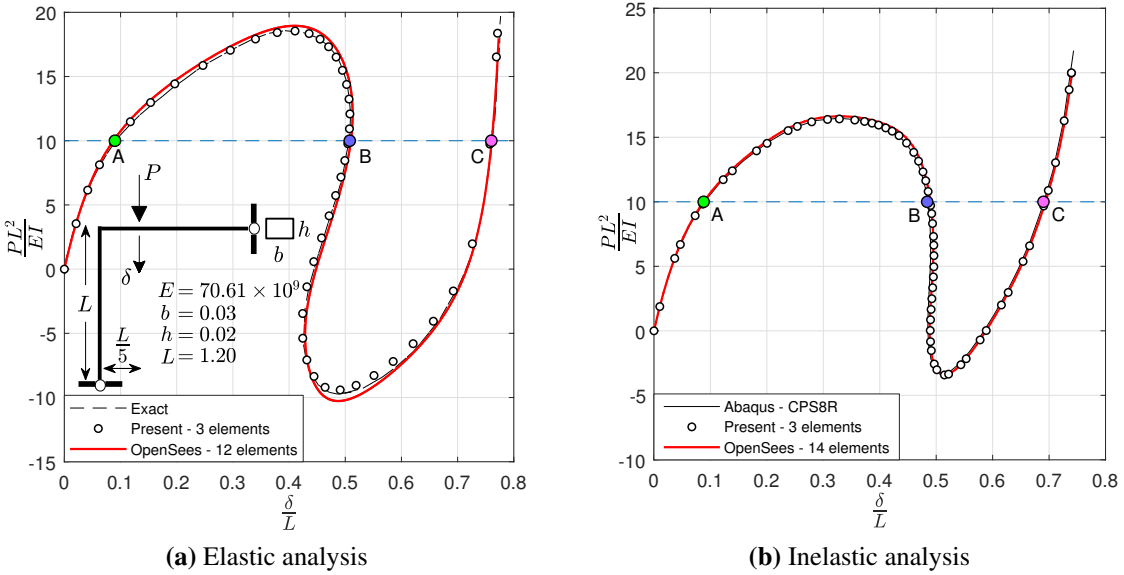


Fig. 2.8. Geometrically nonlinear analyses of Lee's frame with pinned supports.

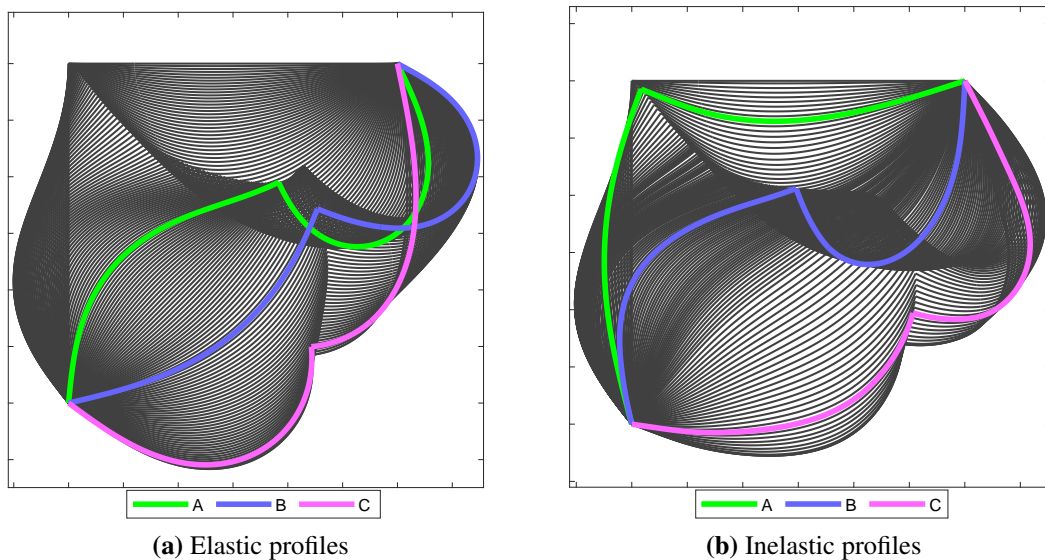


Fig. 2.9. Deformation profiles for Lee's frame with pinned supports.

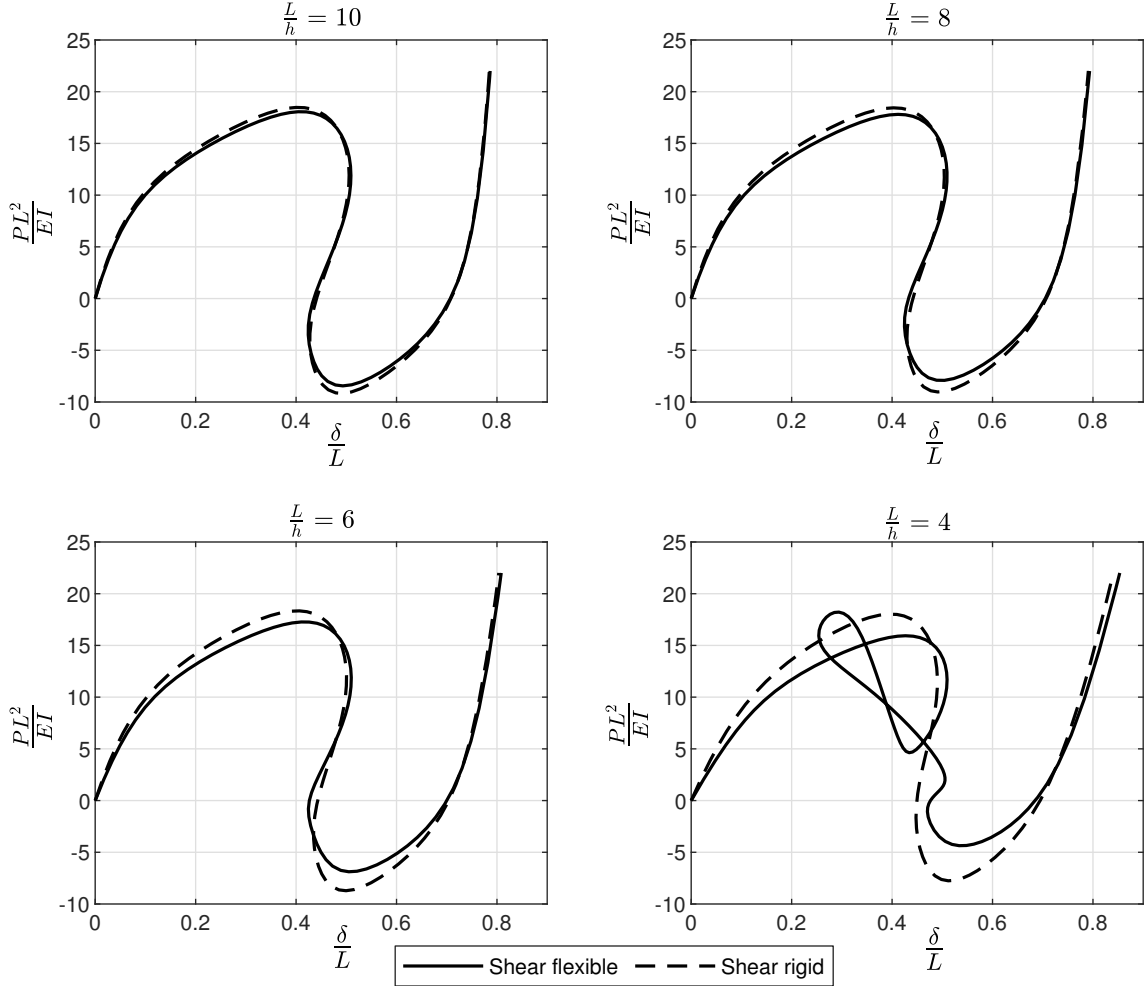


Fig. 2.10. Effect of shear flexibility on Lee's frame response.

In Fig. (2.10), results related to shear flexibility effects on the frame's response are shown. As previously mentioned, in [24] the members are assumed to be shear rigid, effectively adhering to the Bernoulli assumptions. In this example, we relax this assumption and examine how the slenderness decrease affects the structural response. As seen in the figure, four different length-to-thickness ratios are examined and the equilibrium path gradually deviates from the shear-rigid case. For ratio $L/h = 4$, the equilibrium path is drastically different and the structure, after entering the snap-back region, follows a rather complex equilibrium branch. Note that around $\delta/L = 0.5$, the structure exits its current branch and continues on a similar path as in the previous cases.

Frame with fixed supports

This variation of the benchmark problem results in a response that exhibits a dramatic snap-back, with abrupt changes in the stiffness sign along the equilibrium path for the nonlinear elastic problem. Seven integration points are used here per element and, again, one element per member, to achieve the same accuracy as with the Abaqus plane stress model, which terminated prematurely. In contrast, twenty elements are necessary in OpenSees for comparable results. The geometric and material properties are the same as in Sec. (2.5.2) (see Fig. (2.8)). For the inelastic analysis, five integration points are sufficient, since the response is now fairly smooth overall, in comparison to the elastic case. All members are shear flexible in these examples, however the contribution of shear deformation to the overall responses is negligible for both elastic and inelastic cases. The response and deformation profiles for both analyses are shown in Figs. (2.12),(2.11) respectively.

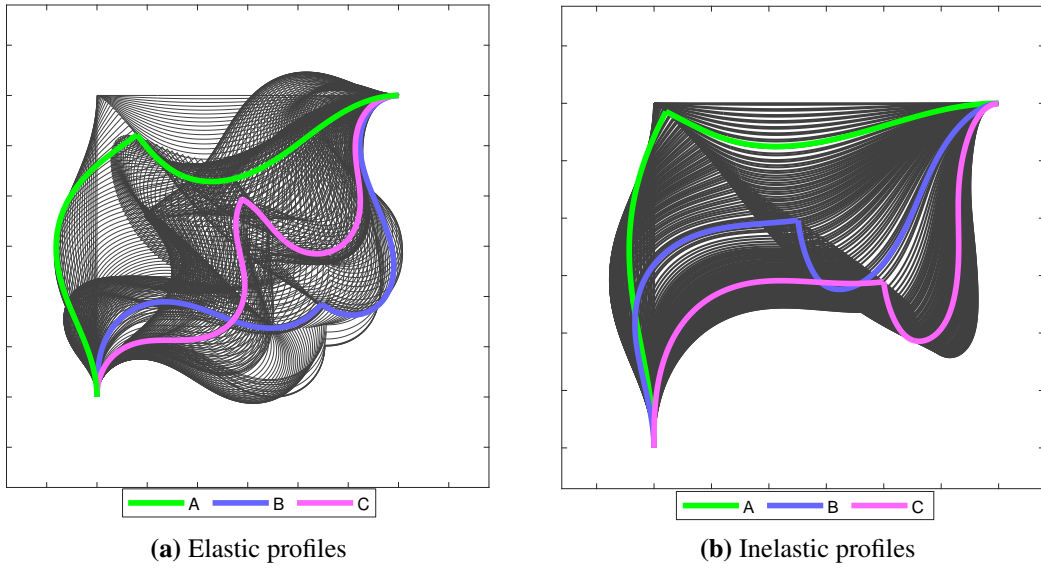


Fig. 2.11. Deformation profiles for Lee's frame with fixed supports.

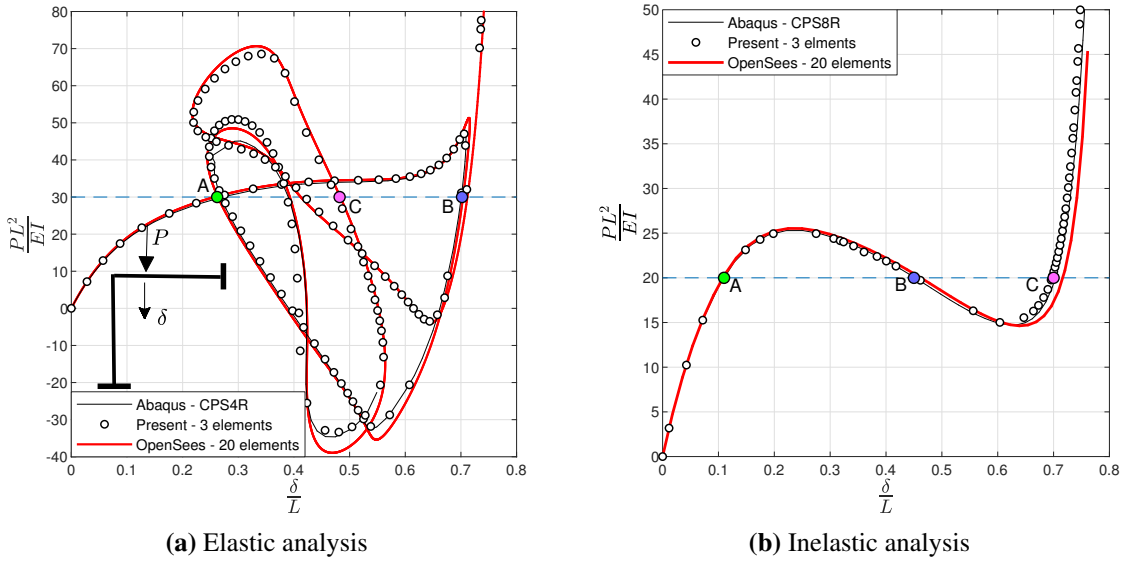


Fig. 2.12. Geometrically nonlinear analyses of Lee's frame with fixed supports.

2.5.3 Two-Storey frame

In this example a two-story frame with one bay is analyzed, first studied regarding its plastic limit load in [25]. It was also later used as a benchmark example by Santos [26], for the performance of a nonlinear beam finite element based on complementary energy principles. The example is slightly modified here, however the rectangular cross-section dimensions of the structural members and their length L have been chosen so their the slenderness remains in accordance with [26]. The yield stress is $\sigma_y = 0.9 \times 10^6$, and the tangent-to-elastic modulus ratio is $r = 3\%$. The full frame characteristics and discretization are shown in Fig. (2.13).

The minimum number of hybrid elements for this example is eight and the number of integration points per element for the elastic and plastic analyses are seven and ten, respectively. For the OpenSees analyses, 36 and 48 elements were used in total for the elastic and inelastic analyses. In both cases, however, the OpenSees analyses stopped prematurely. Results are demonstrated in Fig. (2.14), showing excellent agreement with Abaqus results, while the relevant deformation profiles are provided in Fig. (2.15).

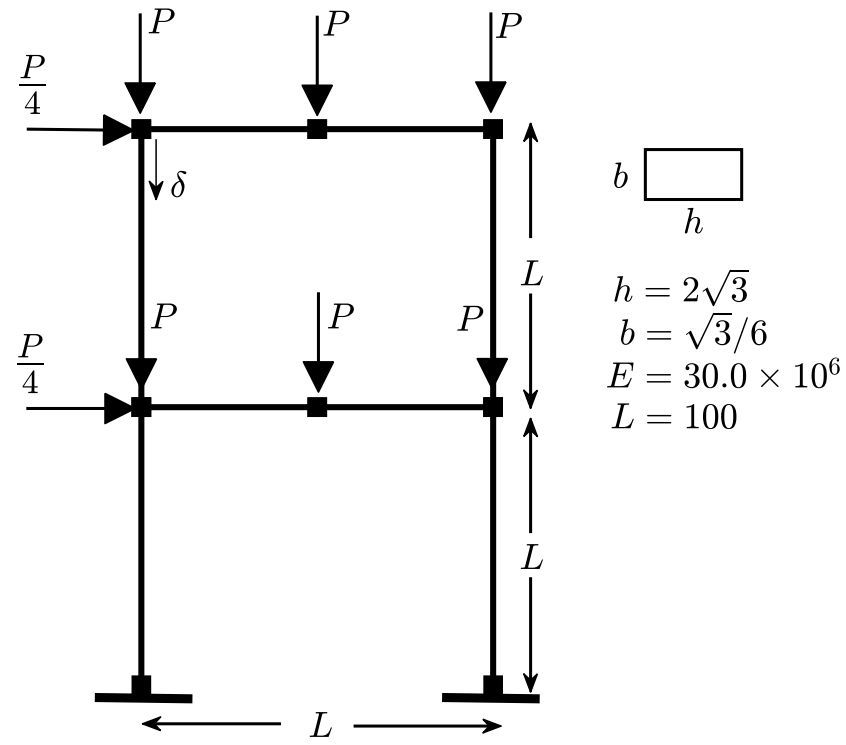


Fig. 2.13. Two-storey portal frame discretization.

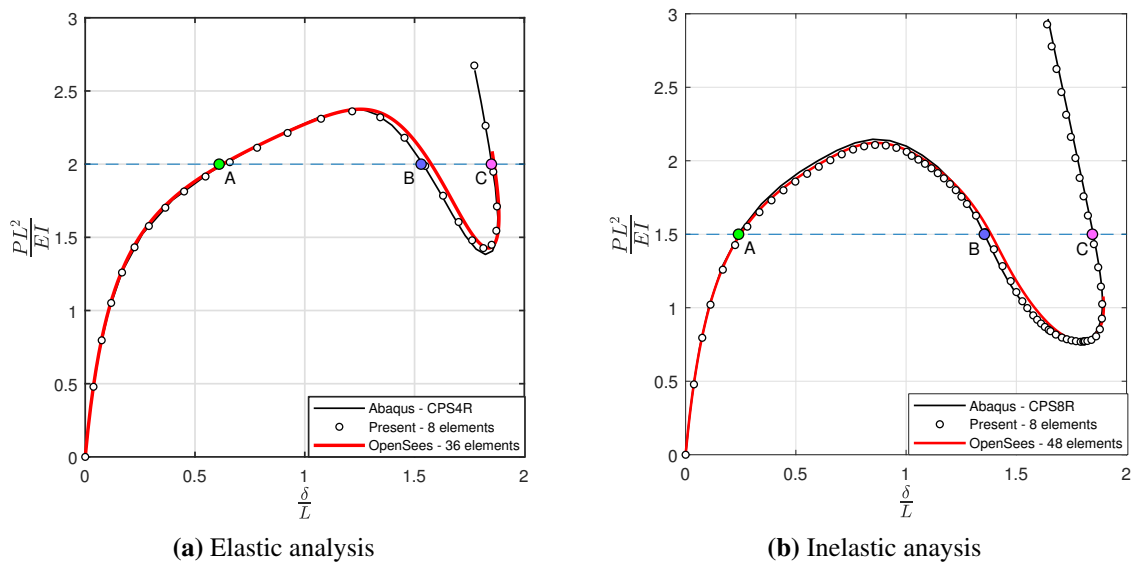


Fig. 2.14. Geometrically nonlinear analyses of the two-storey frame.

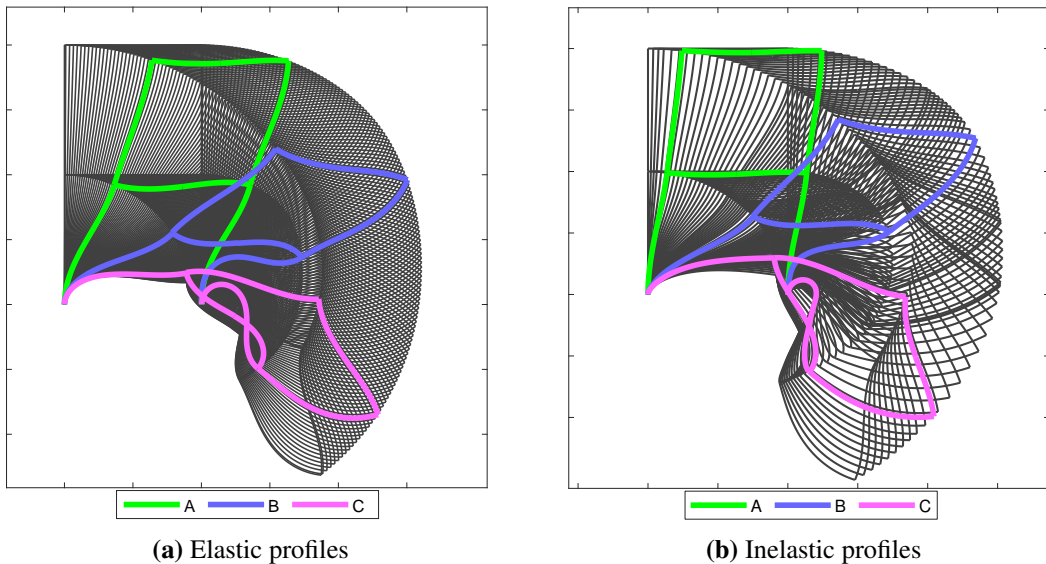


Fig. 2.15. Deformation profiles for two-storey frame.

CHAPTER 3

MATERIAL CONSTITUTIVE MODEL

3.1 Introduction

In this chapter we introduce an algorithm for shear-axial-flexure interaction suited for fibre beam elements of any kind (displacement-based or otherwise). The coupling is taken into account by considering a multiaxial constitutive law at the level of cross-section fibers. Thus, stress resultant interaction as well as the consistent tangent stiffness of a cross-section are derived during the state determination phase. Integration of the elastoplastic rate equations on each fiber is carried out using the fully backward (implicit) Euler method, which as is known, results in the so-called closest point projection algorithm. In addition, the constrained stress state of a fiber is exploited in order to devise a return-mapping scheme that avoids incorporating stress components that are not energetically active. The appropriate mapping on the constrained space is inspirited by the work of Simo[27] and appropriately adapted for fibre discretized elements. This leads to a stress update algorithm that is significantly faster while also requiring less memory requirements for storage of non-active tensor components, compared to formulations that utilize a general three dimensional algorithm[28, 29, 30, 31, 32]. In the latter case, stress update is a nested procedure within an outer Newton iteration which is necessitated in order to enforce the constraint for the transverse stress components, $\sigma_{22} = \sigma_{33} = 0$. This is because during the trial phase of a plastic step, the transverse components become non-zero. Furthermore, a static condensation of the three-dimensional consistent tangent is required to enforce both the local Newton scheme and to derive the consistent tangent modulus pertaining to the fiber stress state. The algorithm introduced in this chapter bypasses the need for additional outer iterations, thereby resulting in a much faster stress update procedure.

For the exposition we adopted the *J2* constitutive model which is based on the von Mises

yield criterion, which is suited for modelling the elastoplastic response of metals. Linear kinematic and general isotropic hardening are incorporated in the formulation. Moreover, infinitesimal strains and a rate-independent associative plasticity framework are the core assumptions that underlie the proposed algorithm. This chapter is subdivided in three main sections: first, we briefly outline the general (rate) form of the three-dimensional elastoplastic equations. In the second section we present the rate constitutive model as it pertains to the fiber stress state and derive expressions for the continuous elastoplastic moduli. In the third section we outline the implementation details, which are based on application of the fully implicit Euler scheme. In addition we derive the expression for the consistent tangent modulus at a fiber, which is required to ensure quadratic rates of convergence for the global Newton method. Finally, we conclude this chapter with a section dedicated to the assessment of the proposed algorithm. Accuracy is demonstrated through iso-error maps for both perfect and hardening plasticity. Furthermore, we compare the performance in terms of total plastic step iterations required for i) the present formulation, ii) the general, three-dimensional and iii) the plane stress return mapping algorithm developed in [27]. Numerical examples pertaining to ultimate collapse load, cyclic loading, elastoplastic buckling and a pushover analysis of a steel frame are also included to highlight the capabilities of the Hybrid NLP element equipped with the multiaxial stress-update algorithm proposed herein.

3.2 Three-dimensional Constitutive Model

Below we outline the general rate form of rate-independent elastoplasticity with combined isotropic and linear kinematic hardening. Infinitesimal strains and associative plasticity are assumed, while the yield criterion is purposefully unspecified at this stage in order to maintain generality.

Let σ , ϵ be the second order symmetric stress and strain tensors. We introduce the internal hardening variables α and q which represent the second order back-stress tensor and the equivalent uniaxial yield stress respectively. The former is associated with kinematic hardening

while the latter models isotropic hardening. Finally, consider the decomposition of the strain tensor into elastic and plastic parts as follows:

$$\boldsymbol{\epsilon} = \boldsymbol{\epsilon}^{el} + \boldsymbol{\epsilon}^{pl} \quad (3.1)$$

Then the rate form of the constitutive equations for the assumptions mentioned above is the following:

$$\dot{\boldsymbol{\epsilon}} = \dot{\boldsymbol{\epsilon}}^{el} + \dot{\boldsymbol{\epsilon}}^{pl} \quad (\text{Strain decomposition}) \quad (3.2a)$$

$$\dot{\boldsymbol{\sigma}} = \mathbb{C}^{el} [\dot{\boldsymbol{\epsilon}} - \dot{\boldsymbol{\epsilon}}^{pl}] \quad (\text{Elastic constitutive law}) \quad (3.2b)$$

$$\dot{\boldsymbol{\epsilon}}^{pl} = \dot{\lambda} \frac{\partial \Phi}{\partial \boldsymbol{\sigma}} \quad (\text{Flow rule}) \quad (3.2c)$$

$$\dot{\boldsymbol{\alpha}} = -\dot{\lambda} H_{kin} \frac{\partial \Phi}{\partial \boldsymbol{\alpha}} \quad (\text{Kinematic hardening law}) \quad (3.2d)$$

$$\dot{q} = \frac{\partial q}{\partial e^{pl}} \dot{e}^{pl} \quad (\text{Isotropic hardening law}) \quad (3.2e)$$

$$\dot{e}^{pl} = \dot{\lambda} \quad (\text{Equivalent plastic strain}) \quad (3.2f)$$

$$\Phi(\boldsymbol{\sigma}, \boldsymbol{\alpha}, e^{pl}) = \sigma_{eq}(\boldsymbol{\sigma}, \boldsymbol{\alpha}) - q(e^{pl}) \leq 0 \quad (\text{Yield criterion}) \quad (3.2g)$$

In the above system of differential algebraic equations, λ is the plastic parameter, H_{kin} is the kinematic hardening modulus, \mathbb{C}^{el} is the elastic moduli, a fourth order tensor, of the material and σ_{eq} is the equivalent stress, which is determined by the yield criterion used. Furthermore, in the case of linear isotropic hardening with modulus H_{iso} , the corresponding harening law (Eq. 3.2e) becomes $\dot{q} = H_{iso} \dot{e}^{pl}$, where e^{pl} is the equivalent plastic strain. Finally, with the inequality in Eq. (3.2g) we define a feasible stress space. Stress points stictly satisfying the inequality, $\Phi < 0$ represent an elastic state while those that cause plastic flow render Φ zero.

The so-called Karush-Kuhn-Tucker loading/unloading conditions derived from the underly-

ing constrained variational problem[33] can be stated as follows:

$$\Phi \leq 0, \quad \dot{\lambda} \geq 0, \quad \dot{\lambda}\Phi = 0 \quad (3.3)$$

From these conditions we can determine the current stress state:

- if $\dot{\lambda} > 0$, then $\dot{\lambda}\Phi = 0$ implies $\Phi = 0$ which means the state is plastic
- if $\Phi < 0$, then $\dot{\lambda}\Phi = 0$ implies $\dot{\lambda} = 0$ and from (3.2c) we get that the state is elastic.

Since $\Phi = 0$, $\dot{\lambda} > 0$ when plastic loading persists, the third equation in (3.3) leads to the so-called plastic consistency condition:

$$\dot{\lambda}\dot{\Phi} = 0 \quad (3.4)$$

3.3 The J_2 formulation for fiber stress state

3.3.1 Mapping on the constrained stress space

We begin by defining the admissible stress space for a planar beam fiber, \mathcal{S} :

$$\mathcal{S} = \{\vec{\sigma} \in \mathbb{R}^6 \mid \sigma_{22} = \sigma_{33} = \sigma_{23} = \sigma_{13} = 0\}$$

The von Mises yield criterion is stated as follows:

$$\Phi(J_2, e^{pl}) = \sqrt{3J_2} - q(e^{pl}) \leq 0 \quad (3.5)$$

where J_2 is the second invariant of the deviatoric stress tensor:

$$J_2 = \frac{1}{2}\boldsymbol{\sigma}^d : \boldsymbol{\sigma}^d \quad (3.6)$$

The deviatoric part of any tensor is given by $()^d = () - \frac{1}{3}\mathbf{I} \cdot \text{trace}[()]$, with \mathbf{I} being the identity

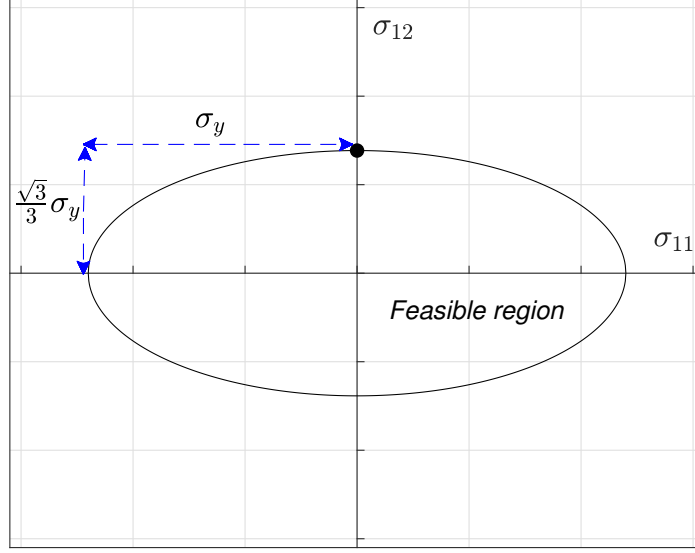


Fig. 3.1. Feasible space and yield locus for the J_2 model. At the boundary of the ellipse, $\sqrt{3J_2} = q$.

tensor and symbol $\mathfrak{z} : \zeta$ designates the contraction operator: $\boldsymbol{\sigma}^d : \boldsymbol{\sigma}^d = \sum_{i,j} \sigma_{ij}^d \sigma_{ij}^d$.

In the von Mises J_2 framework, the hydrostatic pressure cannot cause plastic flow. In other words, plastic deformation is due to the deviatoric components of the stress tensor and volume changes are caused only by elastic deformations. This implies that $\text{trace}[\boldsymbol{\epsilon}^{pl}] = 0$ which, coupled with Eq. (3.2d), also leads to $\text{trace}[\boldsymbol{\alpha}^{pl}] = 0$. This means that the back stress tensor in Eq. (3.2d) deviatoric.

In active stress space \mathcal{S} the yield function is $\Phi = \sqrt{\sigma_{11}^2 + 3\sigma_{12}^2} - q$ describes an ellipse, shown in 3.1, with semi-major and semi-minor axes σ_y , $\sqrt{3}/3\sigma_y$, respectively.

When kinematic hardening is included, we introduce the effective stress tensor and its deviatoric part in order to facilitate notational simplicity:

$$\boldsymbol{\zeta} = \boldsymbol{\sigma} - \boldsymbol{\alpha}, \quad \boldsymbol{\zeta}^d = \boldsymbol{\sigma}^d - \boldsymbol{\alpha}^d \quad (3.7)$$

We now define the following vectors associated with the active tensor components that ex-

pliely enter subsequent derivations:

$$\vec{\alpha}_f = \begin{bmatrix} \alpha_{11} \\ \alpha_{12} \end{bmatrix}, \quad \vec{\alpha}_f^d = \begin{bmatrix} \alpha_{11}^d \\ \alpha_{12}^d \end{bmatrix}, \quad \vec{\epsilon}_f^{pl} = \begin{bmatrix} \epsilon_{11}^{pl} \\ \gamma_{12}^{pl} \end{bmatrix},$$

$$\vec{\sigma}_f^d = \begin{bmatrix} \sigma_{11}^d \\ \sigma_{12}^d \end{bmatrix}, \quad \vec{\zeta}_f = \begin{bmatrix} \zeta_{11} \\ \zeta_{12} \end{bmatrix}, \quad \vec{\zeta}_f^d = \begin{bmatrix} \zeta_{11}^d \\ \zeta_{12}^d \end{bmatrix}$$

The vector representation of (3.6) in terms of the effective stress is:

$$J_2 = \frac{1}{2}(\vec{\zeta}^d)^T \mathbf{J} \vec{\zeta}^d \quad (3.8)$$

where matrix $\mathbf{J} = \text{diag}[1, 1, 1, 2, 2, 2]$ is introduced to account for the symmetry of ζ^d .

We now seek a mapping from the deviatoric stress space onto the fiber stress space S of the deviatoric effective stress vector $\vec{\zeta}^d$ that preserves the inner product and, thus, the second deviatoric invariant J_2 . The non-zero components of $\vec{\zeta}^d$ are $\zeta_{11}^d, \zeta_{22}^d, \zeta_{33}^d, \zeta_{12}^d, \zeta_{21}^d$ and thus we can establish the following mappings between the active components of $\vec{\zeta}^d$ and $\vec{\zeta}_f$:

$$\vec{\zeta}^d = \mathbf{Q} \vec{\zeta}_f, \quad \vec{\zeta}_f^d = \mathbf{S} \vec{\zeta}_f \quad (3.9)$$

where the mapping matrices above are given by:

$$\mathbf{Q} = \begin{bmatrix} \frac{2}{3} & -\frac{1}{3} & -\frac{1}{3} & 0 & 0 & 0 \\ 0 & 0 & 0 & 1 & 0 & 0 \end{bmatrix}^T, \quad \mathbf{S} = \begin{bmatrix} \frac{2}{3} & 0 \\ 0 & 1 \end{bmatrix} \quad (3.10)$$

We can now express J_2 purely in terms of $\vec{\zeta}_f$:

$$J_2 = \frac{1}{2}(\vec{\zeta}^d)^T \mathbf{J} \vec{\zeta}^d = \frac{1}{2} \vec{\zeta}_f^T \mathbf{Q}^T \mathbf{J} \mathbf{Q} \vec{\zeta}_f = \frac{1}{2} \vec{\zeta}_f^T \mathbf{V} \vec{\zeta}_f = \frac{1}{2} \|\vec{\zeta}_f\|_{\mathbf{V}}^2 \quad (3.11)$$

where $\mathbf{V} = \text{diag}[\frac{2}{3}, 2]$ and the notation used for the inner product induced by matrix \mathbf{A} between

vectors \vec{w} , \vec{v} is $(\vec{w}, \vec{v})_A = \vec{w}^T \mathbf{A} \vec{v}$, which leads to the notation adopted in Eq. (3.11).

With these derivations at hand, system (3.2) can be recast in the constrained fiber stress state as follows:

$$\dot{\vec{\epsilon}}_f = \dot{\vec{\epsilon}}_f^{el} + \dot{\vec{\epsilon}}_f^{pl} \quad (\text{Strain decomposition}) \quad (3.12a)$$

$$\dot{\vec{\sigma}}_f = \mathbf{C}^{el} \left[\dot{\vec{\epsilon}}_f - \dot{\vec{\epsilon}}_f^{pl} \right] \quad (\text{Elastic constitutive law}) \quad (3.12b)$$

$$\dot{\vec{\epsilon}}_f^{pl} = \dot{\lambda} \vec{n} \quad (\text{Flow rule}) \quad (3.12c)$$

$$\dot{\vec{\alpha}}_f = \dot{\lambda} H_{kin} \mathbf{V}^{-1} \vec{r} \quad (\text{Kinematic hardening law}) \quad (3.12d)$$

$$\dot{q}_f = \dot{\lambda} \frac{\partial q_f}{\partial e_f^{pl}} \quad (\text{Isotropic hardening law}) \quad (3.12e)$$

$$\Phi(\vec{\zeta}_f, e^{pl}) = \sqrt{\frac{3}{2}} \|\vec{\zeta}_f\|_{\mathbf{V}} - q_f(e_f^{pl}) \leq 0 \quad (\text{Yield criterion}) \quad (3.12f)$$

Vector \vec{n} is expressed as follows:

$$\vec{n} = \frac{\partial \Phi}{\partial \sigma_f} = -\frac{\partial \Phi}{\partial \alpha_f} = \sqrt{\frac{3}{2}} \frac{\mathbf{V} \vec{\zeta}_f}{\|\vec{\zeta}_f\|_{\mathbf{V}}} \quad (3.13)$$

Equations (3.2e), (3.2f) remain the same in the current system. In addition, note that for the J_2 model, the left-hand side of eq. (3.2d) is a deviatoric tensor whereas in (3.12d) it has been mapped to fiber stress space \mathcal{S} .

3.3.2 Continuous tangent modulus

The continuous elastoplastic modulus \mathbf{C}^{ep} is found by enforcing the plastic consistency condition (3.4) during a plastic step:

$$\vec{n}^T \dot{\vec{\zeta}}_f - \dot{\lambda} \frac{\partial q_f}{\partial e_f^{pl}} = 0 \quad (3.14)$$

The rate form for the effective stress is given by combining Eqs. (3.12b), (3.12d) with $\dot{\zeta}_f = \dot{\vec{\sigma}}_f - \dot{\vec{\alpha}}_f$:

$$\dot{\zeta}_f = \mathbf{C}^{el}\dot{\epsilon}_f - \dot{\lambda}\mathbf{Z}\vec{n} \quad (3.15)$$

where $\mathbf{Z} = \mathbf{C}^{el} + H_{kin}\mathbf{V}^{-1}$. Substituting (3.15) into (3.14) and solving for $\dot{\lambda}$ we get:

$$\dot{\lambda} = \frac{\vec{n}^T \mathbf{C}^{el} \dot{\vec{\epsilon}}_f}{\vec{n}^T \mathbf{Z} \vec{n} + \frac{\partial q_f}{\partial e_f^{pl}}} \quad (3.16)$$

Finally, by making use of (3.16), (3.12c) and (3.12b), we arrive at the expression for the continuous elastoplastic modulus:

$$\mathbf{C}^{pl} = \mathbf{C}^{el} - \frac{\vec{m}\vec{m}^T}{\vec{n}^T \mathbf{Z} \vec{n} + \frac{\partial q_f}{\partial e_f^{pl}}} \quad (3.17)$$

where $\vec{m} = \mathbf{C}^{el}\vec{n}$.

3.4 Implicit integration of rate equations

We employ the fully implicit backward Euler method to discretize the rate constitutive equations in system (3.12) in the pseudotime interval $[t_n, t_{n+1}]$. We regard the incremental/iterative process as strain driven, in that at the start of increment n , the dependent state variables for each fiber, $S_n = \{\vec{\epsilon}_f, \vec{\epsilon}_f^{pl}, \vec{\alpha}_f, e_f^{pl}\}_n$, are known and stored. We also know the increment in the centerline strain vector \vec{d} , $\Delta\vec{d}$. The incremental strain vector for the current fiber is then determined using eq. (2.53b):

$$\Delta\vec{\epsilon}_f = \mathbf{N}_s \Delta\vec{q}$$

Given the incremental strain vector $\Delta\vec{\epsilon}_f$, we need to update the state variables for t_{n+1} : $S_n \rightarrow S_{n+1}$. In what follows we omit the subscript denoting the vector pertains to the fiber state:

$$S_n \equiv \{\vec{\epsilon}_n, \vec{\epsilon}_n^{pl}, \vec{\alpha}_n, e_n^{pl}\}, \quad S_{n+1} \equiv \{\vec{\epsilon}_{n+1}, \vec{\epsilon}_{n+1}^{pl}, \vec{\alpha}_{n+1}, e_{n+1}^{pl}\},$$

The update of the fiber total strain vector $\vec{\epsilon}$ is trivial: $\vec{\epsilon}_{n+1} = \vec{\epsilon}_n + \Delta\vec{\epsilon}$. For the remaining

state variables the rate system (3.12) is discretized as follows:

$$\vec{\sigma}_{n+1} = \mathbf{C}^{el} [\vec{\epsilon}_{n+1} - \vec{\epsilon}_{n+1}^{pl}] \quad (3.18a)$$

$$\vec{\epsilon}_{n+1}^{pl} = \vec{\epsilon}_n^{pl} + \dot{\lambda} \vec{n}_{n+1} \quad (3.18b)$$

$$\vec{\alpha}_{n+1} = \vec{\alpha}_n + \lambda H_{kin} \mathbf{V}^{-1} \vec{n}_{n+1} \quad (3.18c)$$

$$q_{n+1} = q_n + \lambda \frac{\partial q_{n+1}}{\partial e_{n+1}^{pl}} \quad (3.18d)$$

$$\Phi(\vec{\zeta}_{n+1}, e_{n+1}^{pl}) = \sqrt{\frac{3}{2}} \|\vec{\zeta}_{n+1}\|_V - q_{n+1}(e_{n+1}^{pl}) \leq 0 \quad (3.18e)$$

and

$$\vec{\zeta}_{n+1} = \vec{\sigma}_{n+1} - \vec{\alpha}_{n+1} \quad (3.19)$$

3.4.1 Elastic predictor - Plastic Corrector algorithm

It is convenient to recast system (3.18) purely in terms of stress by utilizing (3.19),(3.18a),(3.18c):

Stress rate system	Discretized system
$\dot{\vec{\zeta}} = \mathbf{C}^{el} \dot{\vec{\epsilon}} - \dot{\lambda} \mathbf{Z} \vec{n}$ (3.20a)	$\vec{\zeta}_{n+1} = \vec{\zeta}_n + \mathbf{C}^{el} \Delta \vec{\epsilon}_{n+1} - \lambda \mathbf{Z} \vec{n}_{n+1}$ (3.21a)
$\dot{q} = \dot{\lambda} \frac{\partial q}{\partial e^{pl}}$ (3.20b)	$q_{n+1} = q_n + \lambda \frac{\partial q_{n+1}}{\partial e_{n+1}^{pl}}$ (3.21b)

We need not differentiate between initial and final value for the plastic parameter λ since it is initialized to zero at the beginning of every step: $\lambda_n = 0$. The solution of (3.21) is based on a two-step procedure. The first phase is called trial elastic step, where we assume that the increment $\Delta \vec{\epsilon}$ is elastic and all state variables are updated by setting $\lambda = 0$: $S_n \rightarrow S_{n+1}^{TR}$. If the trial stresses satisfy the yield condition $\Phi_{n+1}^{TR} < 0$, then the step was indeed elastic and we can set $S_{n+1}^{TR} \rightarrow S_{n+1}$. If the yield criterion is violated, $\Phi_{n+1}^{TR} > 0$, then the step is plastic and we need to apply (plastic) corrections to the state variables so that, upon convergence, we have achieved $\Phi_{n+1} = 0$. This procedure is referred to as Elastic Predictor - Plastic Corrector algorithm and can be traced back to the work of Wilkins[34]. It has enjoyed widespread application in solving

problems in elastoplasticity[35, 36, 37, 38, 39, 40] and the basic relations for each step are summarized below.

Elastic Predictor	Plastic Corrector
$\vec{\zeta}_{n+1}^{TR} = \mathbf{C}^{el} [\vec{\epsilon}_{n+1} - \vec{\epsilon}_n^{pl}] - \vec{\alpha}_n$	$\vec{\zeta}_{n+1} = \vec{\zeta}_{n+1}^{TR} - \lambda \mathbf{Z} \vec{n}_{n+1}$ (3.23a)
$q_{n+1}^{TR} = q_n$	$\xrightarrow{\Phi_{n+1}^{TR} > 0} q_{n+1} = q_{n+1}^{TR} + \lambda \frac{\partial q_{n+1}}{\partial \epsilon_{n+1}^{pl}}$ (3.23b)
$\Phi_{n+1}^{TR} = f(\vec{\zeta}_{n+1}^{TR}, q_{n+1}^{TR})$	$\Phi_{n+1} = 0$ (3.23c)

The Plastic Corrector step is a system of 4 nonlinear algebraic equations with 4 unknowns, $\{\zeta_{11,n+1}, \zeta_{12,n+1}, q_{n+1}, \lambda\}$, and generally a local Newton method is required to determined the unknowns. It should be stressed here that, in multiaxial constitutive algorithms that do not make use of the mapping as developed here, this local process is nested within an upper level Newton procedure that enforces the zero transverse stress condition.

Substituting Eqs. (3.23a),(3.23b) into (3.23c) furnishes a nonlinear scalar equation that needs to be solved for λ . Once λ is computed, then the fiber state can be updated $S_{n+1}^{TR} \rightarrow S_{n+1}$. Refer also to Box 1 for a detailed summary of the plastic updates. Detailed expressions for the local Newton method on $\Phi_{n+1}(\lambda) = 0$ are provided in Appendix C.

3.4.2 Consistent Tangent Modulus

The tangent modulus consistent with the numerical discretization used on system (3.12) is necessary to restore the quadratic rates of convergence for the global Newton method[41]. That is:

$$\mathbf{C}_c^{pl} = \frac{d\vec{\sigma}_{n+1}}{d\vec{\epsilon}_{n+1}} \quad (3.24)$$

We take the differentials of (3.18a), (3.18c) and (3.18e), using the fact that $d\vec{\zeta}_{n+1} = d\vec{\sigma}_{n+1} - d\vec{\alpha}_{n+1}$ from (3.19) and arrive at the following system:

$$\begin{bmatrix} \mathbf{C}^{el} + \lambda \Psi_{n+1} & -\lambda \Psi_{n+1} \\ -\lambda \Psi_{n+1} & H_{kin}^{-1} \mathbf{V} + \lambda \Psi_{n+1} \end{bmatrix} \begin{bmatrix} d\vec{\sigma}_{n+1} \\ d\vec{\alpha}_{n+1} \end{bmatrix} = \begin{bmatrix} d\vec{\epsilon}_{n+1} - d\lambda \vec{n}_{n+1} \\ d\lambda \vec{n}_{n+1} \end{bmatrix} \quad (3.25a)$$

$$\vec{n}_{n+1}^T [d\vec{\sigma}_{n+1} - d\vec{\alpha}_{n+1}] = d\lambda \frac{\partial q_{n+1}}{\partial e_{n+1}^{pl}} \quad (3.25b)$$

where Ψ is given as follows:

$$\Psi = \frac{\partial \vec{n}}{\partial \vec{\zeta}} = \frac{\partial^2 f}{\partial \vec{\zeta}^2} = \frac{1}{\|\vec{\zeta}\|_V} [\mathbf{V} - \vec{n} \vec{n}^T] \quad (3.26)$$

Upon solving (3.25a) for $d\vec{\sigma}_{n+1}$, $d\vec{\alpha}_{n+1}$ we substitute them into (3.25b) and solve for $d\lambda$:

$$d\lambda = \frac{\vec{n}_{n+1}^T [\Xi_{11} + \Xi_{12}^T] d\vec{\epsilon}_{n+1}}{\vec{n}_{n+1}^T \mathbf{T} \vec{n}_{n+1} + \frac{\partial q_{n+1}}{\partial e_{n+1}^{pl}}} \quad (3.27)$$

Finally, substituting $d\lambda$ into (3.18a) furnishes the formula for the consistent tangent modulus:

$$\mathbf{C}_c^{pl} = \Xi_{11} - \frac{\vec{N}_{n+1} \vec{N}_{n+1}^T}{1 + \delta_{n+1}} \quad (3.28)$$

Details regarding all newly defined vectors and matrices involved in the derivation of \mathbf{C}_c^{pl} is given in Appendix D. In Box 1 we have summarised the return mapping algorithm for a fiber.

3.4.3 Consistent Section Stiffness

Once the stress update on a particular fiber has been carried out, its contribution to the stress resultant vector and the section stiffness are accounted for via a midpoint integration rule along the section height (see Eqs. (2.56), (2.58)).

Box 1 : Summary of Elastic Predictor - Plastic Corrector algorithm.

- **Start of step - Elastic Predictor**

<ul style="list-style-type: none"> ■ $\vec{\epsilon}_{n+1}^{pl,TR} = \vec{\epsilon}_n^{pl}$ ■ $\vec{\sigma}_{n+1}^{TR} = \mathbf{C}^{el} [\vec{\epsilon}_{n+1} - \vec{\epsilon}_n^{pl}]$ ■ $\vec{\alpha}_{n+1}^{TR} = \vec{\alpha}_n$ 	<ul style="list-style-type: none"> ■ $e_{n+1}^{pl,TR} = e_n^{pl}$ ■ $q_{n+1}^{TR} = q_n$ ■ $f_{n+1}^{TR} = \Phi(\vec{\zeta}_{n+1}^{TR}, q_{n+1}^{TR})$
---	--

- IF $\Phi_{n+1}^{TR} < 0 \rightarrow \text{Elastic Step}$

<ul style="list-style-type: none"> ■ $\vec{\epsilon}_{n+1}^{pl} = \vec{\epsilon}_{n+1}^{pl,TR}$ ■ $\vec{\sigma}_{n+1} = \vec{\sigma}_{n+1}^{TR}$ ■ $\vec{\alpha}_{n+1} = \vec{\alpha}_{n+1}^{TR}$ 	<ul style="list-style-type: none"> ■ $e_{n+1}^{pl} = e_{n+1}^{pl,TR}$ ■ $q_{n+1} = q_{n+1}^{TR}$ ■ $\mathbf{C} = \mathbf{C}^{el}$
---	---

- ELSE $f_{n+1}^{TR} > 0 \rightarrow \text{Plastic Corrector}$

1. Iteratively solve (3.4.1) for λ : $\lambda^{j+1} = \lambda^j - \frac{\Phi_{n+1}^j}{(\frac{d\Phi_{n+1}}{d\lambda})^j}$, with $\lambda^0 = 0$, $\Phi_{n+1}^0 = \Phi_{n+1}^{TR}$. Loop termination: $|\Phi_{n+1}^{j+1}| \leq e_{tol}$, where e_{tol} small.

2. Update state variables:

<ul style="list-style-type: none"> ■ $\vec{\zeta}_{n+1} = \Omega(\lambda) \vec{\zeta}_{n+1}^{TR}$ ■ $\vec{\epsilon}_{n+1}^{pl} = \vec{\epsilon}_n^{pl} + \lambda \vec{n}_{n+1}$ ■ $\vec{\alpha}_{n+1} = \vec{\alpha}_n + \lambda H_{kin} \mathbf{V}^{-1} \vec{n}_{n+1}$ 	<ul style="list-style-type: none"> ■ $\vec{\sigma}_{n+1} = \vec{\zeta}_{n+1} + \vec{\alpha}_{n+1}$ ■ $e_{n+1}^{pl} = e_n^{pl} + \lambda$ ■ $q_{n+1} = q_n + \lambda \frac{\partial q_{n+1}}{\partial e_{n+1}^{pl}}$
---	---

3. Get consistent tangent modulus

$$\mathbf{C} = \mathbf{C}_c^{pl} = \Xi_{11} - \frac{\vec{N}_{n+1} \vec{N}_{n+1}^T}{1 + \delta_{n+1}}$$

See Appendix C for $\Omega(\lambda)$.

Notice that while in the present formulation $C_{21} = C_{12}$, this will not be the case if a generalized integration rule is used for the rate equations. In such a scenario, if enforcement of the plastic consistency does not correspond to the interior time $t_a \in [t_n, t_{n+1}]$ chosen, that is $\Phi_a = 0$, then the consistent tangent will not be symmetric. For more details on this refer to [42].

3.5 Numerical Examples

3.5.1 Accuracy of the proposed algorithm

Iso-error maps are commonly used to test the accuracy of return-mapping algorithms in elasto-plasticity[43]. The contours are generated by imposing a family of stress or strain prescribed loadings from a selected point on the yield surface which cause further plastification (no unloading). For each load incrementation, the error is computed as the relative difference between the stress predicted by the proposed algorithm and “exact” stress. The exact stress is typically found by imposing the same increment in a number of sequential subincrements, n_s . A convergence analysis is required to ensure that subincrementation indeed converges to a stress point. In the present study it was found that for $n_s \geq 500$ the stress components had achieved convergence with respect to the first 7 decimal points. Therefore, we use $n_s = 500$. The error plotted is given by:

$$err = \frac{\|\vec{\sigma}^* - \vec{\sigma}\|}{\|\vec{\sigma}^*\|} \cdot 100 \quad (3.29)$$

where $\vec{\sigma}^*$ is the exact stress vector and $\vec{\sigma}$ the one predicted by the proposed scheme by solving in one step. The three points on the yield surface that are selected and shown in Fig. 3.2 correspond to an initial state of pure shear (A), mixed state where $\sigma_{11,0} = \sigma_{12,0}$ (B) and a pure uniaxial stress state (C). For each of these initial states the family of strain increments are imposed along the directions shown, with range up to $\Delta\|\vec{\epsilon}\| = 5\epsilon_y$, where ϵ_y is the yield strain in tension/compression. The material data used are: $E = 2.1 \times 10^5$, $\sigma_y = 2.4 \times 10^2$ and Poisson’s ratio $\nu = 0.3$. For the hardening cases, linear isotropic and kinematic moduli were prescribed as follows: $H_{iso} = H_{kin} = 10^4$.

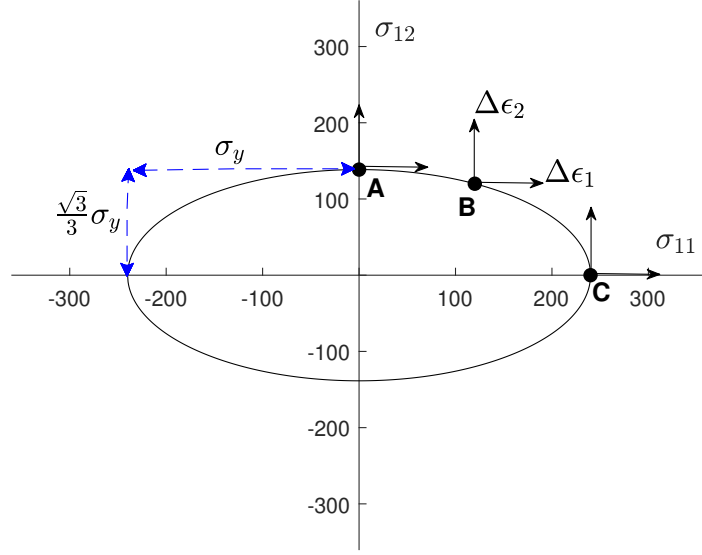


Fig. 3.2. Points of interest on yield surface and direction of load increments.

The parameters associated with the horizontal and vertical axes, a_1 , a_2 , are defined in the following way: $a_1 = \Delta\vec{\epsilon}_1/\epsilon_y$, $a_2 = \Delta\vec{\epsilon}_2/\epsilon_y$. As can be seen from figures 3.3, 3.4, the relative error remains small even for quite large increments in the strain vector. Note also that for along the semi-major and semi-minor axes in the cases of pure uniaxial state and pure shear respectively, the return mapping gives the exact stress even without subincrementation. The same is true for point B when the strain increments are along a direction around 68° with respect to a_1 axis.

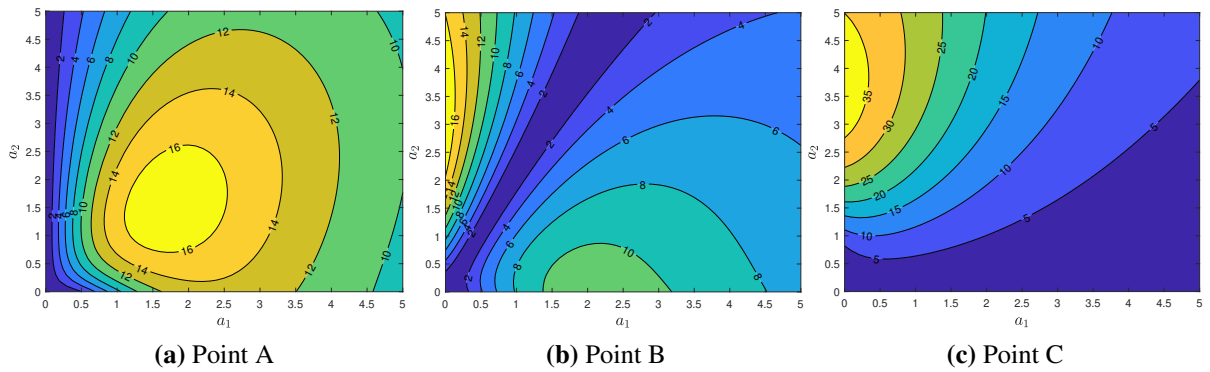


Fig. 3.3. Iso-error maps for a perfectly plastic material.

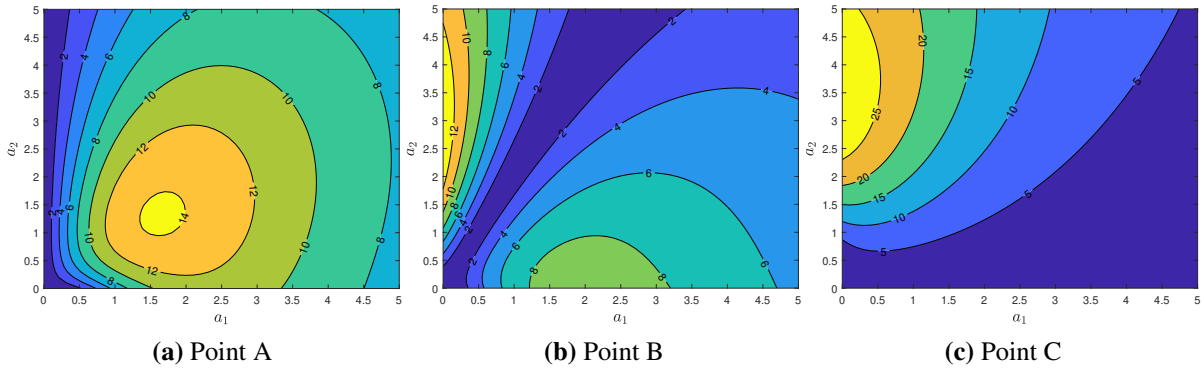


Fig. 3.4. Iso-error maps for combined linear isotropic and kinematic hardening.

3.5.2 Performance against non-monotonic strain histories

In this benchmark we investigate the performance of the proposed algorithm against the three dimensional/axisymmetric procedure typically implemented in beam elements when shear-flexure interaction is taken into account using a multiaxial law at the fiber level. We also compare it with the plane stress projection algorithm by Simo[41], which we followed in our derivations. In the former approach, the return mapping using an implicit integration results in the so-called radial return, which doesn't require iterations in the case of J_2 with perfect plasticity or linear hardening[34]. In contrast, the latter requires iterations since the topology of the stress space is not as simple as the von Mises cylinder anymore. We show below the drastic performance boost when using the present algorithm. As already state earlier, this is mainly due to the fact that we avoid an additional Newton procedure to enforce the zero transverse stress condition. The results for each scenario are shown in the tables below. A perfectly plastic material was assumed and both the average execution time $t(\text{sec})$ and the total number of iterations, N_i are considered as performance metrics. The *additional* iterations during purely elastic steps are also included in parentheses for the 3D and Simo's plane stress algorithm. Moreover, for each scenario, four different incrementations of the strain history are employed, shown in Fig. 3.5, and the effect of this scaling on the performance is highlighted. Parameter a determines the increment "length": $\alpha = \|\Delta\vec{\epsilon}\|/\epsilon_y$. Material data are the same as in the previous example.

As can be seen from the Tables 3.1-3.4, the proposed scheme offers significant speed-up

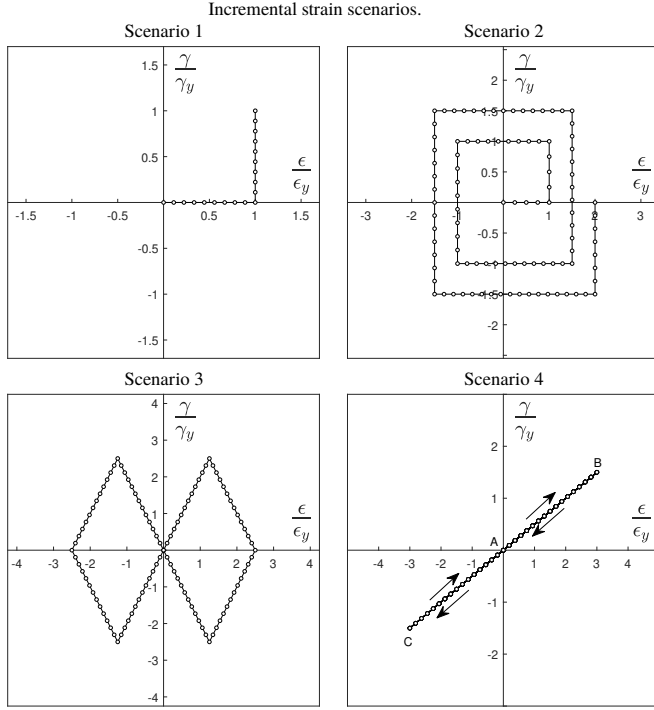


Fig. 3.5. The four different strain histories imposed, with the unstresses configuration as initial point.

compared to the other two methods. It should be highlighted that the 3D algorithm outperforms the one proposed by Simo because a perfectly plastic J_2 was used. In general, it too would require internal iterations to determine λ , in addition to the outer level Newton procedure to enforce the stress constraints. For Scenario 4, shown in Table 3.4, both the 3D and plane stress algorithms did [440, 188, 84, 62] elastic iterations corresponding to values of parameter α : [0.10, 0.25, 0.40, 0.50].

3.5.3 Plastic collapse of a doubly clamped beam

In this example we investigate the collapse load of a doubly clamped beam, shown in fig. 3.6, for two slenderness ratios, L/h : 20 and 4, where h is the cross-section height. We conduct analysis using both uncoupled and coupled, multiaxial, constitutive models at the fiber level and compare result, for each case, with the lower bound collapse load as predicted by limit analysis.

In addition, we showcase the influence of numerical quadrature in predicting the analytical

Table 3.1 Results for Scenario 1, perfect plasticity.

Algorithm	Exact $(\sigma_{11}, \sigma_{12})$	$\alpha = 0.10$		$\alpha = 0.25$		$\alpha = 0.40$		$\alpha = 0.50$	
		t^a	N_i	t	N_i	t	N_i	t	N_i
Proposed	(1.617, 1.023)	0.57	29	0.44	13	0.40	8	0.38	5
3D		1.40	46(20)	0.83	20(8)	0.65	11(4)	0.56	6(2)
Simo		1.64	165(19)	1.13	88(7)	0.96	64(3)	0.83	55(1)
Error(%) ^b			1.32		3.00		5.16		8.05

^a Measured in $\times 10^{-3}$ sec.^b Relative error in converged stress per increment scenario.**Table 3.2** Results for Scenario 2, perfect plasticity.

Algorithm	Exact $(\sigma_{11}, \sigma_{12})$	$\alpha = 0.10$		$\alpha = 0.25$		$\alpha = 0.40$		$\alpha = 0.50$	
		t^a	N_i	t	N_i	t	N_i	t	N_i
Proposed	(1.173, 1.208)	0.33	524	0.16	234	0.10	144	0.08	108
3D		1.24	849(97)	0.61	394(40)	0.31	196(17)	0.23	143(11)
Simo		2.09	2791(96)	1.17	1363(39)	0.57	790(15)	0.42	596(10)
Error(%)			2.32		5.00		10.10		13.35

^a Numbers in execution time columns are measured in $\times 10^{-2}$ s.**Table 3.3** Results for Scenario 3, perfect plasticity.

Algorithm	Exact $(\sigma_{11}, \sigma_{12})$	$\alpha = 0.10$		$\alpha = 0.25$		$\alpha = 0.40$		$\alpha = 0.50$	
		t^a	N_i	t	N_i	t	N_i	t	N_i
Proposed	(1.628, 1.018)	0.35	546	0.16	237	0.11	147	0.09	126
3D		1.15	920(115)	0.61	405(50)	0.31	194(22)	0.29	167(16)
Simo		2.20	2711(114)	1.42	1307(50)	0.55	789(20)	0.48	685(14)
Error(%)			1.15		2.51		5.40		5.80

^a Numbers in execution time columns are measured in $\times 10^{-2}$ s.**Table 3.4** Results for Scenario 4, five cycles, perfect plasticity. One cycle: A-B-C-A.

Algorithm	Exact $(\sigma_{11}, \sigma_{12})$	$\alpha = 0.10$		$\alpha = 0.25$		$\alpha = 0.40$		$\alpha = 0.50$	
		t^a	N_i	t	N_i	t	N_i	t	N_i
Proposed	(2.196, 0.559)	0.92	1500	0.44	678	0.22	392	0.19	345
3D		3.50	2500	1.61	1130	0.77	490	0.69	445
Simo		5.20	7497	2.93	4519	1.60	2352	1.38	2122
Error(%)			0.19		0.40		0.84		0.91

^a Numbers in execution time columns are measured in $\times 10^{-2}$ s.

solution in the slender case. More specifically, we compare Gauss-Legendre and Gauss-Lobatto quadratures. The quadrature rule used is crucial for both flexibility-based beam elements and the hybrid one presented and used herein, since, in both formulations, accuracy relies more on the precision of integration rather than mesh density. Lastly, each cross-section is discretized into 15 layers.

The shear strain distribution function, $k_q\varphi(X_2)$, is assumed to be parabolic and defined as follows:

$$\varphi(X_2) = (1 - 4 \frac{X_2^2}{h^2}) \quad (3.30)$$

where k_q is a parameter introduced in order to establish shear strain energy equivalence between assumed and exact distributions. For that matter, it is convenient to consider the uniform shear strain-average force hypothesis coupled with the corresponding shear coefficient as a representation of the exact one, assuming elastic behavior:

$$\mathcal{U}_{shear}^{exact} = k_s \mathcal{U}_{shear}^{unif} = \mathcal{U}_{shear}^{quad} \iff \frac{1}{2} k_s G A \gamma^2 = \frac{1}{2} G k_q^2 \left(\int_A \varphi(X_2)^2 dA \right) \gamma^2 \quad (3.31)$$

where k_s is the shear coefficient for uniform shear strain assumption. For rectangular sections with $\nu = 0.3$, $k_s = 0.886$ and solving eq. 3.31 for k_q we get:

$$k_q = \sqrt{\frac{k_s A}{\int_A \varphi(X_2)^2 dA}} \quad (3.32)$$

A first observation from fig 3.7 is that Gauss-Legendre quadrature tends to overestimate the capacity load in both edges of the slenderness spectrum and . Gauss-Lobatto quadrature, in contrast, is more accurate and converges to the “exact” capacity from “below”. In addition, it provides accuracy with just 5 quadrature points whereas even with 9 points, Gauss-Legendre still is not as accurate and converges from “above”. The results are in agreement with the ones reported by Papachristidis et al.[28] in a similar investigation but using a flexibility element.

When it comes to the influence of slenderness in the plastic capacity, the collapse load for

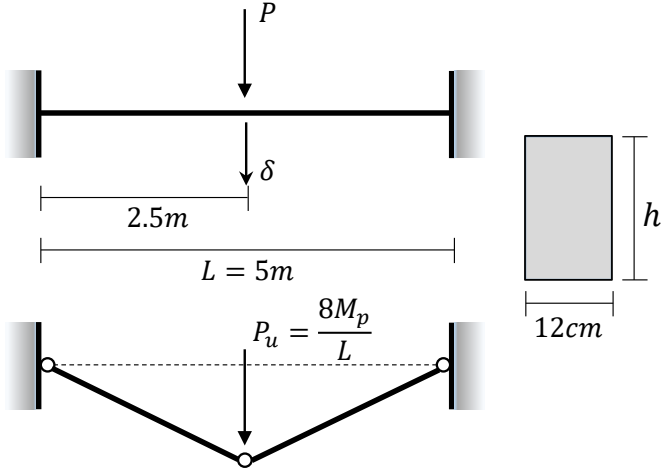


Fig. 3.6. Geometry, initial and final configuration of clamped beam, along with cross-section dimensions.

the L/h case predicted by the multiaxial constitutive law is lower than the one based on limit analysis. Interestingly, the uncoupled constitutive law results in a purely flexural collapse mode, thus yielding a ultimate load coinciding with the theoretical from limit analysis. When the beam is slender, both coupled and uncoupled constitutive laws result, expectably, in a flexure-dominant mode. The results are summarized in Table 3.5 and Fig. 3.7. In Fig. 3.8 the stress distributions for σ_{11} , σ_{12} and the von Mises stress, $\sigma_{VM} = \sqrt{3J_2}$ are presented at three different load levels indicate by point A, B and C (see Fig. 3.7b). The plastic zone propagation is also shown. We observe that the lower capacity as captured by the multiaxial model in the $L/h = 4$ case, which Fig. 3.8 pertains to, is due to shear plastification of the -shrinking- elastic core.

Table 3.5 Collapse moments and loads for clamped beam.

Collapse load, $P_u(kN)^a$					
L/h	$M_p(kN \cdot m)$	Limit Analysis	Uncoupled	Coupled	
20	$3.75 \cdot 10^2$	$6.00 \cdot 10^2$	$\approx 6.00 \cdot 10^2$	$\approx 6.00 \cdot 10^2$	
4	$9.37 \cdot 10^3$	$1.50 \cdot 10^4$	$\approx 1.50 \cdot 10^4$	$\approx 1.43 \cdot 10^4$	

Material data: $E = 200 \text{ GPa}$, $\sigma_y = 200 \text{ MPa}$.

^a For coupled and uncoupled loads, 5 Gauss-Lobatto points are assumed.

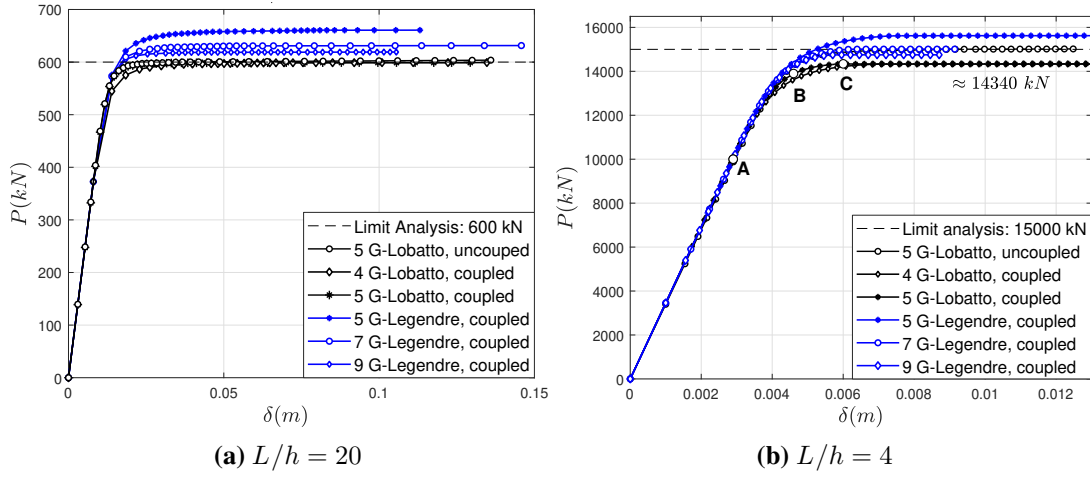


Fig. 3.7. Load-deflection plots for different slenderness ratios. Influence of quadrature type and number of points.

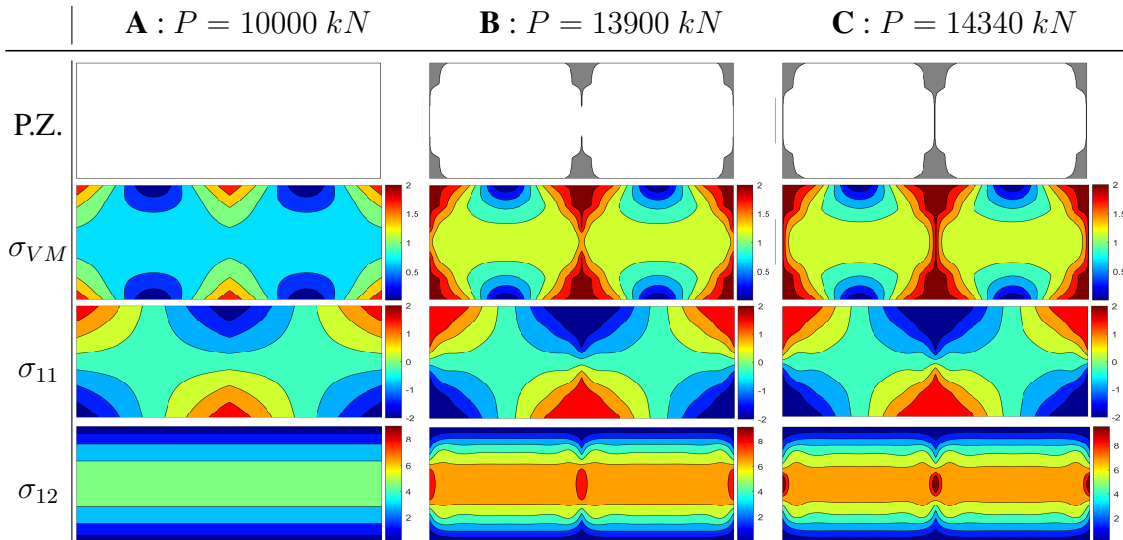


Fig. 3.8. Case $L/h = 4$. Spread of Plastic Zone (P.Z.) and stress distribution for von Mises, axial and shear stress at three different load levels.

3.5.4 Cyclic loading of shear link

In this example we are examining the response of a metallic shear link (Fig.3.9a) with a symmetric wide flange cross-section under displacement-controlled cyclic loading. The specimen we are concerned with was part of an experimental investigation by Hjelmstad & Popov[44] and later was numerically analyzed by Saritas & Filippou[29] using a mixed beam element formulation with shear-flexure interaction at the fiber level. In our analysys the specimen was modelled using one hybrid element with 5 Gauss-Lobatto points and 31 layers at each section with five layers on each flange.

The specimen length is $L = 28$ in. and the cross-section type is W 18 × 40 with basic dimensions specified as follows: total height $h = 17.88$ in., flange width $b = 5.985$ in., web and flange thickness, $t_w = 0.314$ in. and $t_F = 0.521$ in. respectively. The material properties are summarized in Table 3.6, while the displacement history, in accordance with Hjelmstad & Popov's experiment, is shown in Fig.3.9b The plastic modulus corresponding to linear kinematic hardening was determined from uniaxial data to be $H_{kin} = 102$ kips/in². A nonlinear hardening law was specified for the isotropic part, which is given as follows:

$$q(e^{pl}) = \sigma_y + C(1 - \exp(-\rho e^{pl})) \quad (3.33)$$

where $C = \sigma_u - \sigma_y$, σ_u , σ_y the ultimate and yield stresses respectively and ϵ_u , ϵ_y the corresponding strains. Parameter ρ is specified as $\rho = 20$ in this analysis. The shear strain distribution is again assumed to be quadratic, where $k_s = 0.466$ and, using eq. (3.32), $k_q = 1.33$.

As can be seen from Fig.3.10, during the first cycle we have satisfactory agreement between

Table 3.6 Material properties for Example 3.5.4.

Section	σ_y (kips/in ²)	σ_u (kips/in ²)	ϵ_y (%)	ϵ_u (%)	E (kips/in ²)	H_{kin} (kips/in ²)
W 18 × 40						
Web	39.5	60.1	1.8	22	28,300	102
Flange	35.0	58.5	1.4	24	28,000	102

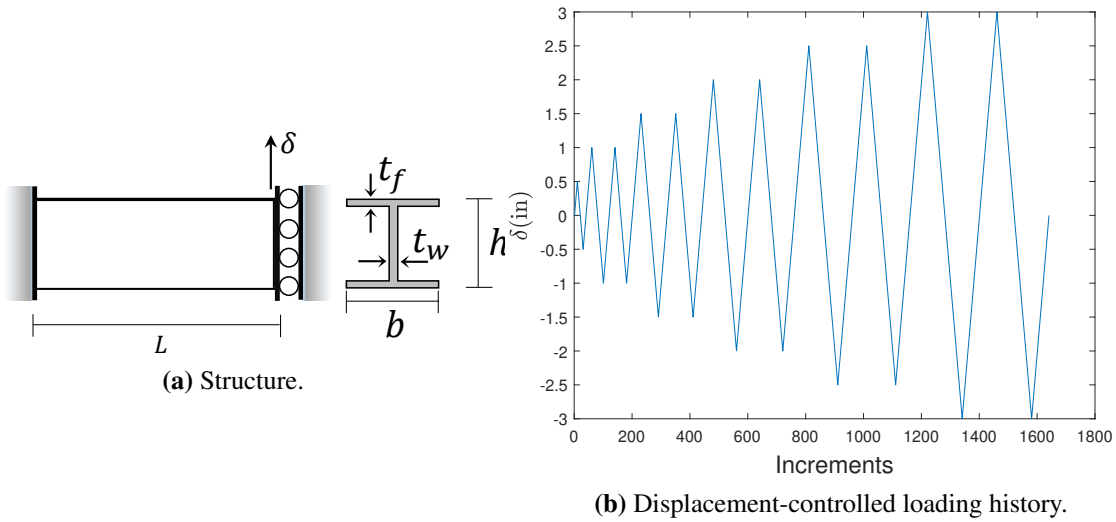


Fig. 3.9. Geometry of the specimen and displacement-controlled loading history.

the present analysis and the experimental result, while for all cycles after the third, we have almost excellent match between all cyclic histories shown. For the second and third cycles, with peak displacement at 1 inch, the present analysis exhibits a more abrupt yielding. This happens because most of the core becomes plastified within a smaller range of increments. While the hardening rules adopted might affect this behavior, it is the assumed shear strain distribution that plays a central role in transitioning from the elastic to plastic regime. Formulations that also consider shear stress distribution functions along the cross-section, section warping or even more accurate shear strain distribution models can definitely improve the approximation. We can also observe that both numerical models show identical accuracy during the unloading steps and a noticeable discrepancy with the experimental analysis. As explained in [29], this is due to improper restraint of the specimen during the experiment.

3.5.5 Elastoplastic post-buckling behavior of two-beam structure

This problem has been previously analyzed in [45, 46]. The structure, shown in Fig.3.11a, enters its inelastic regime immediately after the buckling load is reached, whereby point B starts moving inwards. In Fig.3.11b we compare the results we get using just 3 hybrid elements and 5 Gauss-Lobatto points in each element with Argyris et al.[45]. In addition, we include the inelastic

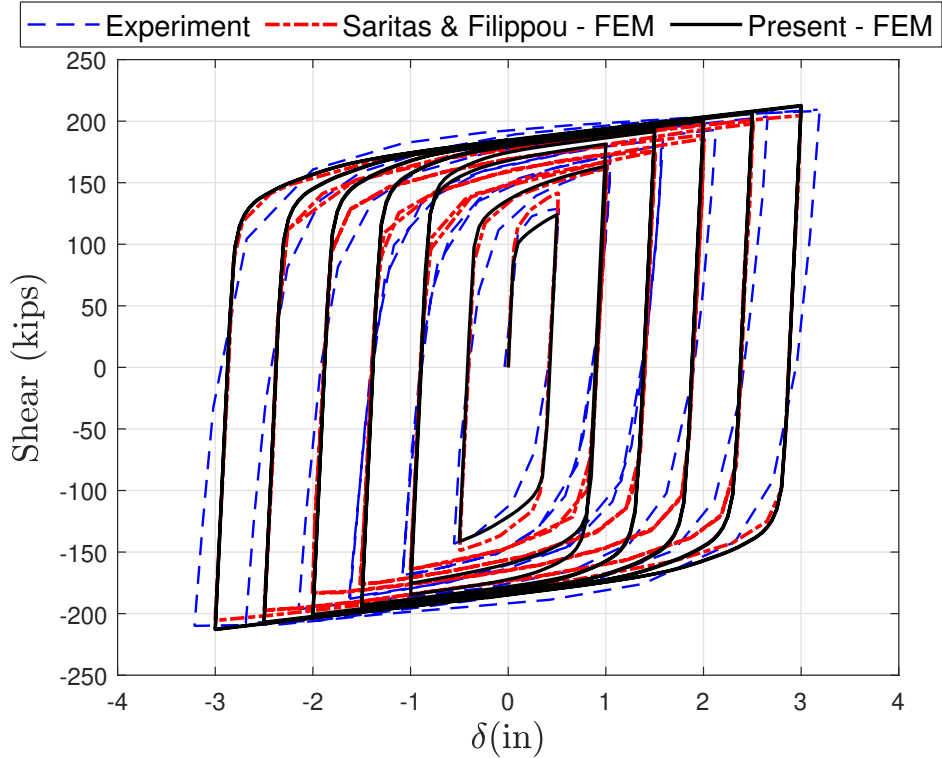
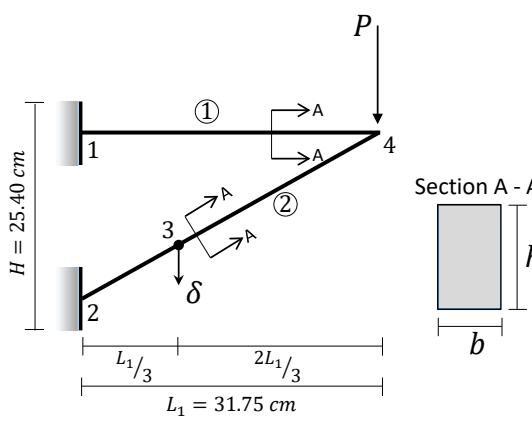


Fig. 3.10. Experimental and numerical results for the specimen.

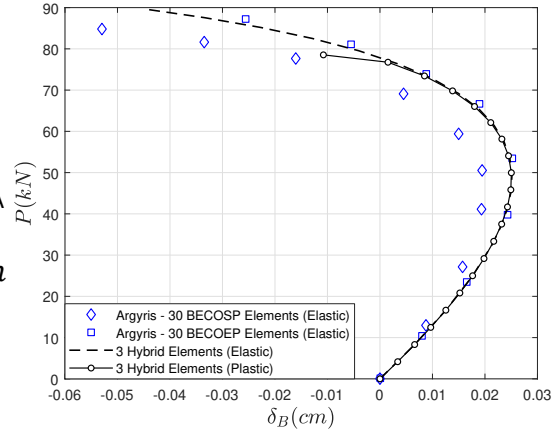
Table 3.7 Member geometric and material data.

Member	$E(\frac{\text{kN}}{\text{cm}^2})$	$H_{kin}(\frac{\text{kN}}{\text{cm}^2})$	$\sigma_y(\frac{\text{kN}}{\text{cm}^2})$	$h_s(\text{cm})$	$h_t(\text{cm})$	$b(\text{cm})$
(1)	6.86×10^3	2.84×10^2	26.20	1.91	8.00	2.54
(2)	6.86×10^3	2.84×10^2	33.10	1.91	8.00	2.54

analysis, which demonstrates that plastification starts immediately after then instability. The material and geometric data are shown in Table 3.7. Again, we highlight the impact of a coupled multiaxial law by investigating a variation of this problem. For all cases, inelastic response with kinematic hardening is assumed. The convergence rates in residual norm and energy norms for the case of thick members is also shown in Tables 3.8, 3.9. As can be seen from Fig.3.12b for the inelastic analysis of the thick member variation, the equilibrium paths corresponding to a coupled and uncoupled constitutive law tend to diverge shortly after the start of plastic deformation.



(a) Structure.



(b) Load vs deflection at point B.

Fig. 3.11. Geometry and loading of two-beam structure. Comparison of load vs deflection curves for different cases.

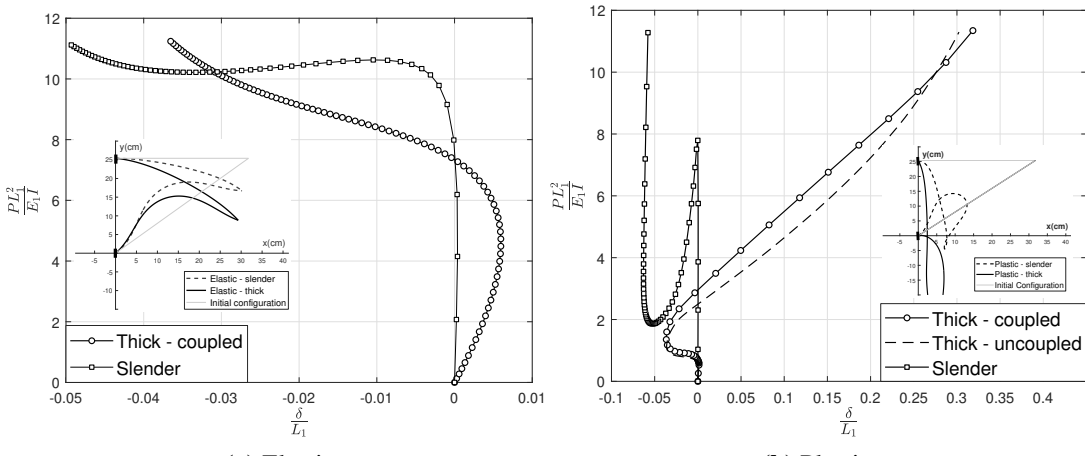


Fig. 3.12. Influence of slenderness and constitutive model on the response for elastic and elasto-plastic behavior.

Table 3.8 Convergence in residual norm during steps 5, 15, 25 35. $\epsilon_{tol} = 10^{-10}$.

iters.	5	15	25	35
1	$1.000000 \cdot 10^0$	$1.000000 \cdot 10^0$	$1.000000 \cdot 10^0$	$1.000000 \cdot 10^0$
2	$1.251499 \cdot 10^{-2}$	$1.988783 \cdot 10^{-2}$	$1.737845 \cdot 10^{-3}$	$6.187773 \cdot 10^{-2}$
3	$2.132711 \cdot 10^{-5}$	$1.066255 \cdot 10^{-5}$	$1.824164 \cdot 10^{-6}$	$4.214041 \cdot 10^{-3}$
4	$9.483080 \cdot 10^{-10}$	$4.882520 \cdot 10^{-10}$	$2.229120 \cdot 10^{-11}$	$6.111545 \cdot 10^{-5}$
5	$5.150000 \cdot 10^{-14}$	$7.790000 \cdot 10^{-13}$	$4.800000 \cdot 10^{-14}$	$1.218231 \cdot 10^{-8}$
6				$7.110000 \cdot 10^{-14}$

Table 3.9 Convergence in energy norm during steps 5, 15, 25, 35. $\epsilon_{tol} = 10^{-10}$.

iters.	5	15	25	35
1	$1.000000 \cdot 10^0$	$1.000000 \cdot 10^0$	$1.000000 \cdot 10^0$	$1.000000 \cdot 10^0$
2	$3.050574 \cdot 10^{-4}$	$1.065944 \cdot 10^{-4}$	$2.618542 \cdot 10^{-2}$	$1.188951 \cdot 10^{-2}$
3	$2.235712 \cdot 10^{-5}$	$5.373434 \cdot 10^{-5}$	$4.974768 \cdot 10^{-5}$	$1.495507 \cdot 10^{-4}$
4	$1.532842 \cdot 10^{-8}$	$2.585263 \cdot 10^{-9}$	$1.551550 \cdot 10^{-7}$	$1.706384 \cdot 10^{-5}$
5	$6.283000 \cdot 10^{-12}$	$1.962000 \cdot 10^{-12}$	$1.687900 \cdot 10^{-11}$	$3.948037 \cdot 10^{-7}$
7				$5.157400 \cdot 10^{-11}$

The full post-buckling elastoplastic equilibrium curve for the slender model is also provided for comparison. In Fig.3.12a the post-buckling response of both slender and thick models are illustrated. In the former, both uniaxial and multiaxial constitutive models yield identical results, assuming an infinite yield stress.

As we reduce the slenderness, slight differences arise compared to a purely uniaxial behavior at the fiber. This is mainly due to the assumed strain distribution, which is user defined and not accounted in the purely flexural model.

3.5.6 Three story frame with shear links

The three-story four-bay steel frame, first analyzed in [47], is shown in Fig. 3.13a, where the diagonal braces are ignored. Gravity loads are derived from the material and geometric properties of the elements and, for simplicity, are assumed to be acting on frame joints only. The values for each joint gravity load are shown in Table 3.10.

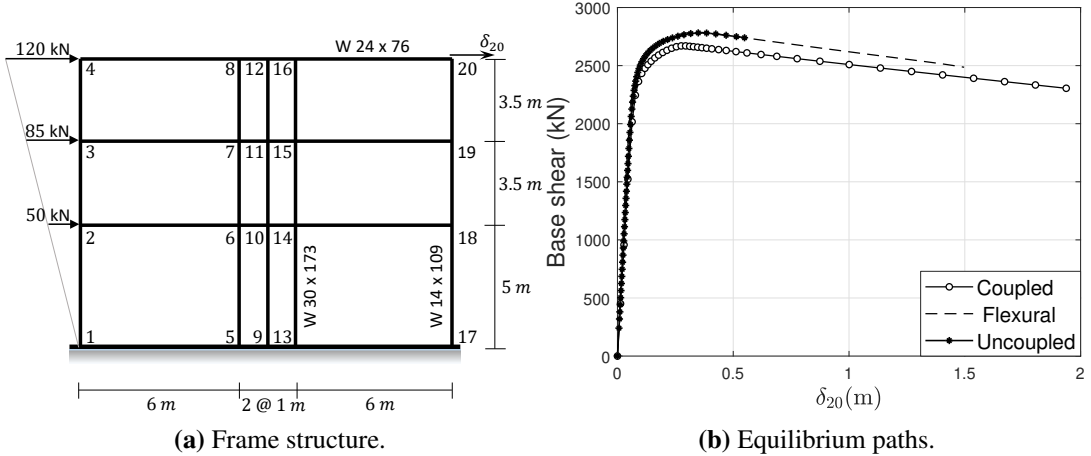


Fig. 3.13. Geometry of the steel frame and 3.13b response curves for three different models.

Table 3.10 Vertical gravity loads at nodes.

Nodes	2,18	3,19	4,20	6,14	7,15	8,16	10	11	12
$\downarrow P_i$ (kN)	240	220	145	340	300	190	255	215	120

A static pushover analysis is then conducted by with respect to the superimposed horizontal loads on nodes 2,3, and 4. For the discretization we used one hybrid element per member, 27 elements in total, and five Gauss-Lobatto quadrature points per element. All members have the same yield stress and Young's modulus: $\sigma_y = 290$ MPa, $E = 210$ GPa, and the Poisson's ratio is set to $\nu = 0.3$. Perfect plasticity is assumed and both material and geometric nonlinearity options are activated for the analysis. In Fig. 3.13b we show the results we get for 3 different modelling options regarding the constitutive law at the fiber level. Both the purely flexural model and the uncoupled elastoplastic model, whereby shear and axial states on fibers are uniaxial and do not interact, yield the same response curve and collapse load. In contrast, the coupled multiaxial model predicts, again, a lower plastic capacity load.

CHAPTER 4

NATURALLY PARAMETERIZED NLP FRAMEWORK

4.1 Introduction

This chapter presents a parametric nonlinear programming (PNLP) framework that extends the problem solving capabilities of the Hybrid NLP beam element beyond analyses concerned with mechanical loading. Such cases can be contact problems or structural sensitivity analysis. A strong feature of this framework lies in the utilization of homotopy continuation principles in order to establish conditions of global convergence to at least one solution. With the term “solution” we broadly refer to any critical point for the objective function, which in the present context is the TPE, with respect to the system variables.

Homotopy continuation, which forms the backbone of the PNLP framework, has been the subject of extensive studies in the field of applied mathematics[48, 49, 50, 51, 52, 53, 54, 55, 56, 57, 58, 59] as a technique for “globalizing” root finding algorithms. That is, even if the initial guess is not in the neighborhood of a root, homotopy theory guarantees convergence to at least one root, given certain regularity conditions hold. These conditions in essence establish the existence of a smooth path connecting the initial guess and that root. When applied to finding a root of a system of equations $F(x) = 0$, this can be done by introducing an “easy” problem whose a solution is easy to find, say $x - x_0 =$, and then construct a homotopy function $H(x, t) = tF(x) + (1 - t)(x - x_0)$, which represents a system of n equations with $n + 1$ unknowns. The system $H(x, t) = 0$ is sequentially solved for a discretization of $t \in [0, 1]$, starting at $t_0 = 0$, where the solution is known (“initial guess”). When $t = 1$ we have arrived at a root of the initial problem $F(x) = 0$. The process of varying t from 0 to 1 and solving the homotopy function is called deformation (not to be confused with mechanical deformation) and construction of such a homotopy function is called artificial homotopy. It is clear that the same principles can

be applied if system $F(x) = 0$ is undetermined, with n equations, $n + 1$ unknowns and a solution is available or can be found easily. In a nonlinear optimization context, application of the same principles have led to the formulation of global optimization algorithms[60, 61, 62, 63, 64, 65, 66, 67]. In addition, this framework highlights the firm theoretical underpinnings of various incremental methods that have been developed independently over the past decades for the numerical treatment of engineering problems[13, 68, 69, 70, 71, 72, 73, 74, 75, 76, 77, 78, 79, 80, 81, 82]. Application of this framework for approximating roots of systems of equations is commonly referred to as numerical continuation, whereas in the the context of finding optimizers it is termed parametric optimization or PNLP.

In structural mechanics, differential equilibrium equations can be reformulated as an optimization problem due to the existence of a variational structure, as discussed in Chapter 2. Thus, the PNLP framework provides a suitable and versatile engine for generating global solutions to engineering problems using the Hybrid NLP-based element, since it allows for the incorporation of constraint specifications directly at the minimization statement. It is shown that, in the presence of inequality constraints, the global path that connects the initial guess to a critical point is continuous but piecewise differentiable[60, 62, 61]. Finally, utilizing the underlying homotopy arguments, we establish the conditions under which the path we follow is unique and convergent to at least one critical point. Non-uniqueness of the homotopy path implies the existence of bifurcation points. Because the derivations do not make use of artificial functions in order to introduce initial guesses, we termed the formulation as Naturally Parameterized NLP (NPNLP). While this has the downside of requiring a known solution of the system in order to initiate the homotopy deformation process, in structural mechanics such states can often be found easily (e.g. initial configuration).

This chapter is divided into 5 sections. In the first section we give an overview of homotopy continuation as applied in (globally) solving systems of nonlinear equations and in parametric optimization. In the second section formulate the NPNLP framework for the Hybrid element and in section three we outline the conditions that both the TPE and the element constraints

need to satisfy in order to guarantee global convergence following a unique path. A brief note on bifurcating paths is also included but the topic is not explored further herein. Finally, we demonstrate the capabilities of the framework through a set of problems from the mechanics and applied mathematics literature.

4.2 Homotopy Continuation

4.2.1 Main idea

The application of numerical approximation methods in virtually all engineering and scientific problems leads, generally, to an algebraic system of equations, \vec{F} , to be solved for the system unknowns, \vec{x} . This system, of which we seek one or more roots, is expressed in the following form:

$$\vec{F}(\vec{x}) = \vec{0} \quad (4.1)$$

where for simplicity we assume that $\vec{x} \in \mathbb{R}^n$ and $\vec{F} : \mathbb{R}^n \rightarrow \mathbb{R}^n$ is a sufficiently smooth vector function. In the derivations that follow, boldface symbols denote vectors while bracketed bold-face symbols denote matrices. Given an initial estimate, \vec{x}_0 , one can use the Newton method to iteratively find a root:

$$\vec{x}_{i+1} = \vec{x}_i - \mathbf{F}_{\mathbf{x}, i}^{-1} \vec{F}_i, \quad i = 0, 1, \dots \quad (4.2)$$

This approach will yield a solution if i) \vec{x}_0 is already in the vicinity of a root and ii) if the Jacobian $\mathbf{F}_{\mathbf{x}}$ is not singular for any of the iterates $\{\vec{x}\}_i$. The main idea of the homotopy continuation is to overcome the difficulty that singularity points pose by imbedding problem (4.1) in a higher dimensional space where both \vec{x} and parameter t are considered independent variables. This is done by pairing function \vec{F} with a simpler problem, $\vec{G} : \mathbb{R}^n \rightarrow \mathbb{R}^n$ which has a trivial solution $\vec{G}(\vec{x}_0) = \vec{0}$, using a homotopy function, $\vec{H}(\vec{x}, t)$. For $\vec{H} : \mathbb{R}^n \times \mathbb{R} \rightarrow \mathbb{R}^n$ we require that i) $\vec{H} = \vec{0}$ for all (\vec{x}, t) and ii) $\vec{H}(\vec{x}_0, 0) = \vec{G}(\vec{x}_0)$ and $\vec{H}(\vec{x}_1, 1) = \vec{F}(\vec{x}_1) = \vec{0}$. Under certain regularity conditions, the Jacobian of \vec{H} , $D\vec{H}$, is of full rank even at points where $\mathbf{F}_{\mathbf{x}}$ is singular and, by the implicit function theorem, there exists a unique differentiable path $\Gamma : \mathbb{R} \rightarrow \mathbb{R}^n \times \mathbb{R}$,

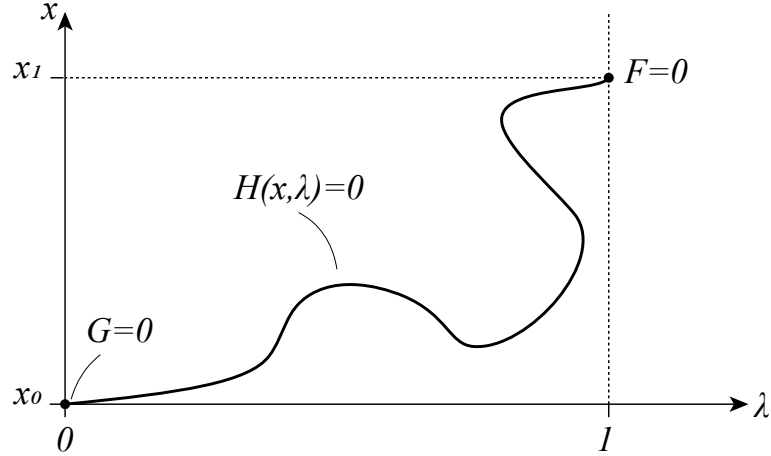


Fig. 4.1. A homotopy path connecting the trivial solution of $G = 0$ to a root of $F = 0$ for a single scalar equation dependent on x .

with $\Gamma(s) = (\vec{x}(s), t(s))$, $s \in \mathbb{R}$ and $\vec{H}(\Gamma) = \vec{0}$. This path connects the solution of the trivial problem, \vec{x}_0 , at $t_0 = 0$ with at least one root of \vec{F} , \vec{x}_1 , when $t = 1$ and can be tracked using numerical continuation[48]. The process of varying parameter t from $0 \rightarrow 1$ is referred to as deformation from the simple problem $\vec{G} = \vec{0}$ to the initial one, $\vec{F} = \vec{0}$, and such a path is depicted in figure (2.1).

The path Γ depends on how \vec{H} is defined, which in turn is determined by the choice for \vec{G} . We distinguish two general cases of homotopy imbeddings: artificial and natural.

One typically resorts to artificial homotopies when a simple solution to problem (4.1) is generally not available. The homotopy parameter t and the simpler problem \vec{G} are then simply devices that initialize the deformation process. In this case, only the final point $(\vec{x}_1, 1)$ is of interest and not the path Γ . A commonly used form of artificial homotopy is the convex homotopy:

$$\vec{H}(\vec{x}, t) = t\vec{F}(\vec{x}) + (1 - t)\vec{G}(\vec{x}) = \vec{0} \quad (4.3)$$

Among the variety of convex homotopy functions that have been developed, the ones most frequently used in implementations are:

- Probability one homotopy: $\vec{G}(\vec{x}) = \vec{x} - \vec{x}_0$ [52, 83]

- Newton homotopy: $\vec{G}(\vec{x}) = \vec{F}(\vec{x}) - \vec{F}(\vec{x}_0)$ [50, 84]

- Affine homotopy: $\vec{G}(\vec{x}) = \mathbf{F}_{\mathbf{x}0}(\vec{x} - \vec{x}_0)$ [85, 59]

On the other hand, systems whose response depends on variations of a parameter, t , that has physical meaning can be recast as natural homotopies as follows:

$$\vec{R}(\vec{x}) = 0 \xrightarrow{\text{parameterization}} \vec{R}(\vec{x}, t) = 0 \quad (4.4)$$

Frequently, in such cases an initial state of the system, \vec{R}_0 , is easily found and the deformation process starts from there. The process ends when one or more target states are found, which, by convention, correspond to $t = 1$. In contrast with artificial imbeddings, the path Γ generated by Eq. (4.4) is also of interest because all $(\vec{x}, t) \in \Gamma$ represent states of the system. As an example, the residual balance equations in nonlinear mechanics, $\vec{R}(\vec{u}) = \vec{0}$, can be cast as a natural homotopy, $\vec{R}(\vec{u}, t) = \vec{0}$, where \vec{u} is the displacement vector and λ represents the load intensity of extern loads.

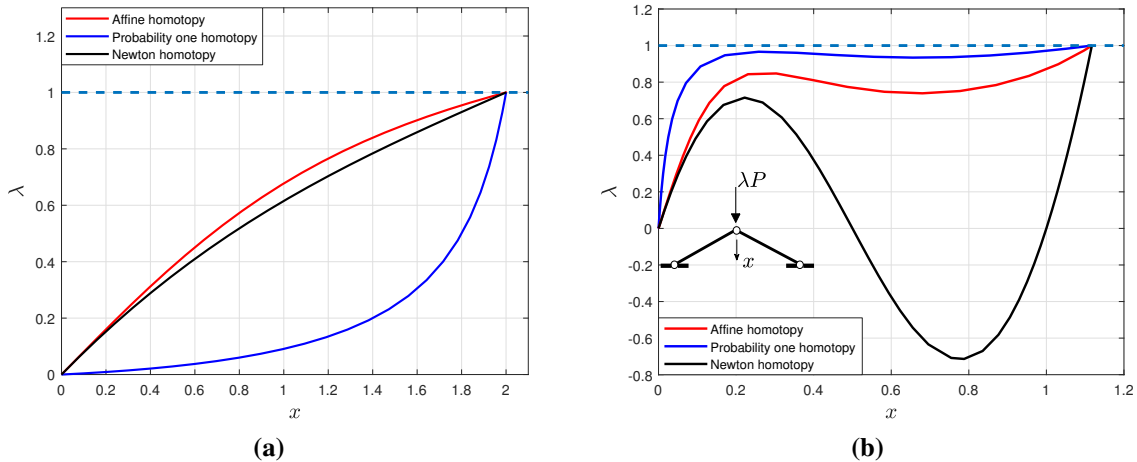


Fig. 4.2. Homotopy paths for (a) $f(x) = x^3 - 6x^2 + 21x - 26 = 0$, with starting point $x_0 = 0$ and convergence at root $x_1 = 2$ when $t = 1$ and (b) truss, with initial state the undeformed configuration($x_0 = 0$) and target load level $P = 0.03$.

A simple demonstration is provided in figure 4.2, where the three artificial homotopies mentioned above are used in two problems. In the first problem (Fig. 4.2a), we find a root of a cubic polynomial, while in the second (Fig. 4.2b) we solve the one degree of freedom truss for target state corresponding to load $P = 0.03$. Details for this example are taken from [86]. We see from the truss case that while, in principle, artificial imbeddings can be used for systems that can be naturally parameterized, the intermediate solution points on the path do not correspond to actual equilibrium configurations.

4.2.2 Regularity and existence of homotopy paths

From the discussion so far it is evident that the study of mappings $\vec{H} : \mathbb{R}^{n+1} \rightarrow \mathbb{R}^n$ is of primary importance. Consider such a mapping, $\vec{H}(\vec{v})$, which is at least of C^k continuity, $k \geq 2$, with $\vec{v} \in \mathbb{R}^{n+1}$ and t being its $(n+1)$ th component. For any given $\vec{w} \in \mathbb{R}^n$, the equation $\vec{H}(\vec{v}) = \vec{w}$ represents a system of n equations with $n+1$ unknowns and we designate the subset of \mathbb{R}^{n+1} satisfying this system as follows:

$$\vec{H}^{-1}(\vec{w}) = \{\vec{v} \in \mathbb{R}^{n+1} \mid \vec{H}(\vec{v}) = \vec{w}\} \subseteq \mathbb{R}^{n+1}$$

Definition 4.2.1 (Regular values of \vec{H}). *An element $\vec{w} \in \mathbb{R}^n$ is a regular value of $\vec{H} : \mathbb{R}^{n+1} \rightarrow \mathbb{R}^n$ if its Jacobian, $\mathbf{D}\vec{H}$, has rank n for all $\vec{v} \in \vec{H}^{-1}(\vec{w})$.*

Definition 4.2.2 (Regular points of \vec{H}). *An element $\vec{v} \in \mathbb{R}^{n+1}$ is a regular point of $\vec{H} : \mathbb{R}^{n+1} \rightarrow \mathbb{R}^n$ if its Jacobian at that point is of rank n .*

The components of the $n \times (n+1)$ Jacobian are given by $\mathbf{D}\vec{H}_{ij} = \partial H_i / \partial v_j$. It follows that if \vec{w} is a regular value for \vec{H} , then all $\vec{v} \in \vec{H}^{-1}(\vec{w})$ are regular points. The following lemma[48], stated here without proof, plays a constitutive role in homotopy continuation theory:

Lemma 4.2.1. *Let $\vec{H} : \mathbb{R}^{n+1} \rightarrow \mathbb{R}^n$ be a C^k map, $k \geq 2$, and having $\vec{0}$ as a regular value. Then, the set $\vec{H}^{-1}(\vec{0})$ is a C^k 1-dimensional manifold in \mathbb{R}^{n+1} , comprised of non-intersecting*

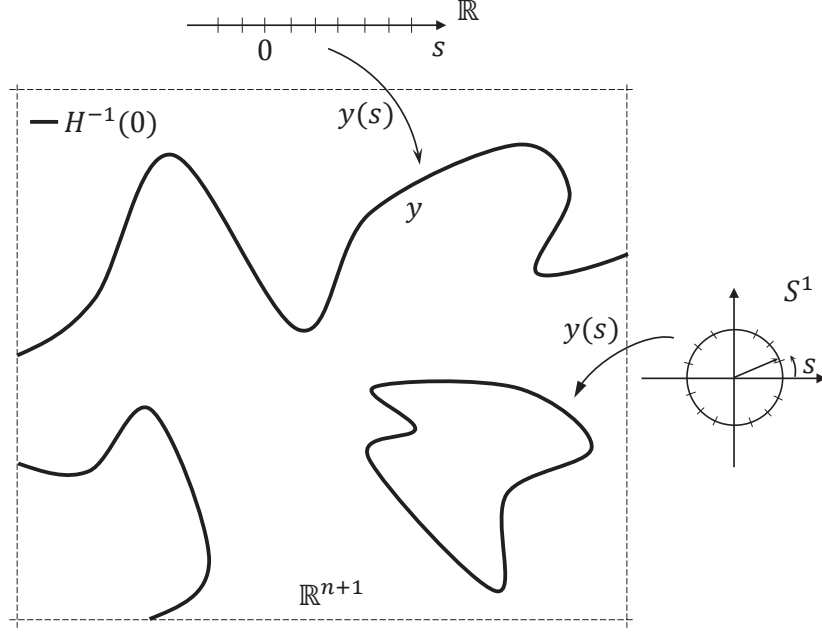


Fig. 4.3. Components of $H^{-1}(0)$ in \mathbb{R}^{n+1} .

components that are either i) homeomorphic with the unit circle S^1 (loops) or ii) homeomorphic with the real line \mathbb{R} (paths).

We refer to the collection of paths and loops in $\vec{H}^{-1}(\vec{0})$ as (connected) components. Figure 4.3 depicts a collection of such components for illustrative purposes. If $\vec{0}$ is a regular value of \vec{H} , by the implicit function theorem, a path(loop) Γ can be described as a C^k map $\Gamma : \mathbb{R}(\text{or } S^1) \rightarrow \mathbb{R}^{n+1}$ such that $\vec{v} = \vec{v}(s)$. The tangent to that curve is given by $\dot{\vec{v}} = d\vec{v}/ds$ and is always a non-zero vector(cf. [48, 85]).

Consider now the case of $\vec{H}(\vec{v})$ where the $n + 1$ -th component of \vec{v} can be regarded as a special parameter of interest, designated as t . We are interested in the zero points of \vec{H} :

$$\vec{H}(\vec{x}, t) = 0 \quad (4.5)$$

where $\vec{x} \in \mathbb{R}^n$, $t \in \mathbb{R}$. Any given initial point $(\vec{x}_0, 0)$ that satisfies Eq. (4.5) sets us on a

component of $\mathbf{H}^{-1}(\vec{\mathbf{0}})$ which we will designate as Γ_0 and define as follows:

$$\Gamma_0 = \{(\vec{x}, t) \mid \vec{x} \in \mathbb{R}^n, t \in \mathbb{R}, (\vec{x}_0, 0) \text{ in } \Gamma_0, \vec{\mathbf{H}}(\vec{x}_0, 0) = \vec{\mathbf{0}}\} \quad (4.6)$$

In most applications we want to ensure the initial point \vec{x}_0 sets us on a component Γ_0 which is a path, not a loop. Under the smoothness and regularity assumptions, the condition which guarantees that is for the $n \times n$ submatrix $\mathbf{D}\mathbf{H} = \partial \vec{\mathbf{H}} / \partial \vec{x}$ to be non-singular at \vec{x}_0 [85]. More conditions are generally required to guarantee that the path will reach $t = 1$ at least once and depend on the particular form of $\vec{\mathbf{H}}$. The interested reader can refer to [48], which provide proofs of existence and convergence for various types of homotopies. In addition, it is customary to formulate homotopies with $t \in [0, 1]$. In our formulation we adhere to the convention that a solution is reached when $t = 1$. However, as is the case in many practical applications, the restriction of t to lie in the unit interval is relaxed and the parameter is allowed to take values outside of that range. The expectation is that more solutions will be reached by crossing the level $t = 1$ multiple times. However, it should be noted that homotopy theory guarantees the (global) convergence to one solution $(\vec{x}_1, 1)$. While certain homotopy imbeddings can find multiple solutions when tracking numerically a single component path[50, 87, 88], it is difficult to establish conditions that guarantee convergence to many or all solutions in general[88].

4.2.3 Parametric nonlinear programming

Our derivations follow closely the works of Kojima & Hirabayashi[60], Gfrerer et al.[63], Gfrerer, Wacker et al.[61], Guddat et al.[62]. Consider the following one-parameter optimization program:

$$\mathbf{P}(t) : \min\{f(\vec{x}, t) \mid \vec{x} \in \Omega(t), t \in \mathbb{R}\} \quad (4.7)$$

with

$$\Omega(t) = \{\vec{x} \in \mathbb{R}^n \mid h_i(\vec{x}, t) = 0, i \in I_h, g_j(\vec{x}, t) \leq 0, j \in I_g\} \quad (4.8)$$

where we assume that functions $f : \mathbb{R}^{n+1} \rightarrow \mathbb{R}$, $h_i : \mathbb{R}^{n+1} \rightarrow \mathbb{R}$ and $g_j : \mathbb{R}^{n+1} \rightarrow \mathbb{R}$ are considered to be C^k , $k \geq 3$, $I_h = \{1, \dots, l\}$, $I_g = \{1, \dots, p\}$ and $l \ll n$, $p \ll n$. Let $\mathcal{L}(\vec{x}, \vec{\lambda}, \vec{\mu}, t)$ be the corresponding Lagrangian function of problem $\mathbf{P}(t)$:

$$\mathcal{L}(\vec{x}, \vec{\lambda}, \vec{\mu}, t) = f(\vec{x}, t) + \sum_{i \in I_h} \lambda_i h_i(\vec{x}, t) + \sum_{j \in I_g} \mu_j g_j(\vec{x}, t) \quad (4.9)$$

where $\vec{\lambda} \in \mathbb{R}^l$ and $\vec{\mu} \in \mathbb{R}^p$ are vectors of Lagrange multipliers, with $\vec{\lambda} = [\lambda_1 \dots \lambda_l]^T$, $\vec{\mu} = [\mu_1 \dots \mu_p]^T$. Additional specifications need to be imposed on set $\Omega(t)$ in order to derive a set of equations which will determine the solution set. Two conditions which we base our exposition on are the Linear Independence Constraint Qualification (LICQ) and the Strict Complementarity Condition (SCC). Let the index set of the active inequality constraints be defined as follows:

$$I_g^a(p) = \{j \mid g_j(\vec{x}, t) = 0, j \in I_g\} \quad (4.10)$$

Definition 4.2.3 (LICQ). At any $\vec{x} \in \Omega(t)$, if the gradients of the active constraints $\{\nabla h_i, \nabla g_j\}$, $i \in I_h$, $j \in I_g^a$, is a set of linearly independent vectors, then the linear independence constraint qualification holds at \vec{x} .

Definition 4.2.4 (SCC). At any $\vec{x} \in \Omega(t)$, if the Lagrange multipliers of the active set of inequality constraints are strictly positive, $\mu_j > 0 \forall j \in I_g^a$, then the strict complementarity condition holds at \vec{x} .

Under the LICQ, SSC and the smoothness assumptions, if \vec{x} is a minimum(maximum) point for $\mathbf{P}(t)$, then there exist unique $\vec{\lambda}$, $\vec{\mu}$ such that the point $(\vec{x}, \vec{\lambda}, \vec{\mu}, t)$ satisfies the so-called Karush-Kuhn-Tucker (KKT) system:

$$\mathbf{KKT}(t) : \quad \nabla_{\vec{x}} \mathcal{L}(\vec{x}, \boldsymbol{\lambda}, \boldsymbol{\mu}, t) = \vec{0} \quad (4.11a)$$

$$h_i(\vec{x}, t) = 0, \quad i \in I_h \quad (4.11b)$$

$$\mu_j g_j(\vec{x}, t) = 0 \quad (4.11c)$$

$$\mu_j \geq 0, g_j(\vec{x}, t) \leq 0, \quad j \in I_g \quad (4.11d)$$

The primary objective of PNLP is to examine the local and global behavior of points that satisfy the $\mathbf{KKT}(t)$ system (4.11). It is convenient to recast the KKT system above into a form that contains only equalities and, thus, homotopy continuation principles can be applied.

Let T be a subdivision of the augmented Lagrangian space $\mathbb{R}^n \times \mathbb{R}^l \times \mathbb{R}^p \times \mathbb{R}$ into cells $\tau(\bar{I}_g)$, where $\tau(\bar{I}_g) = \mathbb{R}^n \times \mathbb{R}^l \times \{\mu \in \mathbb{R}^p \mid \mu_j \geq 0, j \in \bar{I}_g, \mu_j \leq 0, j \in I_g \setminus \bar{I}_g\} \times \mathbb{R}$ for $\bar{I}_g \subset I_g$ and $I_g \setminus \bar{I}_g = \{j \in I_g \mid j \notin \bar{I}_g\}$. That is, the space is partitioned in cells with each cell identified by a particular active index set. Using an active index set strategy, Gfrerer et al[61] showed that problem $\mathbf{P}(t)$ and, consequently, $\mathbf{KKT}(t)$ can be replaced by an equivalent reduced system, which contains only (active) equality constraints[62, 61]:

$$\mathbf{P}^\tau(t) : \quad \min\{f(\vec{x}, t) \mid h_i(\vec{x}, t) = 0, i \in I_h, g_j(\vec{x}, t) = 0, j \in \bar{I}_g, \vec{x} \in \mathbb{R}^n, t \in \mathbb{R}\} \quad (4.12)$$

with the corresponding Lagrangian being:

$$\mathcal{L}^\tau(\vec{x}, \vec{\lambda}, \vec{\mu}, t) = f(\vec{x}, t) + \sum_{i \in I_h} \lambda_i h_i(\vec{x}, t) + \sum_{j \in \bar{I}_g} \mu_j g_j(\vec{x}, t) \quad (4.13)$$

Setting $\vec{z} = (\vec{x}, \vec{\lambda}, \vec{\mu}) \in \mathbb{R}^{n+l+|\bar{I}_g|}$, where $|\bar{I}_g| \leq p$ is the cardinality of \bar{I}_g , the reduced KKT

system for program **P** is:

$$\mathbf{KKT}^\tau(t) : \vec{\mathbf{H}}_{KKT}^\tau(\vec{\mathbf{z}}, t) = \begin{bmatrix} \nabla_{\vec{\mathbf{x}}} \mathcal{L}^\tau(\vec{\mathbf{z}}, t) \\ -h_i(\vec{\mathbf{x}}, t), i \in I_h \\ -g_j(\vec{\mathbf{x}}, t), j \in \bar{I}_g \end{bmatrix} = \begin{bmatrix} \vec{0} \\ 0 \\ 0 \end{bmatrix} \quad (4.14)$$

where $\vec{\mathbf{H}}_{KKT}^\tau(\vec{\mathbf{z}}, t) : \mathbb{R}^{n+l+|\bar{I}_g|+1} \rightarrow \mathbb{R}^{n+l+|\bar{I}_g|}$, that is, in each cell $\vec{\mathbf{H}}_{KKT}^\tau$ is of the form 4.5. This reformulation presupposes that i) LICQ and SCC hold throughout and ii) that $\vec{0}$ is a regular value of the reduced system $\vec{\mathbf{H}}_{KKT}^\tau$ on each cell $\tau(\bar{I}_g)$, which in turn leads to the following corollaries[60]:

1. The set $\cup_\tau [\vec{\mathbf{H}}_{KKT}^\tau]^{-1}(\vec{0})$ is comprised of piecewise continuously differentiable paths(loops) on $\mathbb{R}^{n+l+p+1}$.
2. Each path(or loop) is C^{k-1} in each $\tau(\bar{I}_g) \neq \emptyset$.
3. If a path(or loop) crosses a cell boundary between cells $\tau(\bar{I}_g^1)$ and $\tau(\bar{I}_g^2)$, then sets \bar{I}_g^1 and \bar{I}_g^2 differ by only one index and the tangent vector to the path at the intersection is not tangent to the boundary.

In addition, utilizing condition 3 above, there exists[61] a unique subdivision $\mathcal{D} = \bigcup_{q=1}^Q W^q$ of an interval $[\alpha, \beta]$ on the real line, such that:

- $[\alpha, \beta] = \bigcup_{q=1}^Q W^q$, $W^q = [s_q, s_{q+1}]$, and $s_1 = \alpha, s_Q = \beta$, $q = 1, \dots, Q$.
- $\bar{I}_g(s) = I^q$ where $I^q = I_g^a(s)$, for all s in (s_q, s_{q+1}) .
- $I^q \neq I^{q+1}$.
- By the implicit function theorem, there exist a C^{k-1} function $\vec{\phi}(s) = (\vec{\mathbf{z}}(s), t(s)) : W^q \rightarrow \mathbb{R}^{n+l+|\bar{I}_g|+1}$.
- $\vec{\phi}(s)$ is the solution set for $\mathbf{KKT}^\tau(t)$ for all $s \in W^q$.

In addition, if we require that $\|\mathrm{d}\vec{z}/\mathrm{d}s, \mathrm{d}t/\mathrm{d}s\| = 1$, then s represents the arc-length of the path(or loop). By repeating the process for $q = 1, \dots, Q$, a C^{k-1} piecewise continuous component Γ_0 can be traced numerically using appropriate continuation techniques. At a particular solution point (\vec{z}^*, t^*) , the values of inactive constraints $g_j(\vec{x}^*, t^*)$, $j \in I_g \setminus I^q$ and the Lagrange multipliers of the active constraints, μ_j , $j \in I^q$, are checked to ensure that complementarity slackness holds (eq. (4.11d)). Since adjacent cells differ in their respective active index sets by only one index, violation of the complementarity slackness condition indicates that the continuation entered cell $\tau(I^{q+1})$ and there is a unique index, j_k , such that:

$$g_{j_k}(\vec{x}^*, t^*) \geq 0, \quad j_k \in I_g \setminus I^q \quad \rightarrow \quad I^{q+1} = I^q \cup \{j_k\}, \quad g_{j_k} = 0$$

OR

$$\mu_{j_k} \leq 0, \quad j_k \in I^q \quad \rightarrow \quad I^{q+1} = I^q \setminus \{j_k\}, \quad \mu_{j_k} = 0$$

The collection of paths and loops of stationary points satisfying (4.11) is depicted in Fig. 4.4. For further details on the relevant proofs, refer to Gfrerer et al.[61] and the textbook by Guddat, Vasquez & Jongen[62].

4.2.4 Global optimization

Consider the following NLP:

$$\mathbf{P} : \quad \min\{f(\vec{x}) \mid \vec{x} \in \Omega\} \quad (4.15a)$$

$$\Omega = \{\vec{x} \in \mathbb{R}^n \mid h_i(\vec{x}) = 0, \quad i \in I_h, \quad g_j(\vec{x}) \leq 0, \quad j \in I_g\} \quad (4.15b)$$

where the same assumptions hold for f, h_i and g_j as in PNLP problem (4.7). Conventional numerical tools based in mathematical analysis guarantee the convergence to a (local) minimizer \vec{x}^* of \mathbf{P} provided that the initial guess is within the domain of convergence for the

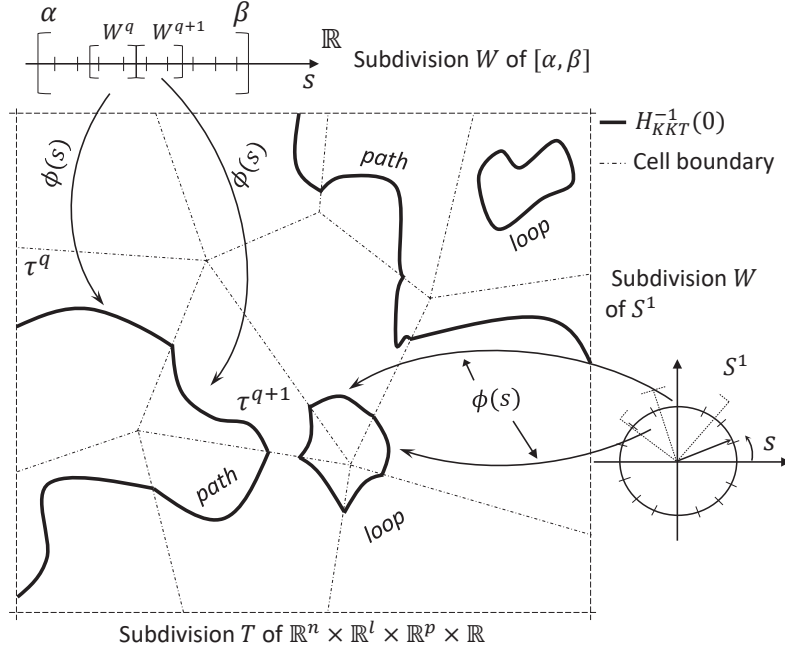


Fig. 4.4. Piecewise continuously differentiable paths and loops of $H_{KKT}^{-1}(0)$ in $\mathbb{R}^{n+l+p+1}$.

particular method employed. By utilizing Homotopy principles, we can convert \mathbf{P} into a PNLP using an appropriate imbedding. A numerical algorithm with global convergence properties can then be constructed, given that the conditions discussed previously hold. Consider the following one-parameter PNLP:

$$\mathcal{P}(t) : \quad \min\{\mathcal{F}(\vec{x}, t) \mid \vec{x} \in \Omega(t), t \in [0, 1]\} \quad (4.16a)$$

$$\Omega(t) = \{\vec{x} \in \mathbb{R}^n \mid \mathcal{H}_i(\vec{x}, t) = 0, i \in I_h, \mathcal{G}_j(\vec{x}, t) \leq 0, j \in I_g\} \quad (4.16b)$$

For $\mathcal{P}(t)$ to be a homotopy imbedding of \mathbf{P} , we require that:

1. NLP $\vec{\mathcal{P}}(0)$ possesses a trivial solution.

2. $\vec{\mathcal{P}}(1) = \mathbf{P}$

If \mathbf{P} can be naturally parameterized, then $\mathcal{P}(t) = \mathbf{P}(t)$, $\mathcal{F}(\vec{x}, t) = f(\vec{x}, t)$ and a stationary point, not necessarily unique, of $\mathbf{P}(0)$ is usually easy to compute. Artificial imbeddings can also be employed when \mathbf{P} cannot be naturally parameterized. In such cases, a trivial stationary point

for $\mathcal{P}(0)$ is easy to compute by construction. Below we list two artificial imbeddings that are frequently used in practice:

- $\mathcal{F}(\vec{x}, t) = tf(\vec{x}) + \frac{1}{2}(1-t)\|\vec{x} - \vec{x}_0\|^2$
- $\mathcal{F}(\vec{x}, t) = \vec{f}(\vec{x}) + \frac{1}{2}(1-t)\|\vec{f}(\vec{x}) - \vec{f}(\vec{x}_0)\|^2$

CHAPTER 5

CONCLUSION

Lorem ipsum dolor sit amet, consectetur adipiscing elit, sed do eiusmod tempor incididunt ut labore et dolore magna aliqua. Ut enim ad minim veniam, quis nostrud exercitation ullamco laboris nisi ut aliquip ex ea commodo consequat. Duis aute irure dolor in reprehenderit in voluptate velit esse cillum dolore eu fugiat nulla pariatur. Excepteur sint occaecat cupidatat non proident, sunt in culpa qui officia deserunt mollit anim id est laborum.

Appendices

APPENDIX A

Explicit expressions of the formulation are provided in this Appendix. We note that operations involving the symbol ∇ map scalars to vectors and vectors to matrices. For example, if $f : \mathbb{R}^p \rightarrow \mathbb{R}$ and $\vec{v} : \mathbb{R}^p \rightarrow \mathbb{R}^q$, then $\nabla f : \mathbb{R}^p \rightarrow \mathbb{R}^p$ and $\nabla \vec{v} : \mathbb{R}^p \rightarrow \mathbb{R}^{p \times q}$.

The Lagrangian function is used here, as presented in Eq. (2.30):

$$\mathcal{L}(\vec{y}, \vec{d}_g, \vec{\lambda}) = U - W + \vec{\lambda}^T \vec{h}_g \quad (\text{A.1})$$

where it is also reminded that $\vec{y} = [\vec{y}_1^T \quad \vec{y}_2^T \quad \dots \quad \vec{y}_m^T]^T$, $\vec{y}_i = [\vec{q}_i \quad \phi_i]^T$ and $\vec{q}_i = [\epsilon_i \quad \gamma_i \quad \kappa_i]^T$. The number m designates the total number of integration points in the structure.

A.0.1 Gradient of strain energy

The gradient of U is expressed as:

$$\nabla U = \begin{bmatrix} \nabla_y U \\ \nabla_{d_g} U \\ \nabla_\lambda U \end{bmatrix}$$

The gradient with respect to the strain vector \vec{y} gives the stress resultants at all cross-sections and has the following form for a particular cross-section i :

$$\nabla_{y_i} U = \begin{bmatrix} w_i N_i \\ w_i V_i \\ w_i M_i \\ 0 \end{bmatrix} = w_i \begin{bmatrix} \vec{F}_{sec}^{(i)} \\ 0 \end{bmatrix} \quad (\text{A.2})$$

it is usually computed by numerical integration of Eqs. (2.55) over the cross-section height. In the case of elastic analysis, the above vector can be computed explicitly for each cross-section, since then $\vec{\mathbf{F}}_{sec}^{(i)} = \begin{bmatrix} EA\epsilon_i & k_s GA\gamma_i & EI\kappa_i \end{bmatrix}^T$.

The gradients of U with respect to both $\vec{\mathbf{d}}_g$ and $\vec{\boldsymbol{\lambda}}$ provide zero vectors:

$$\nabla_{\mathbf{d}_g} U = \vec{\mathbf{0}} \in \mathbb{R}^{3N} \quad \text{and} \quad \nabla_{\boldsymbol{\lambda}} U = \vec{\mathbf{0}} \in \mathbb{R}^s$$

where $s = m + 3n_{el}$, n_{el} being the number of elements. Finally, we then get:

$$\nabla U = \begin{bmatrix} \nabla_{\mathbf{y}} U \\ \vec{\mathbf{0}} \\ \vec{\mathbf{0}} \end{bmatrix} \quad (\text{A.3})$$

A.0.2 Gradient of constraints

We restate the constraints equations from Eqs. (2.32a)-(2.32b):

$$\vec{\mathbf{h}}_g = \begin{bmatrix} \vec{\mathbf{h}}_g^A \\ \vec{\mathbf{h}}_g^B \end{bmatrix} = \begin{bmatrix} \mathbf{V}_1 \vec{\mathbf{d}}_g - \boldsymbol{\Lambda}^T \left[\sum_{i=1}^n w_i \mathbf{R}_i(\vec{\mathbf{q}}_i + \vec{\mathbf{E}}_1) - \ell \vec{\mathbf{E}}_1 \right] \\ \vec{\boldsymbol{\phi}} - \mathbf{V}_2 \vec{\mathbf{d}}_g - \mathbf{T} \vec{\boldsymbol{\kappa}} \end{bmatrix}$$

For notational simplicity, we assume here only one element in the derivations that follow. When more elements are used, their corresponding constraint vectors are stacked in vector form as $\vec{\mathbf{h}} = \begin{bmatrix} \vec{\mathbf{h}}_g^{1T} & \vec{\mathbf{h}}_g^{2T} & \dots & \vec{\mathbf{h}}_g^{n_{el}T} \end{bmatrix}^T$. The gradient with respect to the strain vector $\vec{\mathbf{y}}_i$ at a particular cross-section is given by:

$$\nabla_{\mathbf{y}_i} \vec{\mathbf{h}}_g^A = \begin{bmatrix} \nabla_{\mathbf{q}_i} \vec{\mathbf{h}}_g^A & \frac{d\vec{\mathbf{h}}_g^A}{d\phi_i} \end{bmatrix} = -w_i \boldsymbol{\Lambda}^T \begin{bmatrix} \mathbf{R}_i & \mathbf{R}_i \mathbf{X}[\vec{\mathbf{q}}_i + \vec{\mathbf{E}}_1] \end{bmatrix}$$

where:

$$\frac{d\mathbf{R}_i}{d\phi_i} = \mathbf{R}_i \mathbf{X} \quad \text{and} \quad \mathbf{X} = \begin{bmatrix} 0 & -1 & 0 \\ 1 & 0 & 0 \\ 0 & 0 & 0 \end{bmatrix}$$

The gradient of $\vec{\mathbf{h}}_g^B$ with respect to strain vector $\vec{\mathbf{y}}_i$, is:

$$\nabla_{\mathbf{y}_i} \vec{\mathbf{h}}_g^B = \left[\nabla_{\mathbf{q}_i} \vec{\mathbf{h}}_g^B \quad \frac{d\vec{\mathbf{h}}_g^B}{d\phi_i} \right] = \left[\vec{\mathbf{0}} \quad \vec{\mathbf{0}} \quad -\mathbf{T}\hat{\mathbf{E}}_i \quad \hat{\mathbf{E}}_i \right]$$

where $\hat{\mathbf{E}}_i \in \mathbb{R}^n$ is a unit vector with the i -th component equal to one. Collectively, we have:

$$\nabla_{\mathbf{y}_i} \vec{\mathbf{h}}_g = \begin{bmatrix} -w_i \Lambda^T \mathbf{R}_i & -w_i \Lambda^T \mathbf{R}_i \mathbf{X} [\vec{\mathbf{q}}_i + \vec{\mathbf{E}}_1] \\ [\vec{\mathbf{0}} \quad \vec{\mathbf{0}} \quad -\mathbf{T}\hat{\mathbf{E}}_i] & \hat{\mathbf{E}}_i \end{bmatrix} \quad (\text{A.4})$$

The gradient with respect to the displacement vector is derived in a straightforward manner by simple derivations:

$$\nabla_{\mathbf{d}_g} \vec{\mathbf{h}}_g = \begin{bmatrix} \mathbf{V}_1 \\ -\mathbf{V}_2 \end{bmatrix} \quad (\text{A.5})$$

$$\mathbf{V}_1 = \begin{bmatrix} -\mathbf{I} & \mathbf{I} \end{bmatrix} \quad , \quad \mathbf{V}_2 = \begin{bmatrix} \vec{\mathbf{0}} & \vec{\mathbf{0}} & \vec{\mathbf{1}} & \vec{\mathbf{0}} & \vec{\mathbf{0}} & \vec{\mathbf{0}} \end{bmatrix}$$

$$\mathbf{I} = \begin{bmatrix} 1 & 0 & 0 \\ 0 & 1 & 0 \\ 0 & 0 & 1 \end{bmatrix} \quad , \quad \vec{\mathbf{0}}, \vec{\mathbf{1}} \in \mathbb{R}^n, \quad \vec{\mathbf{0}} = \begin{bmatrix} 0 & \dots & 0 \end{bmatrix}^T, \quad \vec{\mathbf{1}} = \begin{bmatrix} 1 & \dots & 1 \end{bmatrix}^T$$

Finally, the gradient with respect to the vector $\vec{\lambda}$ gives a zero matrix:

$$\nabla_{\lambda} \vec{h}_g = \mathbf{0} \in \mathbb{R}^{(n+3) \times (n+3)} \quad (\text{A.6})$$

The total constraints gradient is then expressed in block matrix form as:

$$\nabla \vec{h}_g = \begin{bmatrix} \nabla_{y_1} \vec{h}_g & \nabla_{y_2} \vec{h}_g & \cdots & \nabla_{y_n} \vec{h}_g & \nabla_{d_g} \vec{h}_g & \nabla_{\lambda} \vec{h}_g \end{bmatrix}$$

Note that in the case of small displacements, only the expression $\nabla_{y_i} \vec{h}_g^A$ has to be modified, so that the strain-displacement relations reduce to the classical linear Timoshenko theory:

$$\nabla_{y_i} \vec{h}_g^A = -w_i \Lambda^T \begin{bmatrix} 1 & -\phi_i & 0 & -\gamma_i \\ 0 & 1 & 0 & 1 \\ 0 & 0 & 1 & 0 \end{bmatrix}$$

with the vector of constraints \vec{h}_g^A being:

$$\vec{h}_g^A = \mathbf{V}_1 \vec{d}_g - \Lambda^T \left[\sum_{i=1}^n w_i [\hat{\mathbf{R}}_i (\vec{q}_i + \vec{E}_1) - \vec{g}_i] - \ell \vec{E}_1 \right] \quad (\text{A.7})$$

where:

$$\hat{\mathbf{R}}_i = \begin{bmatrix} 1 & -\phi_i & 0 \\ \phi_i & 1 & 0 \\ 0 & 0 & 1 \end{bmatrix}, \quad \vec{g}_i = \begin{bmatrix} 0 \\ \epsilon_i \phi_i \\ 0 \end{bmatrix}$$

The vector \vec{g}_i is added in order to eliminate the second order term $\epsilon_i \phi_i$ arising from the imposition of the small displacement assumption $\sin \phi_i \approx \phi_i, \cos \phi_i \approx 1$ in Eq. (2.32a).

A.0.3 Gradient of the potential energy

The potential energy due to external loads $\vec{\mathbf{P}}$ is:

$$W = \sum_{j=1}^N \vec{\mathbf{P}}_j^T \vec{\mathbf{d}}_{g,j} = \vec{\mathbf{d}}_g^T \vec{\mathbf{P}}$$

The gradient of the potential energy is, again, straightforward in its derivation as it only depends on the displacement vector:

$$\nabla W = \begin{bmatrix} \nabla_{\mathbf{y}} W \\ \nabla_{\mathbf{d}_g} W \\ \nabla_{\lambda} W \end{bmatrix}$$

with $\nabla_{\mathbf{y}} W = \vec{\mathbf{0}} \in \mathbb{R}^m$, $\nabla_{\mathbf{d}_g} W = \vec{\mathbf{P}}$ and $\nabla_{\lambda} W = \vec{\mathbf{0}} \in \mathbb{R}^{n+3}$ for one element. Thus, we have:

$$\nabla W = \begin{bmatrix} \vec{\mathbf{0}} \\ \vec{\mathbf{P}} \\ \vec{\mathbf{0}} \end{bmatrix} \quad (\text{A.8})$$

A.0.4 Gradient of the Lagrangian

We substitute in Eqs. (2.35) the explicit expressions derived here in the Appendix:

$$\nabla_{\mathbf{y}_i} \mathcal{L} = w_i \begin{bmatrix} \vec{\mathbf{F}}_{sec}^{(i)} \\ 0 \end{bmatrix} + \begin{bmatrix} -w_i \boldsymbol{\Lambda}^T \mathbf{R}_i & -w_i \boldsymbol{\Lambda}^T \mathbf{R}_i \mathbf{X} [\vec{\mathbf{q}}_i + \vec{\mathbf{E}}_1] \\ [\vec{\mathbf{0}} \quad \vec{\mathbf{0}} \quad -\mathbf{T} \hat{\mathbf{E}}_i] & \hat{\mathbf{E}}_i \end{bmatrix}^T \vec{\boldsymbol{\lambda}} \quad (\text{A.9})$$

$$\nabla_{\mathbf{d}_g} \mathcal{L} = - \begin{bmatrix} \vec{\mathbf{0}} \\ \vec{\mathbf{P}} \\ \vec{\mathbf{0}} \end{bmatrix} + \begin{bmatrix} \mathbf{V}_1 \\ -\mathbf{V}_2 \end{bmatrix}^T \vec{\boldsymbol{\lambda}} \quad (\text{A.10})$$

$$\nabla_{\lambda}\mathcal{L}=\vec{h}_g \tag{A.11}$$

APPENDIX B

The Hessian form in Eq. (2.36), is restated here:

$$\mathbf{H} = \begin{bmatrix} \nabla_{\mathbf{y}\mathbf{y}}^2 \mathcal{L} & \mathbf{0} & \nabla_{\mathbf{y}} \vec{\mathbf{h}}_g^T \\ \mathbf{0} & \mathbf{0} & \nabla_{\mathbf{d}_g} \vec{\mathbf{h}}_g^T \\ \nabla_{\mathbf{y}} \vec{\mathbf{h}}_g & \nabla_{\mathbf{d}_g} \vec{\mathbf{h}}_g & \mathbf{0} \end{bmatrix}$$

The gradients of $\vec{\mathbf{h}}_g$ have been derived in the previous section. Thus, for the complete specification of the second order information we need only to determine the second derivative matrix with respect to the strain vector $\vec{\mathbf{y}}$. Since different integration points are independent of one another, then it is clear that $\nabla_{\mathbf{y}_i \mathbf{y}_j}^2 \mathcal{L} = \mathbf{0}$ for $i \neq j$. Therefore, the matrix $\nabla_{\mathbf{y}\mathbf{y}}^2 \mathcal{L}$ has a block diagonal form:

$$\nabla_{\mathbf{y}\mathbf{y}}^2 \mathcal{L} = \begin{bmatrix} \nabla_{\mathbf{y}_i \mathbf{y}_i}^2 \mathcal{L} & \mathbf{0} & \cdots & \mathbf{0} \\ \mathbf{0} & \nabla_{\mathbf{y}_i \mathbf{y}_i}^2 \mathcal{L} & \cdots & \mathbf{0} \\ \vdots & \ddots & & \vdots \\ \mathbf{0} & \cdots & \mathbf{0} & \nabla_{\mathbf{y}_m \mathbf{y}_m}^2 \mathcal{L} \end{bmatrix}$$

and making use of Eq. (2.60) gives:

$$\nabla_{\mathbf{y}_i \mathbf{y}_i}^2 \mathcal{L} = \nabla_{\mathbf{y}_i \mathbf{y}_i}^2 U + \nabla_{\mathbf{y}_i} ([\nabla_{\mathbf{y}_i} \vec{\mathbf{h}}_g]^T \vec{\boldsymbol{\lambda}}) \quad (\text{B.1})$$

As already seen, the second derivative matrix of the strain energy yields the generalized section

stiffness of cross-section i :

$$\nabla_{\mathbf{y}_i}^2 U = w_i \begin{bmatrix} \mathbf{k}_{sec}^{(i)} & \mathbf{0} \\ \mathbf{0} & 0 \end{bmatrix}$$

where $\mathbf{k}_{sec}^{(i)}$ is given by Eq. (2.58) after numerical integration of the cross-section. We only now need to derive the explicit form for the second term of the right hand side in Eq. (B.1). To this end, we separate the Lagrange multiplier vector into two parts, which correspond to vectors $\vec{\mathbf{h}}_h^A$ and $\vec{\mathbf{h}}_h^B$ respectively:

$$\vec{\boldsymbol{\lambda}} = \begin{bmatrix} \vec{\boldsymbol{\lambda}}^A \\ \vec{\boldsymbol{\lambda}}^B \end{bmatrix}$$

Eq. (A.9) can be now restated as:

$$\nabla_{\mathbf{y}_i} \mathcal{L} = w_i \begin{bmatrix} \vec{\mathbf{F}}_{sec}^{(i)} \\ 0 \end{bmatrix} - w_i \begin{bmatrix} \mathbf{R}_i^T \boldsymbol{\Lambda} \\ [\vec{\mathbf{q}}_i + \vec{\mathbf{E}}_1]^T \mathbf{X}^T \mathbf{R}_i \boldsymbol{\Lambda} \end{bmatrix} \vec{\boldsymbol{\lambda}}^A + \begin{bmatrix} \vec{\mathbf{0}}^T \\ \vec{\mathbf{0}}^T \\ -\hat{\mathbf{E}}_i^T \mathbf{T}^T \\ \hat{\mathbf{E}}_i^T \end{bmatrix} \vec{\boldsymbol{\lambda}}^B \quad (\text{B.2})$$

Noticing that the gradient of $\vec{\mathbf{h}}_g^B$ yields components independent of strains, we conclude that the second derivatives of \mathcal{L} will include only the part $\vec{\boldsymbol{\lambda}}^A$, as:

$$\nabla_{\mathbf{y}_i}^2 \mathcal{L} = \nabla_{\mathbf{y}_i}^2 U + \mathbf{Z}_i \quad (\text{B.3})$$

where:

$$\mathbf{Z}_i = \begin{bmatrix} \mathbf{0}_{(3 \times 3)} & \vec{\mathbf{t}}_i \\ \vec{\mathbf{t}}_i^T & \vec{\mathbf{t}}_i^T \mathbf{X} [\vec{\mathbf{q}}_i + \vec{\mathbf{E}}_1] \end{bmatrix} \quad \text{and} \quad \vec{\mathbf{t}}_i = -w_i \mathbf{X}^T \mathbf{R}_i^T \boldsymbol{\Lambda} \vec{\boldsymbol{\lambda}}^A$$

and the second derivative matrix of the Lagrangian is now fully determined.

APPENDIX C

First, we express the effective stress vector $\vec{\zeta}_{n+1}$ purely in terms of λ , using eq. (3.23a) and the fact that $\vec{n} = \sqrt{\frac{3}{2}} \frac{\mathbf{V}\vec{\zeta}}{\|\vec{\zeta}\|_{\mathbf{V}}}$:

$$\left[\mathbf{I} + \frac{\lambda \sqrt{\frac{3}{2}}}{\|\vec{\zeta}_{n+1}\|_{\mathbf{V}}} \left[\mathbf{C}^{el} \mathbf{V} + H_{kin} \mathbf{I} \right] \right] \vec{\zeta}_{n+1} = \vec{\zeta}_{n+1}^{TR} \quad (\text{C.1})$$

In the first phase of a plastic step we assume that no plastic flow occurs (Elastic Prediction), therefore, for the purposes of the iterative strategy we can consider the following identity:

$$f_{n+1} = 0 \rightarrow \|\vec{\zeta}_{n+1}\|_{\mathbf{V}} = q_n + \lambda \sqrt{\frac{2}{3}} \frac{\partial q_n}{\partial e_n^{pl}} \quad (\text{C.2})$$

In the case of linear isotropic hardening, eq. (C.2) is exact since $\frac{\partial q}{\partial e^{pl}} = H_{iso}$. Otherwise the isotropic modulus used in the context of the fully implicit integration is replaced with the one at the previous step for the purposes of the iterative strategy and only for that. This technique is done so that $\vec{\zeta}_{n+1}$ is recast only in terms of λ . Substituting (C.2) into (C.1) and solving for $\vec{\zeta}_{n+1}$ we get:

$$\vec{\zeta}_{n+1} = \Omega \vec{\zeta}_{n+1}^{TR} \quad (\text{C.3})$$

Let $a_1 = E + \frac{3}{2}H_{kin} + \frac{\partial q_n}{\partial e_n^{pl}}$ and $a_2 = 3G + \frac{3}{2}H_{kin} + \frac{\partial q_n}{\partial e_n^{pl}}$. Then:

$$\Omega = \left[\mathbf{I} + \frac{\lambda \sqrt{\frac{3}{2}}}{q_n + \lambda \sqrt{\frac{2}{3}} \frac{\partial q_n}{\partial e_n^{pl}}} \left[\mathbf{C}^{el} \mathbf{V} + H_{kin} \mathbf{I} \right] \right]^{-1} = \text{diag} \left(\frac{q_n + \lambda \frac{\partial q_n}{\partial e_n^{pl}}}{q_n + \lambda a_1}, \frac{q_n + \lambda \frac{\partial q_n}{\partial e_n^{pl}}}{q_n + \lambda a_2} \right) \quad (\text{C.4})$$

Substitution of (C.3) into $f(\vec{\zeta}_{n+1}, q_{n+1}) \equiv f_{n+1} = 0$ yields the scalar equation to be solved

iteratively for λ :

$$f_{n+1} = \sqrt{\frac{3}{2}} \sqrt{(\vec{\zeta}_{n+1}^{TR})^T \Omega \mathbf{V} \Omega \vec{\zeta}_{n+1}^{TR}} - q_{n+1} = 0 \quad (\text{C.5})$$

The derivative of f_{n+1} with respect to λ involves finding the derivative of the diagonal matrix Ω and a chain rule with respect to q_{n+1} . It can be found that the derivative is:

$$\frac{df_{n+1}}{d\lambda} = -\frac{1}{q_n} \left[\frac{n_{11}\zeta_{11}^{TR}(E + \frac{3}{2}H_{kin})}{(1 + \frac{\lambda a_1}{q_n})^2} + \frac{n_{12}\zeta_{12}^{TR}(3G + \frac{3}{2}H_{kin})}{(1 + \frac{\lambda a_2}{q_n})^2} \right] - (1 + \lambda) \frac{\partial q_{n+1}}{\partial e_{n+1}^{pl}} \quad (\text{C.6})$$

APPENDIX D

For the inversion of the block matrix (3.25a) we perform block elimination considering $\mathbf{A} = \mathbf{C}^{el} + \lambda\boldsymbol{\Psi} - \lambda^2\boldsymbol{\Psi}_{n+1}\left[H_{kin}\mathbf{V} + \lambda\boldsymbol{\Psi}_{n+1}\right]^{-1}\boldsymbol{\Psi}_{n+1}$ as the Schur complement. Notice that while the matrix $\lambda\boldsymbol{\Psi}_{n+1}$ is not invertible, the diagonal ones are. Omitting the subscript referring to the step, inversion of system (3.25a) yields:

$$\begin{bmatrix} d\vec{\sigma} \\ d\vec{\alpha} \end{bmatrix} = \begin{bmatrix} \boldsymbol{\Xi}_{11} & \boldsymbol{\Xi}_{12} \\ \boldsymbol{\Xi}_{21} & \boldsymbol{\Xi}_{22} \end{bmatrix} \begin{bmatrix} d\vec{\epsilon} - d\lambda\vec{n} \\ d\lambda\vec{n} \end{bmatrix} \quad (\text{D.1})$$

and define $\boldsymbol{\Gamma} = \lambda\boldsymbol{\Psi}\left(H_{kin}^{-1}\mathbf{V} + \lambda\boldsymbol{\Psi}\right)^{-1}$. Then, for the block matrices $[\boldsymbol{\Xi}_{ij}]$ we have:

- $\boldsymbol{\Xi}_{11} = \mathbf{A}^{-1}$, the inverse of the Schur complement.
- $\boldsymbol{\Xi}_{12} = \boldsymbol{\Xi}_{11}\boldsymbol{\Gamma}$
- $\boldsymbol{\Xi}_{21} = \boldsymbol{\Xi}_{12}^T$
- $\boldsymbol{\Xi}_{22} = \left(H_{kin}^{-1}\mathbf{V} + \lambda\boldsymbol{\Psi}\right)^{-1} + \boldsymbol{\Gamma}\boldsymbol{\Xi}_{11}\boldsymbol{\Gamma}$

where the fact that matrices $\boldsymbol{\Psi}$ and $\boldsymbol{\Gamma}$ are symmetric was used. The vector \vec{N} in (3.28) is given by:

$$\vec{N} = \frac{[\boldsymbol{\Xi}_{11} + \boldsymbol{\Xi}_{12}]\vec{n}}{\|\vec{n}\|_M} \quad (\text{D.2})$$

with $\mathbf{M} = \boldsymbol{\Xi}_{11} + \boldsymbol{\Xi}_{22} + \boldsymbol{\Xi}_{12} + \boldsymbol{\Xi}_{21}$. Finally, parameter δ is defined as:

$$\delta = \frac{\frac{\partial q}{\partial e^{pl}}}{\|\vec{n}\|_M^2} \quad (\text{D.3})$$

The calculation can be simplified significantly if second and higher order terms in λ are ignored.

BIBLIOGRAPHY

- [1] E. Reissner, “On one-dimensional finite-strain beam theory: The plane problem,” *Zeitschrift für Angewandte Mathematik und Mechanik*, vol. 23, no. 5, pp. 795–804, 1972.
- [2] J. Simo, “A finite strain beam formulation. The three-dimensional dynamic problem. Part I,” *Computer Methods in Applied Mechanics and Engineering*, vol. 49, no. 1, pp. 55–70, 1985.
- [3] J. Simo and L. Vu-Quoc, “A three-dimensional finite-strain rod model. Part II: Computational aspects,” *Computer Methods in Applied Mechanics and Engineering*, vol. 58, no. 1, pp. 79–116, 1986.
- [4] J. Simo and L. Vu-Quoc, “On the dynamics of flexible beams under large overall motions—the plane case: Part I,” *Journal of Applied Mechanics*, vol. 4, no. 53, pp. 849–854, 1986.
- [5] A. Neuenhofer and F. C. Filippou, “Geometrically nonlinear flexibility-based frame finite element,” *Journal of Structural Engineering*, vol. 124, no. 6, pp. 704–711, 1998.
- [6] M. Schulz and F. C. Filippou, “Non-linear spatial timoshenko beam element with curvature interpolation,” *International Journal for Numerical Methods in Engineering*, vol. 50, no. 4, pp. 761–785, 2001.
- [7] A. Cardona and M. Geradin, *Flexible Multibody Dynamics: A Finite Element Approach*, English. UK: John Wiley and Sons, 2001.
- [8] D. Hodges, “Proper definition of curvature in nonlinear beam kinematics,” *American Institute of Aeronautics and Astronautics Journal*, vol. 22, no. 12, pp. 1825–1827, 1984.
- [9] D. Luenberger and Y. Yu, *Linear and Nonlinear Programming*, English. New York, NY: Springer, 2008.

- [10] K. Washizu, Variational Methods in Elasticity and Plasticity, English. Pergamon Press, 1975.
- [11] J. Simo and T. Hughes, Computational Inelasticity, English. New York,NY: Springer, 1998.
- [12] C. P. Andriotis, K. G. Papakonstantinou, and V. K. Koumousis, “Nonlinear programming hybrid beam-column element formulation for large-displacement elastic and inelastic analysis,” Journal of Engineering Mechanics, vol. 144, no. 10, p. 04018096, 2018.
- [13] M. Crisfield, “A fast incremental/iterative solution procedure that handles ”snap-through”,” Computers & Structures, vol. 13, no. 1–3, pp. 55–62, 1981.
- [14] G. Cowper, “The shear coefficient in timoshenko’s beam theory,” Journal of Applied Mechanics, vol. 33, no. 2, pp. 335–340, 1966.
- [15] S. Mazzoni, F. McKenna, M. Scott, and G. Fenves, “Opensees command language manual,” Pacific Earthquake Engineering Research (PEER) Center, vol. 264, 2006.
- [16] A. Neuenhofer and F. C. Filippou, “Evaluation of nonlinear frame finite-element models,” Journal of Structural Engineering, vol. 123, no. 7, pp. 958–966, 1997.
- [17] ABAQUS/Standard User’s Manual, English. United States: Dassault Systèmes Simulia Corp, 2019.
- [18] K. Bishopp and D. Drucker, “Large deflection of cantilever beams,” Quarterly of Applied Mathematics, vol. 3, no. 3, pp. 272–275, 1945.
- [19] K. Mattiasson, “Numerical results from large deflection beam and frame problems analysed by means of elliptic integrals,” International Journal for Numerical Methods in Engineering, vol. 17, no. 1, pp. 145–153, 1981.
- [20] M. Batista, “A closed-form solution for Reissner planar finite-strain beam using Jacobi elliptic functions,” International Journal of Solids and Structures, vol. 87, pp. 153–166, 2016.

- [21] J. Reddy, “On locking-free shear deformable beam finite elements,” *Computer Methods in Applied Mechanics and Engineering*, vol. 149, no. 1-4, pp. 113–132, 1997.
- [22] G. Prathap and G. Bhashyam, “Reduced integration and the shear-flexible beam element,” *International Journal for Numerical Methods in Engineering*, vol. 18, no. 2, pp. 195–210, 1982.
- [23] O. Zienkiewicz, R. Taylor, and J. Too, “Reduced integration technique in general analysis of plates and shells,” *International Journal for Numerical Methods in Engineering*, vol. 3, no. 2, pp. 275–290, 1971.
- [24] S.-L. Lee, F. S. Manuel, and E. C. Rossow, “Large deflections and stability of elastic frames,” *Journal of Engineering Mechanics Division*, vol. 94, no. 2, pp. 521–548, 1968.
- [25] M. R. Horne, “Elastic-plastic failure loads of plane frames,” *Proceedings of the Royal Society of London A: Mathematical, Physical and Engineering Sciences*, vol. 274, no. 1358, pp. 343–364, 1963.
- [26] H. Santos, “Complementary-energy methods for geometrically non-linear structural models: An overview and recent developments in the analysis of frames,” *Archives of Computational Methods in Engineering*, vol. 18, no. 4, p. 405, 2011.
- [27] J. Simo and R. Taylor, “A return mapping algorithm for plane stress elastoplasticity,” *International Journal for Numerical Methods in Engineering*, vol. 22, no. 3, pp. 649–670, 1986.
- [28] A. Papachristidis, M. Fragiadakis, and M. Papadrakakis, “A 3d fibre beam-column element with shear modelling for the inelastic analysis of steel structures,” *Computational Mechanics*, vol. 45, no. 6, pp. 553–572, 2010.
- [29] A. Saritas and F. C. Filippou, “Frame element for metallic shear-yielding members under cyclic loading,” *Journal of Structural Engineering*, vol. 135, no. 9, pp. 1115–1123, 2009.
- [30] P. Ceresa, L. Petrini, R. Pinho, and R. Sousa, “A fibre flexure–shear model for seismic analysis of rc-framed structures,” *Earthquake Engineering & Structural Dynamics*, vol. 38, no. 5, pp. 565–586, 2009.

- [31] J. N. Gregori, P. M. Sosa, M. F. Prada, and F. C. Filippou, “A 3d numerical model for reinforced and prestressed concrete elements subjected to combined axial, bending, shear and torsion loading,” *Engineering Structures*, vol. 29, no. 12, pp. 3404–3419, 2007.
- [32] A. Kagermanov and P. Ceresa, “Fiber-section model with an exact shear strain profile for two-dimensional rc frame structures,” *Journal of Structural Engineering*, vol. 143, no. 10, p. 04017132, 2017.
- [33] J. C. Simo and T. J. Hughes, *Computational inelasticity*. Springer Science & Business Media, 2006, vol. 7.
- [34] M. L. Wilkins, “Calculation of elastic-plastic flow,” California Univ Livermore Radiation Lab, Tech. Rep., 1963.
- [35] R. H. Dodds Jr, “Numerical techniques for plasticity computations in finite element analysis,” *Computers & Structures*, vol. 26, no. 5, pp. 767–779, 1987.
- [36] F. De Angelis and R. L. Taylor, “An efficient return mapping algorithm for elastoplasticity with exact closed form solution of the local constitutive problem,” *Engineering Computations*, vol. 32, no. 8, 2015.
- [37] J. Clausen, L. Damkilde, and L. Andersen, “Efficient return algorithms for associated plasticity with multiple yield planes,” *International Journal for Numerical Methods in Engineering*, vol. 66, no. 6, pp. 1036–1059, 2006.
- [38] O. Hopperstad and S Remseth, “A return mapping algorithm for a class of cyclic plasticity models,” *International Journal for Numerical Methods in Engineering*, vol. 38, no. 4, pp. 549–564, 1995.
- [39] W. M. Scherzinger, “A return mapping algorithm for isotropic and anisotropic plasticity models using a line search method,” *Computer Methods in Applied Mechanics and Engineering*, vol. 317, pp. 526–553, 2017.

- [40] A. R. Hartloper, A. de Castro e Sousa, and D. G. Lignos, “Constitutive modeling of structural steels: Nonlinear isotropic/kinematic hardening material model and its calibration,” *Journal of Structural Engineering*, vol. 147, no. 4, p. 04021031, 2021.
- [41] J. C. Simo and R. L. Taylor, “Consistent tangent operators for rate-independent elasto-plasticity,” *Computer methods in applied mechanics and engineering*, vol. 48, no. 1, pp. 101–118, 1985.
- [42] M Ortiz and E. P. Popov, “Accuracy and stability of integration algorithms for elastoplastic constitutive relations,” *International journal for numerical methods in engineering*, vol. 21, no. 9, pp. 1561–1576, 1985.
- [43] E. A. de Souza Neto, D. Peric, and D. R. Owen, *Computational methods for plasticity: theory and applications*. John Wiley & Sons, 2011.
- [44] K. D. Hjelmstad and E. P. Popov, “Cyclic behavior and design of link beams,” *Journal of Structural Engineering*, vol. 109, no. 10, pp. 2387–2403, 1983.
- [45] J. Argyris, B Boni, U Hindenlang, and M Kleiber, “Finite element analysis of two-and three-dimensional elasto-plastic frames—the natural approach,” *Computer Methods in Applied Mechanics and Engineering*, vol. 35, no. 2, pp. 221–248, 1982.
- [46] R. A. Ridha and L. H. Lee, “Inelastic finite deformation of planar frames,” *Journal of the Engineering Mechanics Division*, vol. 97, no. 3, pp. 773–789, 1971.
- [47] M Amir, K. Papakonstantinou, and G. Warn, “Scaled spherical simplex filter and state-space damage-plasticity finite-element model for computationally efficient system identification,” *Journal of Engineering Mechanics*, vol. 148, no. 2, p. 04021138, 2022.
- [48] E. L. Allgower and K. Georg, *Introduction to numerical continuation methods*. SIAM, 2003.
- [49] W. C. Rheinboldt, “Numerical continuation methods: A perspective,” *Journal of computational and applied mathematics*, vol. 124, no. 1-2, pp. 229–244, 2000.

- [50] H. B. Keller, “Global homotopies and newton methods,” in Recent advances in numerical analysis, Elsevier, 1978, pp. 73–94.
- [51] T.-Y. Li and J. A. Yorke, “A simple reliable numerical algorithm for following homotopy paths,” Analysis and computation of fixed points, pp. 73–91, 1980.
- [52] S. N. Chow, J. Mallet-Paret, and J. A. Yorke, “Finding zeroes of maps: Homotopy methods that are constructive with probability one,” Mathematics of Computation, vol. 32, no. 143, pp. 887–899, 1978.
- [53] S.-N. Chow, J. Mallet-Paret, and J. A. Yorke, “A homotopy method for locating all zeros of a system of polynomials,” in Functional differential equations and approximation of fixed points, Springer, 1979, pp. 77–88.
- [54] L. T. Watson, “Globally convergent homotopy methods: A tutorial,” Applied Mathematics and Computation, vol. 31, pp. 369–396, 1989.
- [55] L. T. Watson, “Globally convergent homotopy algorithms for nonlinear systems of equations,” Nonlinear Dynamics, vol. 1, no. 2, pp. 143–191, 1990.
- [56] E. L. Allgower, “A survey of homotopy methods for smooth mappings,” in Numerical solution of nonlinear systems of equations, Springer, 1981, pp. 1–29.
- [57] W. C. Rheinboldt, “Solution fields of nonlinear equations and continuation methods,” SIAM Journal on Numerical Analysis, vol. 17, no. 2, pp. 221–237, 1980.
- [58] W. C. Rheinboldt and J. V. Burkardt, “A locally parameterized continuation process,” ACM Transactions on Mathematical Software (TOMS), vol. 9, no. 2, pp. 215–235, 1983.
- [59] T. Wayburn and J. Seader, “Homotopy continuation methods for computer-aided process design,” Computers & Chemical Engineering, vol. 11, no. 1, pp. 7–25, 1987.
- [60] M. Kojima and R. Hirabayashi, “Continuous deformation of nonlinear programs,” in Sensitivity, Stability and Parametric Analysis, Springer, 1984, pp. 150–198.

- [61] H Gfrerer, H. Wacker, W Zulehner, and J Guddat, “Path-following methods for kuhn-tucker curves by an active index set strategy,” in Systems and Optimization, Springer, 1985, pp. 111–131.
- [62] J. Guddat, F. G. Vazquez, and H. T. Jongen, Parametric optimization: singularities, pathfollowing and junctions, Springer, 1990.
- [63] H. Gfrerer, J Guddat, et al., “A globally convergent algorithm based on imbedding and parametric optimization,” Computing, vol. 30, no. 3, pp. 225–252, 1983.
- [64] W. I. Zangwill and C. Garcia, “Equilibrium programming: The path following approach and dynamics,” Mathematical Programming, vol. 21, no. 1, pp. 262–289, 1981.
- [65] A. B. Poore, “Bifurcations in parametric nonlinear programming,” Annals of Operations Research, vol. 27, no. 1, pp. 343–369, 1990.
- [66] H. T. Jongen and G.-W. Weber, “On parametric nonlinear programming,” Annals of Operations Research, vol. 27, no. 1, pp. 253–283, 1990.
- [67] C. Tiahrt and A. Poore, “Bifurcation and persistance of minima in nonlinear parametric programming,” in Computation and Control, Springer, 1989, pp. 343–353.
- [68] G. A. Wempner, “Discrete approximations related to nonlinear theories of solids,” International Journal of Solids and Structures, vol. 7, no. 11, pp. 1581–1599, 1971.
- [69] P. Bergan, G Horrigmoe, B Bråkeland, and T. Søreide, “Solution techniques for non- linear finite element problems,” International Journal for Numerical Methods in Engineering, vol. 12, no. 11, pp. 1677–1696, 1978.
- [70] P. Bergan and T. Soreide, “Solution of large displacement and instability problems using the current stiffness parameter,” Finite elements in nonlinear mechanics, vol. 2, pp. 647–669, 1978.

- [71] J.-L. Batoz and G. Dhatt, “Incremental displacement algorithms for nonlinear problems,” *International Journal for Numerical Methods in Engineering*, vol. 14, no. 8, pp. 1262–1267, 1979.
- [72] E Riks, “An incremental approach to the solution of snapping and buckling problems,” *International journal of solids and structures*, vol. 15, no. 7, pp. 529–551, 1979.
- [73] E. Ramm, “Strategies for tracing the nonlinear response near limit points,” in *Nonlinear finite element analysis*, Springer, 1981, pp. 63–89.
- [74] L. T. Watson, M. P. Kamat, and M. H. Reaser, “A robust hybrid algorithm for computing multiple equilibrium solutions,” *Engineering Computations*, 1985.
- [75] P. Sideris, M. Nikoukalam, and M Salehi, “A generalized normal flow method with online step controls for pushover analysis of nonlinear softening structures,” *Engineering Structures*, vol. 143, pp. 232–244, 2017.
- [76] G. D. Byrne and L. A. Baird, “Distillation calculations using a locally parameterized continuation method,” *Computers & chemical engineering*, vol. 9, no. 6, pp. 593–599, 1985.
- [77] A Ushida and L. Chua, “Tracing solution curves of non-linear equations with sharp turning points,” *International journal of circuit theory and applications*, vol. 12, no. 1, pp. 1–21, 1984.
- [78] R. N. Borkovsky, U. Doraszelski, and Y. Kryukov, “A user’s guide to solving dynamic stochastic games using the homotopy method,” *Operations Research*, vol. 58, no. 4-part-2, pp. 1116–1132, 2010.
- [79] D. Besanko, U. Doraszelski, Y. Kryukov, and M. Satterthwaite, “Learning-by-doing, organizational forgetting, and industry dynamics,” *Econometrica*, vol. 78, no. 2, pp. 453–508, 2010.
- [80] P. J.-J. Herings and R. Peeters, “Homotopy methods to compute equilibria in game theory,” *Economic Theory*, vol. 42, no. 1, pp. 119–156, 2010.

- [81] M. Bartoň and V. M. Calo, “Optimal quadrature rules for odd-degree spline spaces and their application to tensor-product-based isogeometric analysis,” *Computer Methods in Applied Mechanics and Engineering*, vol. 305, pp. 217–240, 2016.
- [82] P. J. Barendrecht, M. Bartoň, and J. Kosinka, “Efficient quadrature rules for subdivision surfaces in isogeometric analysis,” *Computer Methods in Applied Mechanics and Engineering*, vol. 340, pp. 1–23, 2018.
- [83] L. T. Watson, “Probability-one homotopies in computational science,” *Journal of Computational and Applied Mathematics*, vol. 140, no. 1-2, pp. 785–807, 2002.
- [84] S. Smale, “A convergent process of price adjustment and global newton methods,” *Journal of Mathematical Economics*, vol. 3, no. 2, pp. 107–120, 1976.
- [85] C. Garcia and F. Gould, “Relations between several path following algorithms and local and global newton methods,” *Siam Review*, vol. 22, no. 3, pp. 263–274, 1980.
- [86] W. C. Rheinboldt, “Numerical analysis of continuation methods for nonlinear structural problems,” in *Computational Methods in Nonlinear Structural and Solid Mechanics*, Elsevier, 1981, pp. 103–113.
- [87] W.-J. Lin, J. Seader, and T. Wayburn, “Computing multiple solutions to systems of inter-linked separation columns,” *AIChE Journal*, vol. 33, no. 6, pp. 886–897, 1987.
- [88] A. C. Sun and W. D. Seider, “Homotopy-continuation method for stability analysis in the global minimization of the gibbs free energy,” *Fluid Phase Equilibria*, vol. 103, no. 2, pp. 213–249, 1995.

VITA

Vita may be provided by doctoral students only. The length of the vita is preferably one page. It may include the place of birth and should be written in third person. This vita is similar to the author biography found on book jackets.